

# **DEVELOPMENT OF SODIUM INSTRUMENTATION TECHNIQUES FOR FAST BREEDER REACTORS**

By

**J.I.SYLVIA**

(Enrollment No. ENGG02200804014)

**Indira Gandhi Centre for Atomic Research, Kalpakkam**

*A thesis submitted to the  
Board of studies in Engineering Sciences  
In partial fulfillment of the requirements  
for the Degree of*

**DOCTOR OF PHILOSOPHY**

*of*

**HOMI BHABHA NATIONAL INSTITUTE**



**August, 2014**

# Homi Bhaba National Institute

## Recommendations of the Viva Voce Committee

As members of the Viva Voce Committee, we certify that we have read the dissertation prepared by **Mrs. J.I.Sylvia** entitled “**Development of Sodium Instrumentation Techniques for Fast Breeder Reactors**” and recommend that it may be accepted as fulfilling the thesis requirement for the award of Degree of Doctor of Philosophy.

---

Chairman - **Dr. U. Kamachi Mudali**

**Date:**

---

Guide/Convener - **Dr. K. Velusamy**

**Date :**

---

Member 1 - **Dr. T. Gnanasekaran**

**Date:**

---

Member 2 – **Dr. B. P. C. Rao**

**Date:**

---

**External Examiner – Dr. Jayant K.Singh**

**Date:**

Final approval and acceptance of this thesis is contingent upon the candidate's submission of the final copies of the thesis to HBNI.

I/We hereby certify that I/we have read this thesis prepared under my/our direction and recommend that it may be accepted as fulfilling the thesis requirement.

**Date:**

**Place: Indira Gandhi Centre for Atomic Research**

**Dr. K. Velusamy**

**Kalpakkam**

**Guide**

## **STATEMENT BY AUTHOR**

This dissertation has been submitted in partial fulfillment of requirements for an advanced degree at Homi Bhabha National Institute (HBNI) and is deposited in the Library to be made available to borrowers under rules of the HBNI.

Brief quotations from this dissertation are allowable without special permission, provided that accurate acknowledgement of source is made. Requests for permission for extended quotation from or reproduction of this manuscript in whole or in part may be generated by the Competent Authority of HBNI when in his or her judgment the proposed use of the material is in the interests of scholarship. In all other instances, however, permission must be obtained from the author.

**Kalpakkam**

**(J.I.Sylvia)**

**August 2014**

## **DECLARATION**

I, hereby declare that the investigation presented in the thesis has been carried out by me. The work is original and has not been submitted earlier as a whole or in part for a degree/diploma at this or any other Institution/University.

**Kalpakkam**

**(J.I.Sylvia)**

**August 2014**

## DEDICATIONS

*Dedicated to my Lord and Saviour*

*Jesus Christ*

*My beloved Father, affectionate Mother, supporting Husband  
and lovely Sons*

## ACKNOWLEDGEMENTS

I feel deeply indebted to several people and thank them for supporting me all through my research at Indira Gandhi Centre for Atomic Research, Kalpakkam. I am grateful to the Department for providing me an opportunity to carry out research work.

I express my sincere gratitude to **Dr.K.Velusamy, Head, MHD, RDG** for providing me inspiration and offering valuable suggestions and guidance during the period of my project work. It has been always a pleasure to work under his guidance. His extreme co-operation and complete involvement in the research were instrumental in bringing this thesis in its complete form.

I am thankful to **Mr.S.Clement Ravichander**, Head, CES for his keen interest and availability for the discussions which are of great asset to my work.

I express my heartfelt thanks to **Dr.T.Jayakumar**, Director, MMG, and Dean, HBNI for his constant encouragement and support throughout the research work.

I am highly grateful to my Doctoral Committee (DC) chairman and members (**Dr.U.Kamachi Mudali, Dr.T.Gnanasekaran, Dr.B.P.C.Rao**), for their valuable inputs, constant monitoring of my progress and valuable supports through out the course of my research.

I thank **Dr.P.R.Vasudeva Rao**, Director,IGCAR, **Dr.R.B.Grover**, Director, HBNI, Mumbai and **Dr.B.K.Dutta**, Dean, HBNI, Mumbai for granting extension to continue my research work. I sincerely thank **Dr.M.Sai Baba**, Associate Director, RMG and **Dr. G.Sasikala**, Dean, HBNI for care and support.

My sincere thanks are due to my colleagues of Rig Instrumentation Section for their support during my work.

# CONTENTS

Title	Page No.
<b>SYNOPSIS</b>	vi
<b>LIST OF FIGURES</b>	ix
<b>LIST OF TABLES</b>	xiii
<b>CHAPTER 1 INTRODUCTION</b>	<b>1-22</b>
1.1 FOREWORD	02
1.1.1 Main Characteristics of FBR	03
1.1.2 Sodium as Coolant	03
1.2 FLOW SHEET OF FBR	05
1.3 IN-SITU TIME CONSTANT ESTIMATION OF CORE MONITORING THERMOCOUPLES	09
1.3.1 Classification of Blockages	12
• <i>Gross blockages of subassembly</i>	12
• <i>Local blockages within subassembly</i>	13
• <i>Total instantaneous blockage</i>	14
1.3.2 Need for Fixing Thermocouple Response Time	14
1.4 UNDER SODIUM VIEWING FOR PROTRUSION DETECTION	16
1.5 DEVELOPMENT OF SODIUM LEVEL SENSORS	17
1.5.1 General Techniques for Level Measurement	18
1.5.2 Challenges in Sodium Level Measurement	18
1.6 MOTIVATION FOR THE PRESENT STUDY	18
1.7 SCOPE AND OBJECTIVES OF THE THESIS WORK	20
1.8 ORGANIZATION OF THE THESIS	22

<b>CHAPTER 2 LITERATURE REVIEW</b>	<b>23-33</b>
2.1 CORE TEMPERATURE MONITORING SYSTEM	24
2.2 ULTRASONIC IMAGING IN FBR	29
2.3 DEVELOPMENT OF SODIUM LEVEL SENSOR	31
2.4 CLOSURE	32
<b>CHAPTER 3 IN-SITU ESTIMATION OF TIME CONSTANT FOR CORE TEMPERATURE MONITORING THERMOCOUPLES</b>	<b>34-61</b>
3.1 INTRODUCTION	35
3.2 PRINCIPLE OF OPERATION OF THERMOCOUPLE	35
3.3 SPECIFICATION OF THERMOCOUPLE	37
3.4 LOCATION OF SENSOR IN THE REACTOR	38
3.5 SENSOR CONSTRUCTION	40
3.6 THEORETICAL MODELING OF THERMOWELL	41
3.7 METHODS USED TO DETERMINE THE TIME CONSTANT OF SENSOR IN FBR	45
3.8 ESTIMATION OF TIME CONSTANT OF CORE MONITORING SENSORS IN FBTR	49
3.9 ESTIMATION OF PROCESS TIME CONSTANT	51
3.10 UNCERTAINTIES IN TIME CONSTANT MEASUREMENT	57
3.11 RESULTS AND DISCUSSION	59
3.12 CLOSURE	61
<b>CHAPTER 4 DEVELOPMENT OF ULTRASONIC TECHNIQUES FOR PROTRUSION DETECTION IN CORE TOP</b>	<b>62-105</b>
4.1 INTRODUCTION	63
4.1.1 Principles of Ultrasonic Techniques	65

4.2	CONCEPT OF DETECTION METHOD	65
4.3.	ULTRASONIC IMAGING USING DIRECT IMAGING TECHNIQUE	67
4.3.1	Simulation of Projected Component in the Reactor	68
4.3.2.	Orientation of CSRDM and DSRDM in PFBR	72
4.3.3	Experimental Setup	72
	• <i>Mechanical setup</i>	73
	• <i>PC based automation system</i>	74
	• <i>Ultrasonic scanner</i>	74
	• <i>Ultrasonic Transducer</i>	75
	• <i>Ultrasonic test instrument</i>	76
	• <i>Stepper motor and its drive system</i>	76
	• <i>Software Architecture</i>	78
	• <i>Commissioning of automation system</i>	78
4.3.4	Details of Experiments	79
	• <i>Case – 1</i>	79
	• <i>Case – 2</i>	83
	• <i>Case – 3</i>	83
	• <i>Case – 4</i>	84
4.3.5	Discussion on Various Images	85
4.4	ULTRASONIC IMAGING USING INDIRECT IMAGING TECHNIQUE	87
4.4.1	Simulation	88
4.4.2	Algorithm	90
4.4.3	Details of Experiments	90

•	<i>Experiments in Sector -1</i>	92
•	<i>Protrusion at same angle at different distance</i>	94
•	<i>Protrusion at same distance at different angles</i>	96
•	<i>Protrusion of CSRDM</i>	97
•	<i>Experiments in Sector-4</i>	99
•	<i>Study on effect of inclination of SSA</i>	101
•	<i>Study on Random protrusion</i>	102
4.4.4	Discussion on Results	103
<b>4.5</b>	<b>CLOSURE</b>	<b>104</b>
<b>CHAPTER 5</b>	<b>DEVELOPMENT OF MUTUAL INDUCTANCE</b>	<b>106-133</b>
	<b>TYPE SODIUM LEVEL SENSOR WITH NEW TEMPERATURE</b>	
	<b>COMPENSATION TECHNIQUE</b>	
5.1	INTRODUCTION	107
5.2	THEORY OF LEVEL PROBES	109
5.3	PRINCIPLE OF OPERATION	112
5.4	CONSTRUCTION OF LONG LENGTH LEVEL PROBE	112
5.5	PERFORMANCE EVALUATION	115
5.6	DEVELOPMENT OF TEMPERATURE COMPENSATION	
	TECHNIQUE	116
5.6.1	Principle of New Temperature Compensation Technique	119
5.6.2	Experimental Validation	120
5.7	IMPROVED ELECTRONICS CHASSIS	125
5.8	STUDIES TO IMPROVE THE SENSITIVITY OF THE PROBE	127
5.9	DISCUSSION ON RESULTS	128
5.10	MUTUAL INDUCTANCE TYPE DISCRETE LEVEL PROBE	129

5.11	CONSTRUCTION OF MI TYPE DISCRETE LEVEL PROBE	130
5.12	FREQUENCY RESPONSE STUDIES	131
5.13	DISCUSSION ON RESULT	132
5.14	CONCLUSION	132
<b>CHAPTER 6 CONCLUSIONS</b>		<b>134-139</b>
6.1	IN-SITU TIME CONSTANT ESTIMATION OF CORE THERMOCOUPLES	135
6.1.1	Future Directions	136
6.2	ULTRASONIC TECHNIQUE FOR PROTRUSION DETECTION	136
6.2.1	Future Directions	137
6.3	SODIUM LEVEL MEASUREMENT SYSTEM	138
6.3.1	Future Directions	139
<b>ANNEXURE 1 EFFECT OF GROSS FLOW REDUCTION ON THE MAXIMUM RATED SUBASSEMBLY DUE TO THE PRESENCE OF GROSS BLOCKAGE</b>		<b>140-150</b>
A1.1	ANALYSIS	141
A1.2	MODEL	145
A1.3	CLOSURE	150
<b>ANNEXURE 2 ERROR ESTIMATION IN TIME CONSTANT</b>		<b>151-157</b>
<b>REFERENCES</b>		<b>158-164</b>
<b>NOMENCLATURE</b>		<b>165-172</b>
<b>PUBLICATIONS BASED ON THE THESIS</b>		<b>173</b>

## SYNOPSIS

Core temperature monitoring system is an important component of reactor protection system in the current generation fast reactors. In this system multiple thermocouples are housed inside a thermowell for all fuel subassemblies. The response time of the thermocouple assembly forms an important input for safety analysis of fast reactor and hence frequent calibration/time constant estimation is essential. In fast reactors the central fuel subassembly is provided with bare fast response thermocouples to detect under cooling events in reactor and take proper safety action. On the other hand, thermocouples in thermowell are mainly used for blockage detection in individual fuel subassemblies. The time constant of thermocouples in thermowell can drift due to creep, vibration and thermal fatigue of the thermowell assembly. A novel method for in-situ estimation of time constant is proposed. This method uses the Safety Control Rod Accelerated Mechanism (SCRAM) or lowering of control Rod (LOR) signals of the reactor along with response of the bare central subassembly thermocouples as reference data. Validation of the procedure has been demonstrated by applying it to FBTR.

The 500 MWe, sodium cooled, Prototype Fast Breeder Reactor (PFBR) is under advanced stage of construction at Kalpakkam in India. Opacity of sodium restricts visual inspection of components immersed in sodium by optical means. Ultrasonic wave passes through sodium hence ultrasonic techniques using under sodium ultrasonic scanners are developed to obtain under sodium images. The main objective of such an Under Sodium Ultrasonic Scanner (USUSS) for Prototype Fast Breeder Reactor (PFBR) is to detect and ensure that no core Sub Assembly (SA) or Absorber Rod or its Drive Mechanism is protruded in the above core plenum before starting the fuel handling operation. Hence, it is necessary to detect and locate the object, if it is protruding the above core plenum. To study the feasibility of detecting the absorber rods, their drive mechanisms and protruded hexagonal

subassemblies using direct/indirect ultrasonic imaging technique experiments were carried out for different orientations and profiles of the projected components in a 5 m diameter water tank. The in-house developed PC based ultrasonic scanning system is used for acquisition and analysis of data. The pseudo three dimensional color images obtained are discussed and the results are applicable for PFBR. This report gives the details of the features of the absorber rods and their drive mechanisms, their orientation in the reactor core, experimental setup, PC based ultrasonic scanning system, ultrasonic images and the discussion on the results using direct imaging technique. Development of suitable algorithm for detecting the protruding objects which are not favorable to ultrasonic beam is the challenge of the research.

Continuous and discontinuous level sensors working on Mutual Inductance principle is used in PFBR for monitoring sodium level as well as for safety. The wide and high operating temperature, highly chemically active nature of sodium and its reaction with air make the sodium instrumentation special over conventional Instrumentation. The traditional sodium level sensors such as Resistance Type Level Probe (RTLTP) for discrete level measurements and MI type Continuous Level Probe for continuous level measurement is used in Fast Breeder Test Reactor (FBTR). The challenges involved in making traditional continuous level sensors suitable for PFBR, include development of mechanically robust level sensors of longer length with better resistance to vibration, new method of temperature compensation to improve the accuracy over wide operating range from (150 °C -550 °C) and improved electronics circuit with better features. MI type Discrete Level Probe has been developed as improvement over RTLTP. This thesis highlights construction of longer level probes with leak tight arrangement, performance evaluation of prototype level probes, recent development on temperature compensation technique, improvement in electronics and development of non contact type discrete level probe for PFBR.

The first chapter is an introductory chapter and explains the background, and the need for the present research. The second chapter is on Literature review. Development of techniques for sodium instrumentation viz., temperature measurement, ultrasonic under sodium viewing and sodium level measurements is the major focus of the current research. These are discussed in three chapters.

The background, location of temperature sensor and mathematical modeling, and characteristic graph between variations in response time with contact pressure are established in chapter-3. Details of the in-situ time constant estimation and the validation of the procedure has been demonstrated by applying it to FBTR are also elaborated in chapter-3.

Chapter-4 deals with under sodium ultrasonic imaging. Experimental simulation of the probable protruded objects of absorber rod drive mechanism, development of direct ultrasonic imaging techniques, construction of pseudo coloring images through a PC based automatic scanning system are presented in this chapter. Further, development of an algorithm for detecting the protruding objects having unfavorable orientation to ultrasonic beam, establishing experimental facility, validation of the algorithm by experimental simulation and image construction are also presented in this chapter.

Chapter -5 highlights the performance evaluation of long length level probes and recent development of temperature compensation technique along with simplified electronics.

Chapter-6 summarizes the results and major conclusions of thesis and presents future scope of research.

## LIST OF FIGURES

Fig 1.1	Flow sheet of a typical pool type FBR	06
Fig. 1.2	Vertical sectional view of reactor vessel	07
Fig. 1.3	Fuel subassembly of medium size pool type FBR	11
Fig. 3.1a	Principle of thermocouple	36
Fig 3.1b	Thermocouple circuit	36
Fig. 3.2	FBTR Core configuration	39
Fig. 3.3	Location of thermocouples above fuel subassembly outlet nozzle	39
Fig. 3.4	Details of Chromel Alumel thermocouple in thermowell	40
Fig. 3.5	Details of thermocouple Probe	40
Fig.3.6	Equivalent circuit of thermocouple in thermowell	41
Fig. 3.7	Dependence of time constant on contact pressure	44
Fig. 3.8	Computed sensor temperatures as a function of response time for step input	46
Fig. 3.9	Computed sensor temperatures as a function of response time for ramp input	48
Fig. 3.10	Response of power and temperature of reference thermocouple during LOR	50
Fig. 3.11	Estimation of ramp rate	50
Fig. 3.12	FBTR fuel subassembly	53
Fig. 3.13	Process response time for Zone-1	54
Fig. 3.14	Process response time for Zone-II	55
Fig. 3.15	Radiography Examination of thermocouple	60
Fig. 4.1	Schematic of above core plenum (100 mm gap)	64

Fig. 4.2	PFBR core	66
Fig. 4.3	Principle of protrusion detection	67
Fig. 4.4a	Portion of CSR in 100 mm Plenum	69
Fig. 4.4b	Portion of DSRDM through 100 mm above -Core Plenum	70
Fig. 4.5	Actual and Mockup CSRDM gripper with important dimensions	71
Fig. 4.6	Experimented CSR	71
Fig. 4.7	Experimented electromagnet of DSRDM with support rod	72
Fig. 4.8	Orientation of CSRDM and DSRDM from IVTP access port and Observation port	73
Fig. 4.9	Experimental setup	73
Fig. 4.10	Scheme of Automation system	75
Fig. 4.11a	Case-1 objects and Ultrasonic image with threshold of 0.1V at 0 mm elevation	80
Fig. 4.11b	Case-1 objects and Ultrasonic image with threshold of 0.15V at 0 mm elevation	81
Fig. 4.11c	Case-1 CSRDM object and its ultrasonic image	82
Fig 4.12	Case-2 Ultrasonic image of conical portions of CSRDM/DSRDM	83
Fig. 4.13	Case-3 Objects and its ultrasonic image	84
Fig.4.14	Case- 4 Ultrasonic image of CSR at two different orientations	85
Fig. 4.15	Fuel subassembly head	87
Fig. 4.16	Determination of beam spread in water using 1 MHz transducer	88
Fig. 4.17	Reactor Core of PFBR	92
Fig. 4.18	Sector-1 in Water Setup	93
Fig. 4.19	Simulation of 20mm growth of fuel subassembly	93
Fig. 4.20	Photograph of Sector-I setup simulating protrusion	94

	at same angle at different distances from 1 m ,2m &3m	
Fig. 4.21	Sector -1 C-Scan image by protruding the SA at same angle	95
Fig. 4.22	Photograph of Sector-I setup simulating protrusion	96
	at different angle at same distances (2m)	
Fig. 4.23	C-Scan image of protruded SA at same distance(2 m)	97
	with different angles	
Fig. 4.24	Photograph showing position of protruded CSR conical portion	98
Fig. 4.25	C-Scan image of protruded CSR conical portion	98
	at different lengths from top	
Fig. 4.26	Simulation details of Sector-4	99
Fig. 4.27	Photograph of Sector-4	100
Fig. 4.28 (i)	C- scan image of protruded object at 1m,2,and 3m	100
Fig. 4.28 (ii)	C- scan image of protruded object at 1m, 2m distance	101
Fig. 4.29	Echo from single SSA at different inclination	102
Fig. 4.30	Effect on random and equal protrusion of SSA	103
Fig. 5.1	Typical Installation of Level sensors in PFBR	108
	(LS-Discontinuous level probe, LW- Continuous level probe)	
Fig. 5.2	Magnetic field lines due to a current through the solenoid	109
Fig. 5.3	Mutual Inductance type continuous level probe	113
Fig. 5.4	M.I type level probe with Biological Shielding	115
Fig. 5.5	% Sensitivity Vs frequency	116
Fig. 5.6	Electrical conductivities of sodium and stainless steel	117
Fig. 5.7	Earlier method of temperature compensation	118
Fig. 5.8	Schematic of continuous Level probe	119
Fig. 5.9	Frequency vs External resistance	121

Fig. 5.10	Secondary output without temperature compensation	123
Fig. 5.11	Secondary output with temperature compensation using external resistor	123
Fig. 5.12	Level measuring system using new method of temperature compensation	124
Fig. 5.13	Improved electronics for continuous level probe	127
Fig. 5.14	Bobbin and windings of MI discrete level probe	130
Fig. 5.15	Schematic of MI discrete level sensor	131
Fig. 5.16	%Sensitivity Vs Frequency (kHz)	132
Fig. A1.1	Measured temperature as a function of response time for ramp input	148
Fig. A1.2	Time constant Vs rate of flow reduction	149

## LIST OF TABLES

Table-1.1	Design basis events for core cooling	10
Table-2.1	Details of core monitoring system in fast breeder reactor	28
Table-2.2	literature related to Research and Development in Under-Sodium viewing	30
Table-3.1	Estimation of time constant using analytical modeling	45
Table-3.2	Thermocouple reading for different time constant for a step input of 50 K	47
Table-3.3	Thermocouple reading for different time constants for ramp input	48
Table- 3.4	Time constant and temperature profile for Zone-1	54
Table- 3.5	Time constant and temperature profile for Zone-1I	55
Table-3.6	Estimated time constant of thermocouples (process time subtracted)(2007 data)	56
Table-3.7	Estimated time constant of thermocouples (process delay subtracted)(2012/2007 data)	57
Table-4.1	Shape of objects in case-1	80
Table- 4.2	Simulation of sector in clockwise direction	91
Table -4.3	Simulation of sector in anti-clock wise direction	91
Table-5.1	Secondary output for different temperature with compensation using external resistor	122
Table-5.2	Variation of frequency and resistance at different temperature ranges	125
Table-5.3	Sensitivity studies for varying bobbin dimension	128
Table-5.4	Results of partial compensation and resistor compensation probe	129

Table-A1.1	Flow rate versus clad hot spot temperature	145
Table-A1.2	Thermocouple reading for different time constant for ramp input ( $R=9.0673$ K/s)	148
Table- A2.1	Typical calculation for error in rate	153
Table- A2.2	Error estimation in rate, $T_{ss}$ and $T_m$	154
Table-A2.3	Error estimation in time constant of thermocouple with process	154
Table- A2.4	Error estimation in Rate, $T_m$ and $T_{ss}$ for process	155
Table- A2.5	Error estimation in process time constant	156
Table-A2.6	Error estimation in thermocouple time constant	157

# **CHAPTER-1**

# INTRODUCTION

## 1.1 FOREWORD

India with its present population of over 1.2 billion requires considerable energy to attain world average level of per capita energy consumption. Coal and nuclear energy are the only large resources towards this objective. India's uranium resource is estimated at 50,000 t. If this is invested in Pressurised Heavy Water Reactor (PHWR), it is possible to install and operate about 12 GWe capacity for 30 years whereas by converting the abundant isotope  $U^{238}$  of natural U to Pu, one can install and operate about 250 GWe over 100 years. Therefore, India needs to develop FBR at the earliest possible time. Development of Fast Breeder Reactor (FBR) was pursued very vigorously in the 70's and 80's in many developed countries. But, from strategic considerations and due to lack of demand for energy, availability of alternate resources, stable price of uranium and high cost of FBR, the development has been discontinued for the present in most of the western countries. However, Russia, China, Japan and India continue to develop FBR.

The nuclear energy program in India is being implemented in three stages. A large number of natural uranium fuelled PHWRs are in operation and many are under construction in the first stage. Plutonium generated from PHWRs will be multiplied through breeding in FBR in the second stage. This will facilitate launching of a large scale Th- $^{233}U$  fuel cycle in the third stage. FBRs also utilize natural uranium fuel very effectively (~ 75 %) through breeding and thus provide a rapid energy growth potential. They also constitute a clean source of power unlike fossil fuel power stations. Several FBRs worldwide like EBR-II, Phenix, PFR, BN reactors are witness to their environment friendly performance. The use of thorium in FBRs in the third stage will make it a much larger resource than the combined coal, oil and gas resources.

Thus FBRs will provide long term energy security utilizing the indigenous uranium and abundant thorium reserves.

### **1.1.1 Main Characteristics of FBR**

A fast reactor requires higher fraction (enrichment) of fissile material in the fuel, say about 20%. The neutrons are fast and the neutron flux is more by 10 times compared to that in thermal reactors. The core volume is reduced to reduce the fissile inventory. Hence smaller pin diameter is required. Because of low core volume, the power density is high  $\sim 5$  kW/litre of core. Due to higher linear power rating of fuel, the power extracted from unit mass and unit volume of the fuel is higher. Hence, it needs better heat transfer facilities. Liquid sodium is selected as coolant. But, there will be more neutron leakage. Fertile blanket are provided surrounding the core to profitably capture the escaping neutrons. Higher neutron flux causes higher damage to reactor materials. Unlike thermal reactor, there is no large reactivity change of core due to accumulation of fission products. High fuel burn-up achievable in FBR helps to extend core cycle length to reduce fuelling cost and to increase, Uranium Utilisation (UU) factor. In PHWR, UU is only about 0.4% to 0.5% by once through cycle and is about 1 to 3 % by reprocessing. However, in FBR, UU can be as high as 60 to 70%. Conversion Ratio is defined as the ratio between the number of fissile atoms produced and fissile atoms destroyed. If it is more than 1, then it is called breeding ratio which is high in FBR. The design objectives of FBR include high breeding ratio, short doubling time, low fuel-cycle cost, etc.

### **1.1.2 Sodium as Coolant**

A large amount of heat is required to be removed from the core of a fast reactor and this requires a coolant with excellent heat transfer properties. Heat transfer properties are not

dependent on coolant velocity alone. Efficient cooling is possible even during a natural convection. Density of sodium changes significantly with respect to temperature and the range of temperature possible in a sodium system before reaching boiling point is very high. These features are important advantages in safety. Being liquid metal, sodium has the properties of an excellent heat transfer medium. It has a very high thermal conductivity from 85.8 W/m-K at 100°C to 63.9 W/m-K at 550°C. It also has a reasonably high specific heat (~1340 J/kg-K). It has a low melting point of 97.8°C and a high boiling point of 882°C. So, the coolant is at a low-pressure in the operating temperature range. Therefore, thin walled components are used and thermal stresses are more. In thermal reactors, where the amount of heat required to be removed per unit fuel pin length is less (40-50W/cm) compared to a fast reactor (450W/cm). Hence, pressurized water/ heavy water is sufficient as a coolant in thermal reactors whereas in a fast reactor, liquid metals with high thermal conductivity are required as coolant. Besides heat transfer capability, other properties such as,

- (i) Non-corrosive nature,
- (ii) Low neutron absorption cross section,
- (iii) Low moderation for fast reactors,
- (iv) Radiation stability,
- (v) Thermal stability,
- (vi) Low induced radioactivity,
- (vii) Low pumping power are preferable.

Sodium exhibits the following advantages over water

- (i) Very high film heat-transfer coefficient,
- (ii) Greater permissible temperature rise of coolant without involving pressure,

- (iii) Minimal corrosion of stainless steel by sodium,
- (iv) Removal of large amounts of heat from the fuel elements with minimum clad-coolant temperature difference.

One of the disadvantages of sodium is it is solid at room temperature. So preheating is required. It also becomes radioactive due to formation of Na-24. Further, it is highly reactive with air, and hence an inert cover gas is required for all sodium systems.

## **1.2 FLOW SHEET OF FBR**

The schematic of a typical pool type fast breeder reactor is presented in Fig.1.1 along with its inner and peripheral components. The fluid flow directions are also indicated. The core consists generally of a mixture of Pu and U in their oxide forms. Surrounding the core is a “blanket” of uranium oxide. Breeding takes place both in the core and the blanket. Primary sodium coolant flows through the core and the blanket to extract the fission energy. Fuel (Pu/U) in metallic, carbide, or nitride form is also feasible. The coolant has to convey the fission energy removed to the heat exchange system, such as a steam generator, eventually to convert heat energy into electrical energy. Sodium coolant, while passing through the core becomes radioactive, and so is not permitted to contact directly the steam generator. The primary sodium coolant gives its energy to an intermediate heat-exchanger (IHX), from which a secondary sodium loop takes the energy, which in turn is conveyed to the steam generator. In the reactor core, sodium is pumped by centrifugal pumps. Sodium inlet temperature to core is measured by six thermocouples. The temperature of sodium is measured at the outlet of every fuel sub assembly by two thermocouples. Neutronic flux is measured by triplicate in-core high temperature fission chambers. Flow of sodium is measured by eddy current flow meters at the outlet of primary sodium pump. The level of sodium in the reactor vessel is measured by

continuous level probes. The hot sodium coming out of the core enters into Intermediate Heat Exchangers. The arrangements of primary pump, reactor core, intermediate heat exchangers etc. are inside the main vessel as shown in Fig. 1.2. The pool type reactor does not have any penetration for piping and hence structurally more robust. The large mass of sodium attenuates transient temperature rise in the systems, providing adequate time for safety action.

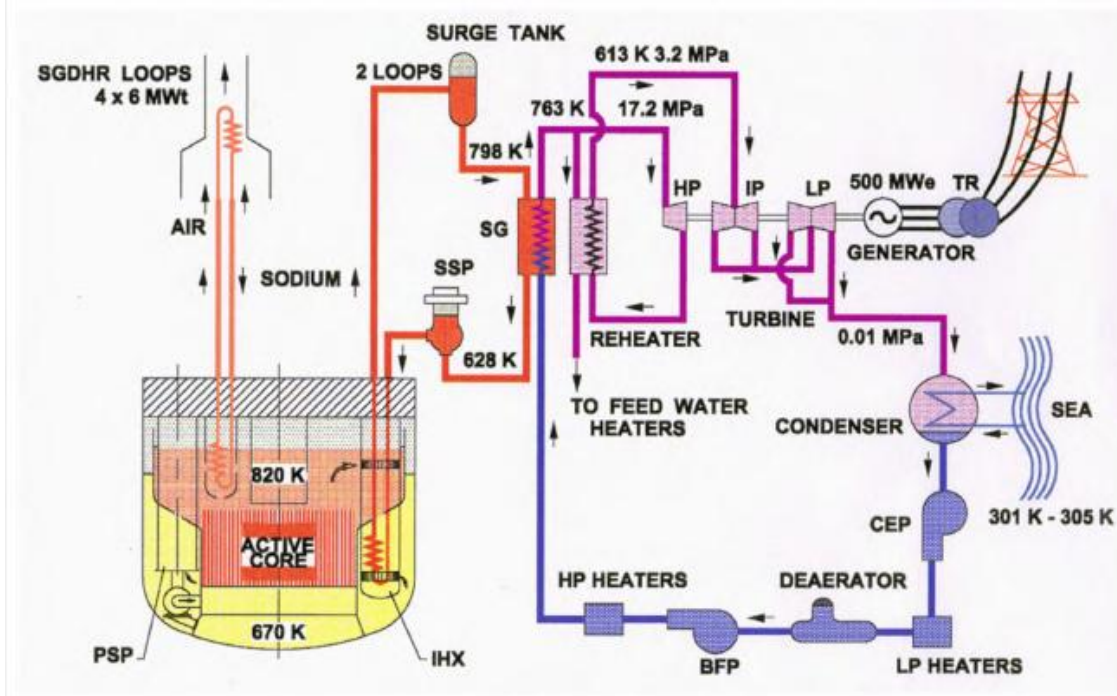
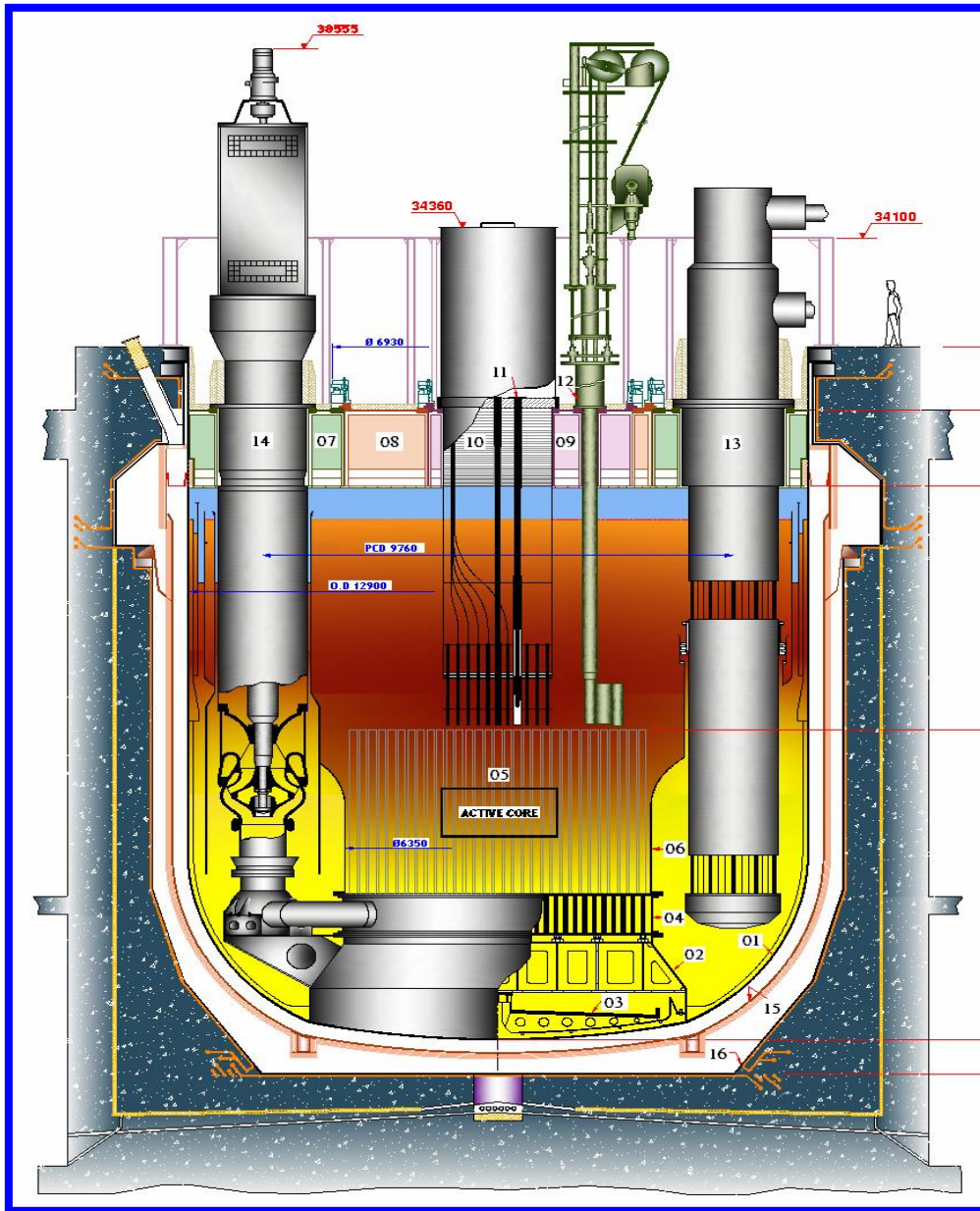


**Fig. 1.1 Flow sheet of a typical pool type FBR (Chetal et al., 2006)**

The primary sodium pool is divided into hot pool and cold pool by a thin structure called inner vessel. The main vessel is cooled by cold sodium to enhance the structural integrity. The core subassemblies (SA) are supported on the grid plate, which in turn is supported on the core support structure. A core catcher provided below the core support structure, is designed to take care if melt down of seven subassemblies and prevents the core debris from coming in contact with the main vessel. The main vessel is surrounded by the safety vessel, with a nominal gap of 300mm to permit robotic and ultrasonic inspection of the vessels. The safety vessel also helps to



**LEGEND**

- |                            |                                    |
|----------------------------|------------------------------------|
| 01. MAIN VESSEL            | 09. SMALL ROTATABLE PLUG           |
| 02. CORE SUPPORT STRUCTURE | 10. CONTROL PLUG                   |
| 03. CORE CATCHER           | 11. CONTROL & SAFETY ROD MECHANISM |
| 04. GRID PLATE             | 12. IN-VESSEL TRANSFER MACHINE     |
| 05. CORE                   | 13. INTERMEDIATE HEAT EXCHANGER    |
| 06. INNER VESSEL           | 14. PRIMARY SODIUM PUMP            |
| 07. ROOF SLAB              | 15. SAFETY VESSEL                  |
| 08. LARGE ROTATABLE PLUG   | 16. REACTOR VAULT                  |

**Fig. 1.2 Vertical sectional view of reactor vessel  
(Chetal et al., 2006)**

keep the sodium level above the inlet windows of the intermediate heat exchanger ensuring continued cooling of the core in case of a leak of main vessel. The inter space between main and safety vessel is filled with inert nitrogen. Each secondary sodium loop, each loop consists of one expansion tank with centrifugal pump, one surge tank, and a few steam generator modules. Heat transfer takes place from primary sodium to secondary sodium in intermediate heat exchanger. Hot sodium flows into surge tank and then to steam generator. After transferring heat to water, relatively cool sodium flows from steam generator to expansion tank. Here, submerged centrifugal secondary sodium pump pumps sodium into intermediate heat exchanger. Permanent magnet type flow meters are used to measure the sodium flow in secondary sodium circuit. A sample of sodium coming out of steam generator is analysed for the presence of hydrogen. Increase in hydrogen level will reveal leak in the steam generator modules. Superheated steam coming out of steam generator is passed into turbo-generator set for generating electricity. Spent steam is condensed back into water. After preheating with bleeding steam, water is pumped back into steam generator.

The instrumentation and control for sodium system are specialized in nature due to the requirements of measuring process variables at wide and high operating temperatures ranging from 150 to 650°C and in sodium environment. As a part of this research, new techniques have been developed in the field of sodium instrumentation applicable to FBR. These include,

- (i) a simple method for in-situ time constant estimation of core temperature sensors
- (ii) a direct imaging ultrasonic technique for Absorber Rod Drive Mechanism (ARDM)
- (iii) an indirect imaging ultrasonic technique for protrusion detection in core top
- (iv) development of a mutual inductance type sodium level measurement sensor with a new temperature compensation technique

In FBR, the most frequently monitored process variable is temperature and about 60% of the installed sensors are thermocouples. Much of the remaining instrumentation however is concerned with sodium levels and is necessary to ensure that the sodium coolant circuits are operated safely and under appropriate design condition. The enhanced scale and temperature levels of FBR's offer interesting and challenging issues in sodium process instrumentation. To tackle these issues, new instrumentation techniques have to be developed, which would virtually result in a new generation of sodium instrumentation. Some of these have been described in Evans (1966), Duncombe (1966 and 1984) and Davidson (1966).

### **1.3 IN-SITU TIME CONSTANT ESTIMATION OF CORE MONITORING THERMOCOUPLES**

As far as monitoring for core cooling is concerned, the major objective of monitoring devices is to find out flow reduction in any of the fuel subassembly and thereby to prevent large-scale under cooling of the SA, which may lead to fuel pin damage and possible reactivity addition in the core due to sodium boiling and fuel melting. While considering the requirements of instruments to supervise core cooling, it is necessary to consider various potential that are possible in the nuclear reactor. Table.1.1 lists down a series of events that lead to power increase in addition to those involving flow reduction. The instrumentation system should be amenable for easy maintenance and quick replacement, without impairing primary containment integrity. As already mentioned, the thermocouples (TC) placed above the SA outlet monitor outlet temperatures from the subassemblies. Temperature measurements are scanned at a predetermined interval by the computer. This surveillance is intended to monitor for any blockage occurring in any of the subassembly. The delay in taking a suitable safety action depends on computer cycle time, thermocouple response time and control rod shut down time.

**Table–1.1 Design basis events for core cooling**

GLOBAL	Upset	Inadvertent control rod withdrawal Argon bubble in Core Oil leakage into primary circuit Pump slow down
	Faulted	Primary pump seizure Loss of main heat transport loops Guillotine rupture of inlet pipe From pump to grid plate
LOCAL	Upset	Local blockages from fuel debris from failed pins
	Emergency	Fuel loading error Orifice assembly error Gross enrichment error
	Faulted	Local blockage from external debris Local enrichment error Gross inlet and out blockage of a S/A

Single subassembly plugging and consequent fuel melting is considered more probable than the whole core accidents in a fast reactor though both the events are of extremely low probability ( $10^{-4}/\text{ry}$  to  $10^{-6}/\text{ry}$ ). Protection against fuel subassembly plugging is provided at two levels, first in the design and the next in the detection and safety action. Gross blockages in a subassembly is avoided by providing radial entry for flow and by providing number of slots at two levels in the grid plate sleeve and at the subassembly foot. Also, at the top, gross flow blockage is prevented by providing blockage adaptors above the pins which will ensure 53% flow in the subassembly in the event of any falling object on the top of the subassembly as shown in Fig.1.3.

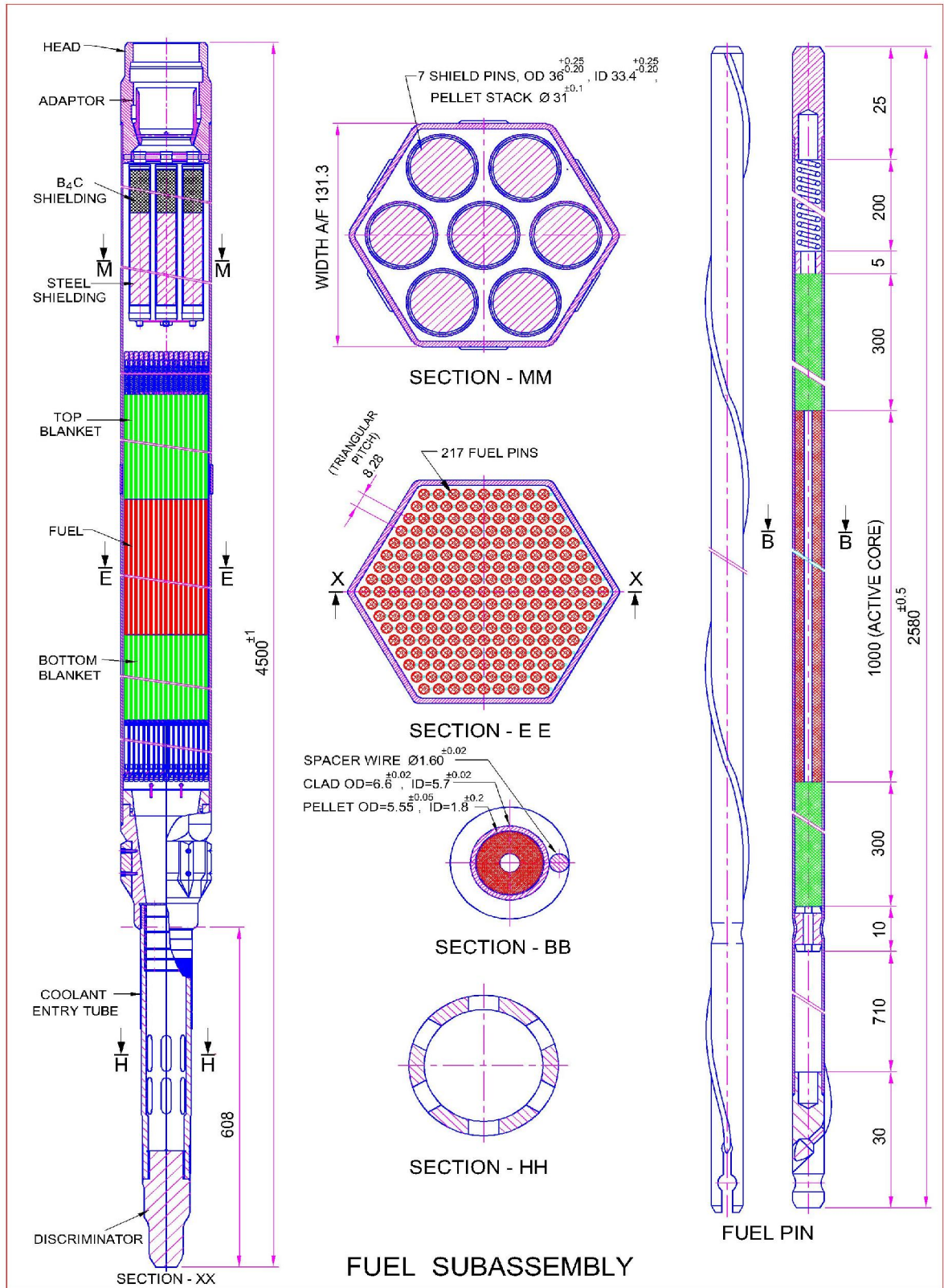


**Fig. 1.3. Fuel subassembly of medium size pool type FBR (Ravi et al., 2013)**

For any local blockage, it is ensured that the clad hot spot temperature shall not exceed 800 °C by the time safety action is taken by providing suitable detectable mechanism. General safety features of FBR plant can be broadly classified as inherent safety features and engineered safety features. Inherent safety features are available because of the chosen concept of the reactor system, choice of coolant and core characteristics that can inherently bring down the reactor to shut down state by introducing negative reactivity in the core with temperature/power increase. Some of the important engineered safety features are multiple radial entry sleeves for subassemblies, inertia provided on primary pump, core monitoring instrumentation etc. The classification of blockages and the limit on thermocouple response time is discussed below.

### **1.3.1 Classification of Blockages**

The blockages are classified as gross external blockage, local blockages within the FSA and total instantaneous blockage. Blockage in any form results in flow reduction and thereby increasing the sodium outlet temperature.

- ***Gross blockages of subassembly***

The gross error in a subassembly leads to disturbance of the design ‘power to flow’ ratio and may be initiated due to the following reasons:

- Incorrect positioning of a subassembly
- Inlet and outlet blockage of a subassembly

In correct positioning of a subassembly comes from loading a higher enrichment fuel subassembly to a lower enrichment subassembly position in the core or loading low flow zone subassembly in a high flow requirement region. Prior to loading in the reactor core, the enrichment is checked in the control post by gamma scanning and verifying enrichment number on the subassembly head. Also the foot profile is checked against the enrichment flow zone

category. Further, loading errors are detected by different combination of dimensions for coolant entry tube provided at the bottom discriminators for different core subassembly. If a subassembly is loaded in an unsafe position by mistake, then full insertion of subassembly is impossible due to this design feature and monitoring the top level of subassembly after loading onto grid plate helps in detecting wrong loading. Thus, monitoring of subassembly protrusion during fuel handling operation becomes very important, which is achieved by “ultrasonic under sodium viewing” system developed as a part of the current research. Also, the monitoring of outlet temperatures of the individual subassembly at low power by thermocouples mounted in the core cover plate acts as a backup for wrong loading of subassembly.

- ***Local blockages within subassembly***

For an internal local blockage, the immediate consequence is the reduction of flow due to increased resistance. Local blockages may be due to

- Pin deformation
- Failure of spacers
- Transport of debris to the pin-bundle from the coolant circuit and getting lodged in the space between pins.
- Fragments from failed fuel

Local blockages may be due to the fragments of fuel from failed fuel (active) or foreign particles transported from the coolant circuit (passive). Active blockages beyond certain sizes can be detected by Delayed Neutron Detector signal. For passive blockages, detection is difficult. The different mechanism for local blockage formation lead to different size, shape and physical property of the blockage. Even the geometry of the pin bundle affects the nature of the blockage

spread over a large radial area is unlikely. A failed wire or debris accumulation in a wire-wrapped pin-bundle would lead to a long thin blockage.

- ***Total instantaneous blockage***

It is defined as an instantaneous blockage at the inlet of subassembly at nominal operating conditions. It is considered as an envelope of all types of blockages which could evolve and can be taken as beyond design basis (BDB) event ( $< 10^{-6}/\text{Ry}$ ). The question of detection of this event has to be considered with a critical eye because it is physically impossible. That is to say that even if a total blockage occurs inside the subassembly, it cannot be instantaneous. Cover gas monitors indicate the fuel element failure, first this is followed by the emission of Delayed Neutron Detector signal as soon as the coolant makes contact with the fuel inside the failed fuel element. Even in the worst reactor conditions, the residual sodium flow is sufficient to provide significant Delayed Neutron Detector signal from the faulted subassembly, thereby allowing the early detection of the faulted subassembly. Still, the major task of the designers is to improve the performance and reliability of detection system. Two important specifications of the global detection system are the sensitivity and response time of the Delayed Neutron Detector system.

### **1.3.2 Need for Fixing Thermocouple Response Time**

The objective is to find out the suitable time constant for the thermocouple to bring the reactor into safe shut down under category II event, (with frequency of occurrence in the range of 0.01 - 1/year) but also to arrive at the allowable error band on time constant that can be tolerated to avoid any spurious SCRAM. The need to consider the tolerance on time constant arose from an incident that occurred in FBTR in which lowering of control rod (LOR) that was ordered on pump trip converted to safety control rod accelerated mechanism (SCRAM) leading

to reactor SCRAM (Vinolia,2008). On investigation, it was found that incident of LOR getting converted to SCRAM was due to varying times of thermocouples that give rise to spurious signals from computer. Though there is no LOR in pool type FBR, the need for the tolerance on time constant arises from power setback consideration. The criteria for fixing the time constant is

- Clad mid-wall temperature under hot spot condition shall be restricted to 800 °C under flow blockage condition
- Sodium temperature under hot spot condition shall be less than its boiling point

As explained in Annexure -1, timely detection of flow reduction and suitable safety action are possible when the time constant of the sensor is in the regime of 4 to 8 s. The time response measurement of the sensor is an important requirement to be observed in ensuring the time constant throughout the life of the reactor in the maintenance of nuclear reactor protection system.

Direct methods such as ‘loop current step response test’ and ‘off-on test’ give more precise results, but need special equipment for carrying out the test which interfere with the continuous reactor operation. Indirect methodology which is basically a noise analysis technique is the most practical one. It does not interfere with the reactor operation as the sensors do not have to be out of operation. Since the parameter identification depends on the noise characteristics, there are cases where indirect methodology is not suitable to predict the time constant of core monitoring sensors. Therefore, an alternate in-situ time constant measurement to obtain information about the dynamic behavior of the sensor with a minimal interference is preferred. This forms the motivation for development of a in-situ technique, This techniques standard signals (ramp or step signals) generated during operation of the nuclear power plant for in-situ time constant estimation.

## 1.4 UNDER SODIUM VIEWING FOR PROTRUSION DETECTION

As already explained, it is essential to ensure that the subassembly is properly located in its position during handling operations. As FBR uses opaque liquid sodium as the coolant, during in-service inspection, in-core structures of FBR cannot be visually examined using optical instruments, while those of water cooled reactor are visually examined. Therefore, in order to improve plant's integrity, under sodium viewing system are to be developed utilizing ultrasonic. Such systems do not need any sodium draining and yet are capable of viewing under sodium in-core structures. The main objectives of under sodium ultrasonic scanner are

- To scan the above-core plenum for detecting protruding subassemblies, Absorber Rod Drive Mechanism's and control rods before starting the fuel handling operation.
- To view the subassembly heads to assess the extent of growth or bowing.

In typical medium sized pool type fast breeder reactors, the fuel subassembly is hexagonal in shape. This geometrical shape is favorable to ultrasonic beam only for 30% of the core orientation. For the rest, the subassembly is in unfavorable orientation. Therefore, two methods of ranging are envisaged for finding the presence of an object in the above core plenum (i.e., the gap between subassembly head and central figure, see Fig.1.2). Receiving the echo directly from the projected object is known as direct imaging while the other one is indirect imaging using shadowing effect of protruded object on peripheral subassemblies. In this case, the peripheral subassemblies are circular in shape having 100 mm extra projection above any other subassembly and are located in the last row of the core. In the later technique,

significant changes in the echo pattern received from the peripheral subassembly have been observed due to the protruding object.

## **1.5 DEVELOPMENT OF SODIUM LEVEL SENSORS**

In FBR, argon cover gas blanket is maintained above the sodium free surface to accommodate volume changes of sodium as a result of its thermal expansion, due to various possible operating conditions of the reactor, as well as to avoid sodium-air contact through the numerous penetrations in the roof slab. Hence, a large primary sodium surface, which interfaces with argon, is formed as shown in Fig. 1.2. The secondary circuit also has a large number of free sodium-argon interfaces. This literature includes, surge tank, secondary sodium pump vessel, storage tank etc. Operationally, the levels at the pool region and secondary circuit must be measured continuously to know the gross sodium hold up in the primary circuit, to ensure that an adequate level is maintained at the heat exchanger inlet to prevent vortex formation and gas entrainment. This is also required to find out the entry of secondary sodium into primary due to the failure of intermediate heat exchanger tubes if any. Control of the relative level is important during normal operation, shut down condition and transient condition of the reactor operation. Consequently, a large number of measurements of high temperature sodium level sensors in general, at least one for every sodium/gas interface are mandatory from safety point of view. As an alkali metal, sodium is highly reactive with air and water and is incompatible with many commonly used engineering materials. In addition to the essential requirement of compatibility of the sensors used with liquid sodium up to a temperature of 823 K, the integrity of the system should be maintained even in the case of breach of the sensor. Hence, conventional instrumentation devices cannot be readily used in sodium systems. The above requirements necessitate development of special sensors for use in liquid sodium.

### **1.5.1 General Techniques for Level Measurement**

There are a number of methods for measuring liquid level, which are based on various physical principles. The usual method involving the use of float is not suitable for liquid sodium due to oxide deposits which impairs accuracy and achieving hermetic closure is difficult for mechanical transmission system. The use of ultrasonic waves using a thin strip wave guide has also been proposed in literature, but it leads to complicated electronics system. The principle of non-contact level probe of mutual inductance is known and is being used in FBTR (Srinivasan et al., 2006). But, the major disadvantage of the probe is, the temperature is not known with accuracy and is not uniform along the probe.

### **1.5.2 Challenges in Sodium Level Measurement**

Even though the traditional continuous level sensors used in small loop type FBR is also of non-contact type, working on mutual inductance principle, for large pool type FBR application, robust, longer length (~10m) level probes and simple temperature compensation technique with improved electronics having better accuracy are required. As the temperature gradient is more for longer probes, the traditional partial temperature compensation technique is not suitable for large size FBRs. In addition to that, the level probes used for shorter length cannot be used for longer level measurement, considering the insertion and withdrawal of the probe into the pocket. Therefore, it is required to improve the existing sensor to cater for the above requirements.

## **1.6 MOTIVATION FOR THE PRESENT STUDY**

Apart from safety requirements, instrumentation is also required as an aid to operator for monitoring the healthiness of a system and to provide valuable data to the designer to verify

the design and to improve upon it. Development of techniques for sodium instrumentation viz., core temperature measurement, under sodium ultrasonic viewing and sodium level measurements are the major focus of the research. The core temperatures are monitored by measuring the average outlet temperatures of sodium jets issuing from each fuel subassembly by two numbers of K type thermocouples mounted inside a thermowell. This system is intended to monitor for any blockage occurring in any of the fuel subassembly. The main requirement is timely detection of the event by an efficient and reliable instrumentation system. Typical time constant of the sensor is  $6\pm 2$  s as explained in Annexure-I. The spring constant of the gripper assembly varies with long term exposure of combination of heat and vibration, temperature cycle and mechanical shock. These conditions are termed as stressors (Hashemian, 2005). If the thermocouple is spring loaded into the thermowell (T/W), mechanical effects may change the insertion length or contact pressure and increase the size of the air gap in the T/W causing the response time to increase. Measurement of dynamic response of the sensor in installed condition is necessary to satisfy requirements on allowable response time for nuclear power plant.

The ultrasonic method is the only possibility for detecting the protrusion of reactor components, above the core top. The possible protruded objects in typical medium size pool FBR (Chetal et al., 2006) type consist of conical shape in absorber rod drive mechanism, tapered shape in control rod and hexagonal shape in subassembly head. Before resuming every fuel handling operation under sodium ultrasonic scanner is deployed to ensure that no components are protruded in the above core plenum before resorting to rotating the fuel handling plugs. The objects which are perpendicular to the ultrasonic beam will give back echo and indicate the presence of the object. Detecting the objects which are not favorable to

ultrasonic beam is the main challenge and a new technique has been developed as part of this thesis work.

The use of directly immersed probes as level sensors is not favorable because of their attendant practical difficulties, including dependence on sodium wetting and susceptibility to formation of oxide films. Therefore, the present research has been focused towards development of non contact electromagnetic level sensors of the mutual inductance type. These sensors are readily accessible for repairs and inspection as the level probe is mounted inside a pocket. For longer level probes, the temperature distribution along the sensor is not uniform, but measurement of level independent of temperature is necessary. Therefore, the current research is directed to design and develop longer level probe with improved temperature compensation technique.

## **1.7 SCOPE AND OBJECTIVES OF THE THESIS WORK**

The major area of research work is development of new techniques for sodium applicable to large size sodium cooled fast breeder reactors.

- The work aims at development of a new technique for in-situ estimation of time constant for core temperature monitoring sensors. The sensor consists of multiple thermocouples in a thermowell mounted above the fuel subassembly head mainly used for blockage detection in individual fuel subassemblies. The time constant of thermocouple probe has been modeled theoretically to understand the factors influencing the time constant. This method uses the safety Control Rod Accelerated Mechanism (SCRAM) or lowering of Control Rod (LOR) signals of the reactor along with the response of the central subassembly thermocouple as reference data.

- A detailed experimental study in water has been performed towards understanding the direct/indirect ultrasonic imaging techniques for protrusion detection of components above core top. To study the feasibility of detecting the absorber rods and their drive mechanisms using direct ultrasonic imaging technique, experiments are carried out for different orientations and profiles of the projected components. Pseudo three dimensional color images are developed towards protrusion detection.
- An indirect imaging technique has been developed and simulated in water. The experiments have been performed for detection of protruded objects which are unfavorable to ultrasonic beam using 0.6 MHz transducer as against 1 MHz transducer in sodium. This is to simulate the beam divergence effect equivalent to that of sodium. The development of suitable algorithm for detecting the protrusion and construction of ultrasonic images in an user friendly manner is the challenge of the research.
- Also, a personal computer based automatic scanning system, has been developed as a part of this research for acquisition and analysis of data.
- As longer length level probes are required for large capacity FBR application, development has been carried out in the sensor with a new temperature compensation technique. The probe is characterized in sodium for obtaining the optimum frequency and sensitivity. Further, parameterize studies are carried out for improving the sensitivity. The present development is towards level sensor which is easy to use, has improved accuracy of measurement and provides indication of level irrespective of temperature. As part of this, Mutual inductance type discrete level probes are developed and characterized in sodium.

## **1.8 ORGANISATION OF THE THESIS**

The first chapter is an introductory chapter and explains the background, and the need for the present research. Chapter-2 details the literature survey and conclusion from literature survey. Development of techniques for sodium instrumentation are discussed in the subsequent three chapters. The background, location of temperature sensor and mathematical modeling, and characteristic graph between variations in response time with contact pressure are established in chapter-3. Details of the in-situ time constant estimation and the validation of the procedure by applying it to FBTR are also elaborated in chapter-3. Chapter-4 deals with under sodium ultrasonic imaging for detecting the protruded object. Experimental simulation of the probable protruded objects of absorber rod drive mechanism, development of direct ultrasonic imaging techniques, construction of pseudo coloring images through a PC based automatic scanning system are presented in this chapter. Further, development of an algorithm for detecting the protruding objects having unfavorable orientation to ultrasonic beam, establishing experimental facility, validation of the algorithm by experimental simulation and image construction are also presented in this chapter. Chapter -5 highlights the performance evaluation of long length level probes and recent development of temperature compensation technique along with simplified electronics. Chapter-6 summarizes the results and major conclusions of thesis and presents future scope of research.

## **CHAPTER-2**

## LITERATURE REVIEW

Fast reactors are one of the promising future energy options. Due to their breeding potential they could utilize a maximum quantity of uranium/thorium for energy production. Fast Breeder Reactors (FBR) have a compact core with a large potential for volumetric energy production rate. To extract large heat flux without causing fuel melting and keeping clad temperature within its limits, liquid sodium is used as the coolant which has excellent nuclear and thermal properties. The Instrumentation and control for sodium system are specialized in nature due to the requirements of measuring process variables at wide and high operating temperatures ranging from 180 to 650°C and in hostile sodium environment. As a part of this research, new techniques have been developed in the field of sodium instrumentation applicable to FBR. These include,

(i) A new method for in-situ time constant estimation of core temperature sensors (ii) A direct imaging ultrasonic technique for Absorber Rod Drive Mechanism (ARDM),(iii) An indirect imaging ultrasonic technique for protrusion detection in core top and (iv) A mutual inductance type sodium level measurement sensor with a new temperature compensation technique. Important literature relevant to these domains is reviewed in this chapter.

### 2.1 CORE TEMPERATURE MONITORING SYSTEM

The power density in the fast reactor core is very high. If sufficient cooling doesn't take place, the clad temperature increases to a very high value and leads to clad rupture and to fuel melt down. Blockages in any form will lead to increase in subassembly temperature. Blockage detection incidents in various countries are discussed below.

Some of the instances where partial core melt down has happened are listed below. Fermi-1 suffered a partial fuel meltdown (Bertini, 1980) due to gross and total instantaneous blockage. This reactor accident was attributed to a piece of zirconium that obstructed a flow-guide in the sodium cooling system. Two of the 105 fuel assemblies melted during the

incident. To mitigate such an eventuality in FBTR, subassemblies were provided with semi radial entry through multiple holes (Srinivasan et al., 2006). Outlet blockages could occur if some object falls from the top over the subassembly. However the design of FBTR, subassembly head is such that total instantaneous blockage due to falling objects is impossible. To overcome the subassembly blockage at the top in FBTR, head and shoulder having 5 and 95% flows respectively are provided at the outlet. Another possibility of gross blockage was reported in French reactor, Super Phenix (Creys-Malville, 1982). A rubber packing at the inlet was left behind by mistake in the subassembly, which was subsequently loaded in the pile too. This was, however, detected by outlet temperature monitoring during start up. It generally requires very large blockage to effect substantial flow reduction as low as 10%. In the case of Indian PFBR, to prevent total flow blockage in fuel and blanket subassemblies, multiple layer, and multiple radial openings in the sleeves in grid plate and in the feet of all the core subassemblies have been provided (Chetal et al., 2006). Total blockage at the outlet of a fuel subassembly is ruled out due to the adaptor, which ensures alternate path (maximum flow 53%) for flow through side gap-holes.

French study with ABACUS (Fiorini et al., 1990) programme reveals that the external debris is essentially trapped at the bottom of the bundle. The debris concentration decreases from the bottom of the bundle due to the screening effect due to wire-wrap. In PFBR a long bottom plenum is provided which is likely to act as a screen for any debris entering the fuel subassembly. Japanese study (Koyama et al., 1991) in the formation of local blockage due to foreign materials also confirms this. An analysis of the available data reveals that the process of blockage formation of oxides and impurities is very slow compared with the general time scale of failure development. In the case of a cladding fault of one pin, the amount of material available is insufficient to cause any global blockage. At the same time, a large blockage in the fast reactor can occur only as a result of fuel release from the pin failure. An

oil ingress incident in the primary circuit has been reported in Prototype Fast Reactor, and BN-600 (Brear and Stanfield, 1991). The debris generated due to oil ingress then can be transported by sodium and gets lodged in subassembly causing partial blockage.

A temperature drifting phenomenon was observed in KNK-II reactor (Brockmann et al., 1990). The investigations indicate large areas of depositions structured like rough plasters on the fuel rods. These deposits changed the resistance which explains the temperature changes at the outlet of the fuel element. These incidents show the importance of the system and its capability to detect such blockage events.

The details of core monitoring sensors are presented in Table - 2.1. In Rapsodie reactor after 10 years of operation four thermocouples failed due to ingress of sodium into thermowell. All the other thermocouples had worked well and no drift on their outputs were observed. From Phenix reactor, it is reported that there are no changes in the characteristics of the thermocouples after 40 yrs of operation. In FBTR, all the core temperature monitoring thermocouples provided in thermowells have worked without any problem.

Considering the selection of sensors for core temperature monitoring system, Platinum RTD's are used in thermal reactors. For fast reactors platinum RTD is not suitable due to the following reasons

- Platinum undergoes transmutation in fast neutron irradiation environment and hence its temperature resistance characteristics change.
- Due to gamma radiation at the location of the core subassembly outlets, the RTD elements get heated. This leads to an error in temperature monitoring.
- RTD cannot be manufactured in small sizes as thermocouples and it has linear temperature range only upto 500 °C, whereas the temperature at subassembly outlet rises more than that.

For the UK reactor CDFR, ungrounded coaxial thermocouples with 50 ms time constant is used. As these thermocouples have special manufacturing technique and are difficult to replace, they are not selected. The other option is SS- Na thermocouple. These thermocouples are used on experimental basis to study temperature noise at the subassembly outlets. The studies have shown that the temperature noise depends on cross flow and position of the sensor. No fully dependable method has been evolved so far to analyse the thermal noise signal at the subassembly outlets, for subassembly blockage detection. Hence, mineral insulated SS sheathed ungrounded junction chromel-alumel thermocouples are widely used in FBRs.

For detection of partial blockage of subassemblies and incorrect loading of subassembly, slow response times of chromel-alumel thermocouples are acceptable. Studies carried out on the adequacy of the core temperature control system of Super Phenix in protecting the core in case of transient global leakage in any subassembly, had concluded that the time constants of the instrumentation has only marginal influence on the performance of the system (Gourdan , 1979).

The time response measurement of the sensor is an important requirement to be observed in ensuring the time constant through out the life of the reactor in the maintenance of nuclear reactor protection system. The need and methods for monitoring the response time of temperature sensors is discussed by Hashemian (2005). The measurements carried out in Brazilian Angra I nuclear power plant is discussed by (Iraci, 2007). This explains the direct and indirect methods for in-situ time constant measurement and their advantages and disadvantages. The proposed research is aiming at new indirect in-situ time constant estimation without interrupting the reactor operation.

**Table-2.1. Details of core monitoring system in Fast Breeder Reactors**

S.No.	Name of the reactor	Type of sensors	Method of installation	Time constant	Remark
1.	FBTR	SS sheathed mineral insulated Chromel-Alumel (Ktype) thermocouples (2nos)	Probes consisting of thermocouples in thermowells	6±2 sec	Experimental reactor T/Cs are replaceable (Pralad, 1985) (Uma Seshadri, 1989)
2.	RAPSODIE	SS sheathed mineral insulated Chromel-Alumel ungrounded (Ktype) thermocouples (2nos)	In thermowells		Experimental reactor T/Cs are replaceable
3.	Phenix	SS sheathed mineral insulated Chromel-Alumel (Ktype) thermocouples ungrounded (2nos)	In thermowells	4± 2 sec c	Demonstration Reactor T/Cs are replaceable (Creys, 1982)
4.	Phenix	SS-Na thermocouple	5 positions	>100 Hz	Demonstration Reactor (Argous, 1980 and Selvaraj, 1979)
5.	Super-Phenix	Probe in sodium K-type thermocouple 2nos ungrounded SS -- sodium Thermocouple (1no.)	T/C as integral part of Thermowell	6± 2 sec 1 sec >100 Hz	Commercial Reactor T/Cs not replaceable (Gourdon, 1979) (Trapp, 1990)
6.	PFBR	SS sheathed mineral insulated Chromel-Alumel (Ktype) ungrounded thermocouples (2nos)	Thermowell	6±2 sec	Commercial Reactor

## 2.2 ULTRASONIC IMAGING IN FBR

In the second part of the research, ultrasonic techniques (Crecraft,1983) have been used as a research tool to detect and ensure that no subassembly or Absorber rod Drive Mechanism (ARDM) protrude in the above core plenum before initiating the fuel handling operation. An Under Sodium Ultrasonic Scanner (USUSS) has been developed for deployment in pool type fast breeder reactor which is used to detect the protruding objects if any above the core top before every fuel handling operation. Also, a novel instrumentation tool for liquid-metal-cooled fast breeder reactor (LMFBR), under-sodium viewing (USV) systems has been developed, aiming at visualizing reactor core components. A report by (Griffin, 2009) provides a comprehensive review and assessment of current and past research and development efforts in various countries including U.S, U.K, Germany, Japan, India, Belgium and France in the domain of under-sodium viewing for LMFBR. The earliest application of under sodium viewing known as “Visus” was used in the Phenix reactor, which enables fuel assemblies to be observed during loading (Lions, 1974). Swaminathan, (1990) reports the use of under sodium ultrasonic viewing system for the Indian Fast Breeder Test Reactor.

In FBTR, after fuel handling operation in July 1995, Core cover plate Mechanism (CCPM) could not be lowered to normal working position from fuel handling position. Various operations resulted in the mechanism being struck at higher position above top of subassembly heads. The likely causes were attributed to mechanical obstruction at the top, below the core cover plate or within the mechanism. An ultrasonic viewer was used to scan the region below the core cover plate mechanisms to find out possible protrusion of subassembly beneath it (Rajendran, 1996). The mechanical obstruction below core cover plate was systematically ruled out using the ultrasonic scanner.

**Table-2.2 Literature related to Research and Development in Under-Sodium Viewing**

Sl. No	Name of the reactor/ Country	Sensor details	Purpose of imaging system
1.	Phenix , SuperPhenix/ France	<ul style="list-style-type: none"> <li>• VISUS two wave guides, one for transmission and one for receiving</li> <li>• Both filled with NaK, PZT transducer at upper part of waveguide</li> <li>• Operating frequency 1MHz.</li> </ul>	To ensure that no core assembly or control rod is above its normal level, before rotating the control plug and fuel handling arm. (Lions,1974)
2	Risley/UK	<ul style="list-style-type: none"> <li>• Ultrasonic transducer made of lead Zirconate</li> <li>• Operating temperature of 285°C having nickel diaphragm with 5 MHz transducer</li> </ul>	Used to study changes in the structural materials in the reactor caused by neutron irradiation (Griffin, 2009) (Hans, 1984)
3	FFTF/US	<ul style="list-style-type: none"> <li>• 27 transducers operating at 5MHz having gold coated surface</li> </ul>	Used to view objects less than a foot. In addition ranging capability can indicate equipment location upto 16 feet away where detailed picture cannot be produced at that distance (Hoitnik, 1975)
4	FBTR/India	<ul style="list-style-type: none"> <li>• PZT-5A lead Zirconate titanate crystal with nickel diaphragm</li> <li>• Operating at 2 MHz frequency at 180°C of sodium</li> </ul>	Used to scan the above core plenum to ensure no SA or ARDM protrude ( used as and when demanded) (Swaminathan, 1990)
5	Atomic Power Co./ Japan	<ul style="list-style-type: none"> <li>• PZT(also investigated LinbO3)</li> <li>• Operated at 220°C and frequency range is 4.5-5 MHz</li> <li>• Diaphragm in gold -coated invar. Matrix array 5 mm X 5 mm</li> </ul>	Volumetric inspection of structural materials (Junzo Taguchi, 1980) (Hirokazu Karasawa, 2000)
6	Prototype Fast Reactor/ Dounreay	<ul style="list-style-type: none"> <li>• Ultrasonic transducer made of lead Zirconate</li> <li>• Operating temperature of 285°C having nickel diaphragm 5 MHz transducer</li> </ul>	To assess fuel distortion in the reactor core. (Mcknight,1983), (Turnbull, 1991),(Barrett, 1984) (Fothergill, 1983),(Huang, 2004)
7	SNR300/ Germany	<ul style="list-style-type: none"> <li>• Ultrasonic transducer made of lead Zirconate</li> <li>• Operating temperature of 285°C having nickel diaphragm 5 MHz transducer</li> </ul>	Examining the instrument plate of the reactor. (Rohrbacher, 1974 and Hans, 1984)

A detailed survey of literature related to research and development in under sodium viewing is provided in Table-2.2. This literature survey discusses the various systems used in fast reactors for periodic in-service monitoring and inspections of the reactor core. France, U.K. and India have pursued the development of ultrasonic ranging systems using side viewing transducers having operating frequencies in the range of 1 to 2 MHz for fast reactors. The prime objective of the ranging system is to ensure none of the core assemblies protrude above the normal core level before starting the fuel handling operation. In Phenix and SuperPhenix, normally the protruded objects are cylindrical in shape which is geometrically favorable to ultrasonic beam. Efforts in other countries are focused towards ultrasonic imaging system to image the top of the core using 5 MHz ultrasonic transducer to measure the lateral shift i.e., bowing of fuel subassembly from its original location to assess core distortion. In the present research, both ranging and imaging (Swaminathan, 2012) are provided and special technique has been developed for detecting the objects which are unfavorable to ultrasonic beam.

### **2.3 DEVELOPMENT OF SODIUM LEVEL SENSOR**

The characteristics required for level sensors include (a) wide and high operating temperature with minimum weld joints, (b) should not depend on wetting effects and (c) should be robust to withstand cross flow during normal operation. Various level methods have been discussed in the literature. A new design of pulse-echo ultrasonic liquid level gauge is developed in UK (Gillespie, 1982 and Watkins, 1988) in which the ultrasonic pulse (here, a Rayleigh or a Lamb wave) travels down a metal bar or a strip towards the liquid surface, where through a double mode- conversion process and a special reflecting structure, a strong echo is generated which travels back up the bar to the receiving transducer. The ultrasonic sensor is located outside a sealed vessel. An experimental gauge operating over a liquid level range of 10 m was tested.

In Phenix, Mutual inductance type continuous level probe is used. The coils are of stainless steel wire, wound on an insulating refractory support. For discontinuous level measurement Resistance type level probes are used in Phenix and RAPSODIE reactor as discussed in (Lions, 1978). GEC supplier from UK is able to supply inductive level probe of 4000 mm long with an accuracy of 5 %. The mathematical model for inductive level probe gives an accuracy of 8 %. As the temperature compensation in level probe is complicated, obtaining improved accuracy is a challenge. Level measurement which is independent of temperature (Paris et al., 1976) and improving the sensitivity (Playfoot et al., 1976 and Kerwin, 1976) for inductive level sensor motivates the development of new temperature compensation technique with an accuracy of 1.5%.

The other option for level measurement is the RADAR type level sensor which is used in Dounrey reactor during decommissioning of the plant.

## **2.4 CLOSURE**

The following conclusions have been reached based on detailed literature survey:

- For detection of partial blockage of subassemblies and incorrect loading of subassembly, slow response times of chromel-alumel thermocouples are acceptable. K-type thermocouples are suitable for fast reactors. Therefore, development towards improving response time of sensors is not a priority area.
- In situ time constant estimation is used as surveillance in fast reactors. Reliable indirect method without disturbing the operation of the reactor is not reported in literature.
- For ultrasonic under sodium scanner, viewing of components which are far away inside the sodium has not been reported. Imaging of complex shapes using simple technique is also not discussed in published literature.

- For Mutual inductance type level sensors, longer length probes were not reported in open literature and the accuracy obtained was poor in this sensor due to complicated temperature distribution along the sensor.

As has been described in the chapter on Introduction, the current research topics are undertaken for study in order to bridge some of the gaps existing in the literature as noted above.

## **CHAPTER-3**

# **IN-SITU ESTIMATION OF TIME CONSTANT FOR CORE TEMPERATURE MONITORING THERMOCOUPLES**

## **3.1 INTRODUCTION**

As already mentioned, it is mandatory to monitor the sodium outlet temperature from every fuel subassembly for early detection of flow blockage. Sodium flow reduction in a subassembly could be detected and safety action can be initiated when the time constant of core temperature monitoring thermocouples is in the regime of 4 to 8 s. The transient response of a sensor depends strongly on its operating conditions, which often cannot be duplicated in bench tests. Moreover, the transient response may change during the service life of the sensor. Thus, an in-situ measurement of the response rate is necessary. The response time measurement of the core temperature sensor is an important requirement to be observed in the maintenance of nuclear reactor protection system. The time constant of a thermocouple sensor is defined as the time taken for the sensor to reach 63.2% of its steady state value for a step/ramp change in the external temperature. Therefore a simple in-situ time constant measurement method is devised to obtain information about the dynamic behavior of the sensor with minimal interference. This chapter discusses the construction of the sensor, theoretical modeling of the sensor, method of determining the time constant, estimation of precise time constant and validation of this method by applying to the Indian FBTR (Srinivasan et al., 2006).

## **3.2 PRINCIPLE OF OPERATION OF THERMOCOUPLE**

It is known that thermocouples operate under the principle that a circuit made by connecting two dissimilar metals produces a measurable voltage when a temperature gradient is imposed between one end and the other. Seebeck observed the existence of an electromotive force at the junction formed between two dissimilar metals (Seebeck effect).

Seebeck effect is actually the combined result of two other phenomena, viz., Thomson and Peltier effects (Jha, 2005).

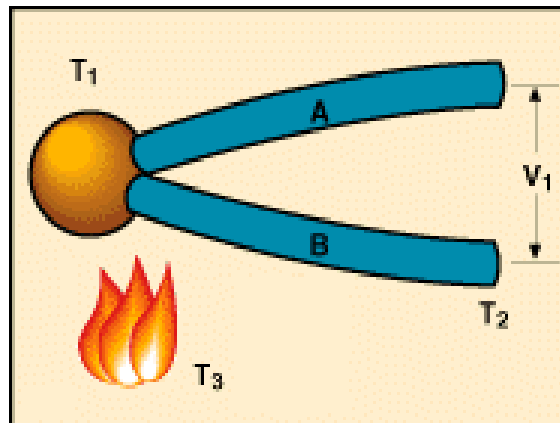


**Fig. 3.1a Principle of thermocouple**

Thomson observed the existence of an electromotive force due to the contact of two dissimilar metals at the junction temperature. Peltier discovered that temperature gradients along conductors in a circuit generate an electromotive force. The Thomson effect is normally much smaller than the Peltier effect. It is generally reasonable to assume that the electromotive force is generated in the wires, not in the junction. The signal is generated when temperature gradient ( $dT/dx$ ) is not zero. When the materials are homogeneous, then the thermoelectric power is a function of temperature only.

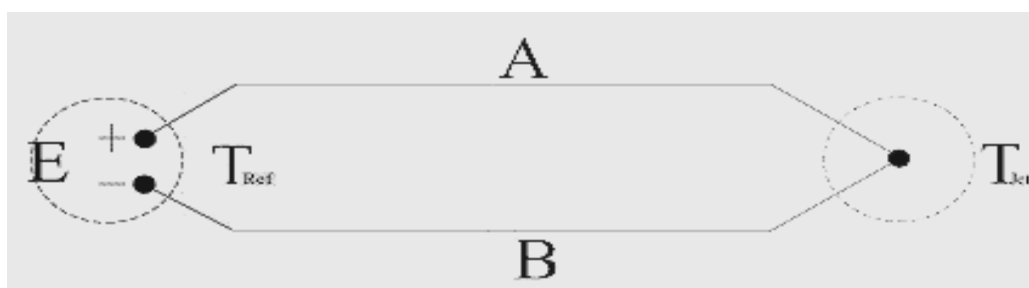


**Fig 3.1b Thermocouple circuit**

The electromotive force generated ( $E$ ) is given by,

$$E = \int_0^L \varepsilon_A \frac{dT}{dx} dx + \int_L^0 \varepsilon_B \frac{dT}{dx} dx \quad \text{-----} \quad (3.1)$$

If the wires are both homogeneous, then

$$E = \int_{T_{Ref}}^{T_{jn}} \varepsilon_A dT + \int_{T_{jn}}^{T_{Ref}} \varepsilon_B dT \quad \text{-----} \quad (3.2)$$

Where  $\varepsilon_A, \varepsilon_B$  - Seebeck coefficients

L - Length of the wire

If both wires begin at  $T_{Ref}$  and end at  $T_{jn}$ , then

$$E = \int_{T_{Ref}}^{T_{jn}} (\varepsilon_A - \varepsilon_B) dT \quad \text{-----} \quad (3.3)$$

For small temperature differences, we can use the average calibrations:

$$E = (\varepsilon_A - \varepsilon_B) (T_{jn} - T_{Ref}) = \varepsilon_{AB} (T_{jn} - T_{Ref}) \quad \text{-----} \quad (3.4)$$

During the last 30 years of FBTR operation, the variation in temperature with time is found to be only  $\pm 2^\circ \text{C}$  which is within the accuracy limit of thermocouple itself. Therefore, no noticeable drift is observed in K-type thermocouple which was verified during isothermal operating condition of the reactor. Since K-type thermocouple has been under sodium environment and has proven performance in FBTR at high temperature of operation ( $600^\circ \text{C}$ ), K-type thermocouple is found to be best suited for fast breeder reactor applications vis-a-vis N-type thermocouple wherein the performance has to be established under such hostile conditions.

### 3.3 SPECIFICATION OF THERMOCOUPLE

Temperature Range : 300 to 1200 K Chromel–Alumel Thermocouples

Sensitivity : Average sensitivity of thermocouple  $-40\mu\text{V/K}$

Response time : For 1 mm size mineral insulated SS sheathed ungrounded

junction Chromel-Alumel TCs installed in closed end thermowells, having  $6\pm 2$  sec can be achieved.

Accuracy : K type thermocouples can be supplied within class 1 of IEC-584, the tolerances are 0.4% from 375 upto  $1000^{\circ}$  C. These tolerances can be achieved with specified diameter and nature.

Radiation resistance : The thermocouple probe shall meet all functional requirements of 1019 nvt (40R-y at full power equivalent flux of  $1.55 \times 10^9$  nv). The minimum gamma dose that the thermocouple probe assembly shall withstand, meeting all the functional requirements is 946 MSv.

### **3.4 LOCATION OF SENSOR IN THE REACTOR**

In FBR, an uninterrupted cooling is ensured for each subassembly of the core at all power levels to remove the fission heat generated during normal conditions and decay heat generated during shut down conditions. A typical core configuration of Indian FBTR is shown in Fig. 3.2. Each fuel subassembly is instrumented with two thermocouples housed inside a thermowell. Ungrounded thermocouples are used to overcome the effect of common mode ground voltage. The thermowells are fixed to the stationary core cover plate (Fig. 3.3). Each thermowell is provided with a sleeve which is attached to a mobile core cover plate. During normal operation, the mobile core cover plate is driven down and sleeves come closer to the subassembly head. The axial distance between sleeve bottom and subassembly head is 15 mm during normal operation, guiding subassembly outlet sodium towards thermowell.

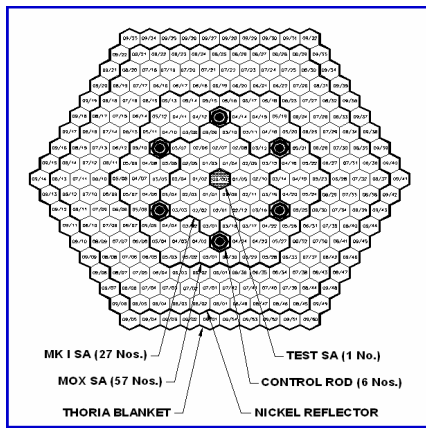


**Fig. 3.2 FBTR Core configuration**

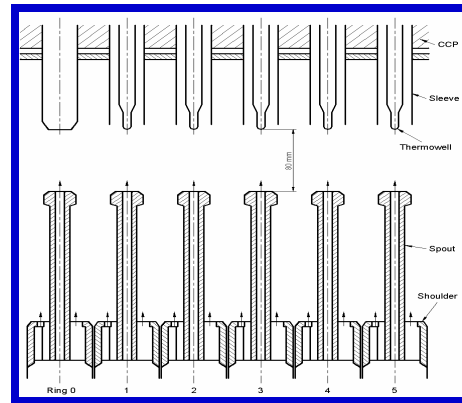


**Fig. 3.3 Location of thermocouples above fuel subassembly outlet nozzle**

But, during fuel handling operation when control plug rotation is essential the mobile core cover plate is moved upwards creating an axial distance of 80 mm between sleeve bottom and subassembly head, thus avoiding any mechanical interference between sleeves and subassembly heads. The central subassembly sodium outlet temperature is monitored by four 2 mm ungrounded K type thermocouples mounted on the central canal plug at a distance of 15 mm above the subassembly outlet nozzle. Reactor inlet temperature is monitored by three thermocouples located at pump suction in each loop. In order to achieve high and uniform core outlet temperature, the core of FBTR has been divided into three flow zones with decreasing flow from centre to periphery. The flow regulation is achieved by fitting an orifice plate at the subassembly head. The temperature signals from the core are scanned every second by Fault –tolerant Computer System as discussed in (Swaminathan, 1996 and 2004). Besides reliable sensing of temperature with the highest possible precision and fast response, long term reproducibility and minimum fatigue with extended lifetime within hostile environment are necessary. Hence, periodic online measurement of time constant of the sensor is essential.

### 3.5 SENSOR CONSTRUCTION

The sensor consists of two numbers of 1 mm diameter stainless steel sheathed Magnesium Oxide (MgO) insulated chromel-alumel ungrounded thermocouples which are tightly held in a dry thermowell by means of spring force of a gripper as shown in Fig.3.4. The gripper, which is machined out of a special steel (Autominyph) carries two sheathed thermocouples and runs through long guide tube into a leak tight thermowell (T/W) which is positioned just above the head of the fuel subassembly. The schematic of thermocouple probe is shown in Fig. 3.5.

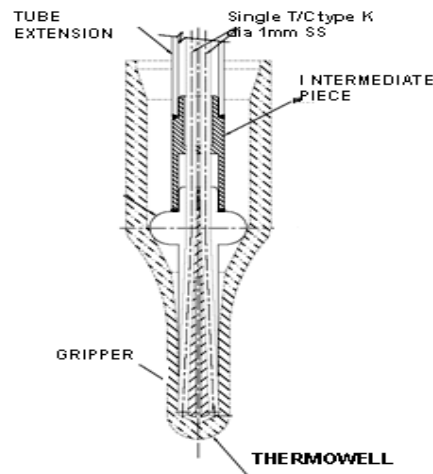


**Fig. 3.4 Details of Chromel Alumel thermocouple in thermowell**

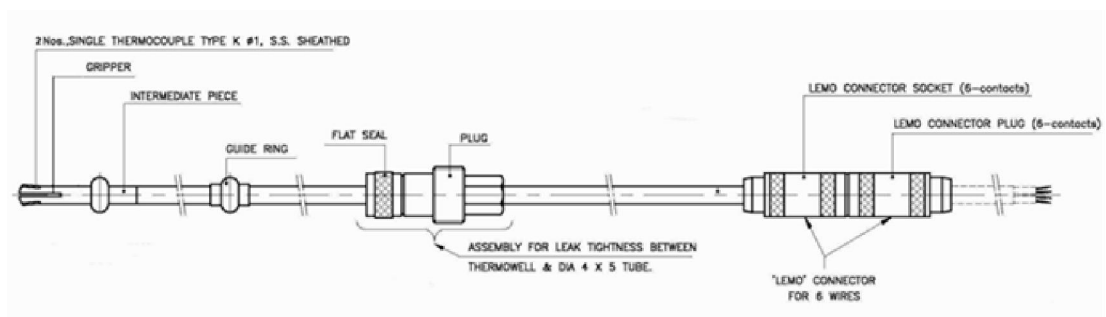


**Fig. 3.5 Details of thermocouple Probe**

The duplex thermocouples in each sensor is to achieve better reliability and hence the deviation in their time constants from each other is required to be minimum which is ensured

by stringent dimensional tolerances during fabrication. The spring constant of the gripper assembly varies with long term exposure to combination of creep, vibration, temperature cycling and possible mechanical shock. As the thermocouple is spring loaded into the thermowell, mechanical effects may change the insertion length or the contact pressure and alter the air gap in the thermowell causing the response time to change.

### 3.6 THEORETICAL MODELING OF THERMOWELL

In order to understand the factors influencing the response time, a mathematical modeling has been carried out. Time constant of temperature sensor is estimated based on the second order lumped parameter model by considering various thermal resistances and capacitances in the path of heat transfer from source to the thermocouple junction. From electrical analogy, an equivalent circuit diagram is prepared where the thermal resistance of thermo-well wall is split into two parts viz.,  $R_{w1}$  and  $R_{w2}$  as discussed in Prahalad et al., (1985). In order to get a sufficiently accurate picture of the response, it is necessary to include the effects of several resistances and capacities as shown in Fig. 3.6.

$$R_1 = R_c + R_{w1}$$

$$R_2 = R_f + R_{w2} \quad \text{where, } R_f = \text{film resistance of source}$$

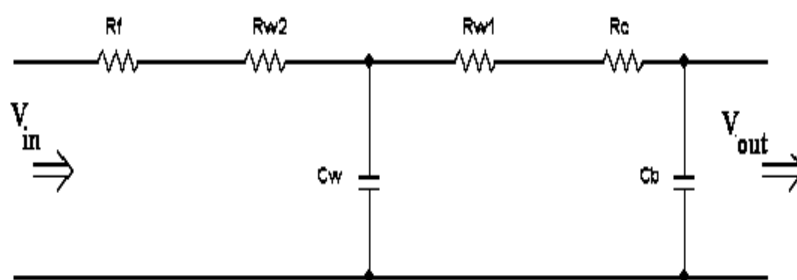


**Fig. 3.6 Equivalent circuit of thermocouple in thermowell**

$h$  = Heat transfer film coefficient of sodium ( $W / m^2-K$ )

$A$  = Contact area between the thermocouple and the inside of the well ( $m^2$ )

$R_{w1}$  = Thermal resistance offered by half of the wall thickness of the thermo-well given by

$$R_{w_1} = \frac{\ln\left(\frac{D_o}{D_m}\right)}{2\pi K} \cdot \frac{\pi(D_m + D_o)}{2A}$$

The derivation for heat flow through the thick walled cylinder is given in McCabe and Smith (1976). The heat transfer geometry is considered as a cylinder with inner diameter  $D_i$  and outer diameter  $D_o$  with equivalent contact length as, ‘Contact area of thermocouple/Mean diameter of the thermowell’.

$R_{w_2}$  = Thermal resistance offered by other half of the wall thickness of the thermo-well given by

$$R_{w_2} = \frac{\ln\left(\frac{D_m}{D_i}\right)}{2\pi K} \cdot \frac{\pi(D_m + D_i)}{2A}$$

$R_c$  = Thermal resistance of contact between the Stainless Steel sheathed thermocouple and the inside surface of thermo-well

$D_i$  = Inner diameter of thermowell (m)

$D_o$  = Outer diameter of thermowell (m)

$$D_m = \left\{ \frac{D_o^2 + D_i^2}{2} \right\}^{0.5}$$

$K$  = Thermal conductivity of stainless steel (W/m-k)

$C_w = C_2$  = Thermal capacitance of Well (J/K)

$C_b = C_1$  = Thermal capacitance of the thermocouple bulb (J/K)

It is assumed that the thermal resistance of thermocouple bead, thermal capacity of outside fluid film and radiation heat transfer are negligible.

Considering an electrical analogue, with  $V_i$  = Input voltage,  $V_o$  = Output voltage, we have

$$V_i = C_1 C_2 R_1 R_2 \frac{\delta^2 V_o}{\delta t^2} + (R_2 C_2 + R_2 C_1 + R_1 C_1) \frac{\delta V_o}{\delta t} + V_o \text{ -----(3.5)}$$

and

$$\frac{V_0(s)}{V_i} = \frac{1}{1 + (R_2C_2 + R_2C_1 + R_1C_1)s + R_2C_2R_1C_1s^2} \text{-----}(3.6)$$

Solution for the differential equation (3.5) is of the form

$$V_0 = Ae^{\frac{-t}{\tau_1}} + Be^{\frac{-t}{\tau_2}} \text{-----}(3.7)$$

where

$$\tau_1 = 0.5(R_2C_2 + R_2C_1 + R_1C_1) + \{0.25(R_2C_2 + R_2C_1 + R_1C_1)^2 - R_2C_2R_1C_1\}^{0.5}$$

and

$$\tau_2 = 0.5(R_2C_2 + R_2C_1 + R_1C_1) - \{0.25(R_2C_2 + R_2C_1 + R_1C_1)^2 - R_2C_2R_1C_1\}^{0.5}$$

If  $R_2C_1$  is small in comparison with  $R_2C_2 + R_2C_1$ , then the interacting effects are negligible and non interacting time components  $\tau_1$  and  $\tau_2$  are equal to  $R_2C_2$  and  $R_1C_1$  respectively. The transfer function for the second order non-interacting system is given by

$$\frac{V_0(s)}{V_i(s)} = \frac{1}{\{(1 + \tau_1s)(1 + \tau_2s)\}} \text{-----}(3.8)$$

But, both non interacting and interacting systems respond to a given input in exactly the same way and their lag is defined as

$$L = \tau_1 + \tau_2 = (R_2C_2 + R_2C_1 + R_1C_1)$$

For all possible ratios of  $\tau_2/\tau_1$  where  $\tau_1$  greater than or equal to  $\tau_2$ , the response is 63 % complete when the time elapsed after the step change is between 1.0L and 1.1L. For this system, then the thermal lag is a good approximation to the 63% response time as discussed in Coon and Roachesta (1957). Table-3.1 shows the estimated value of time constant using analytical modeling as a function of contact pressure. From the table, it is observed that the interacting effect ( $R_2C_1$ ) is negligible compared with  $R_2C_2$  and  $R_1C_1$ . Figure 3.7 pictorially depicts the relationship between contact pressures and time constant of the thermocouple in the thermowell, computed by the analytical modeling.

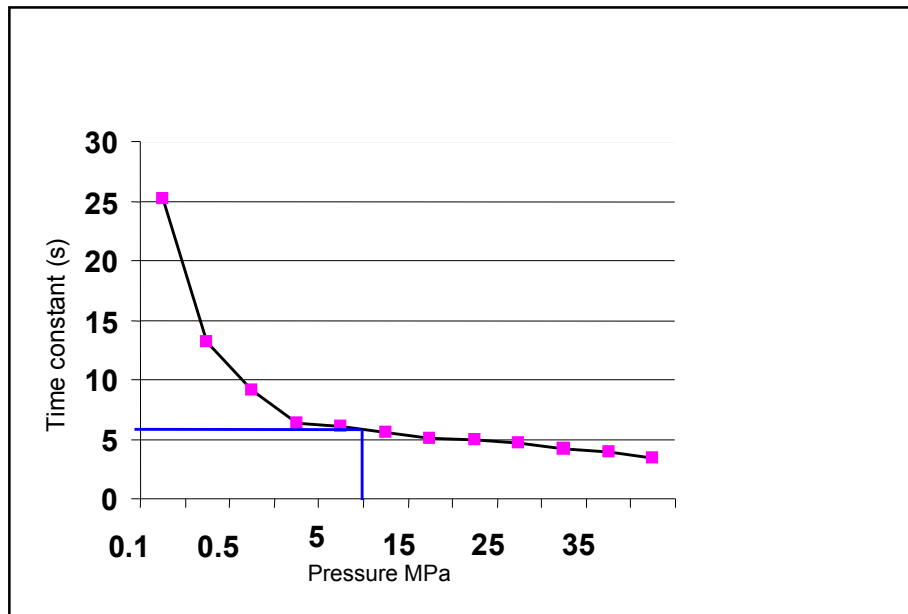


**Fig. 3.7 Dependence of time constant on contact pressure**

The contact resistance between thermowell and the thermocouple is selected from the hand book (Heat transfer Division, 1991) where the roughness of the stainless steel is 80 micron and is filled with argon at a pressure of 1.1 bar absolute. The analysis indicates that the time constant depends mainly on the contact pressure between thermocouple and the thermowell exerted by the gripper. As the pressure increases, the time constant decreases and vice versa. The theoretical value of contact pressure was found to be 10 MPa which was obtained from the dimensional details of the gripper and the thermowell. At this pressure, the time constant value is 5.6 s.

**Table-3.1 Estimation of time constant using analytical modeling**

$$R_f = 1/h_f A = 0.29488$$

Pressure (MPa)	Contact resistance $1/h_c$	$R_c = 1/h_c A$ (K/W)	$R_2$ (K/W)	$R_1$ (K/W)	$R_1 C_1$ (s)	$R_2 C_2$ (s)	$R_2 C_1$ (s)	$\tau_1$ (s)	$\tau_2$ (s)
0.1	0.001	1273.885	1.0556	1275.98	24.2797	0.9441	0.0201	24.3006	0.9433
0.25	0.0005	636.9427	1.0556	639.036	12.1598	0.9441	0.0201	12.1816	0.9424
0.5	0.0003	424.6285	1.0556	426.722	8.1198	0.9441	0.0201	8.14252	0.9415
1	0.0002	280.2548	1.0556	282.348	5.37261	0.9441	0.0201	5.39696	0.9398
5	0.0002	267.5159	1.0556	269.61	5.13022	0.9441	0.0201	5.15481	0.9396
<b>10</b>	<b>0.0002</b>	<b>242.0382</b>	<b>1.0556</b>	<b>244.132</b>	<b>4.64542</b>	<b>0.9441</b>	<b>0.0201</b>	<b>4.67059</b>	<b>0.939</b>
15	0.0002	216.5605	1.0556	218.654	4.16062	0.9441	0.0201	4.18656	0.9382
20	0.0002	203.8217	1.0556	205.915	3.91822	0.9441	0.0201	3.94463	0.9378
25	0.0002	191.0828	1.0556	193.176	3.67582	0.9441	0.0201	3.70278	0.9372
30	0.0001	165.6051	1.0556	167.699	3.19102	0.9441	0.0201	3.21945	0.9358
35	0.0001	152.8662	1.0556	154.96	2.94862	0.9441	0.0201	2.97804	0.9348
40	0.0001	127.3885	1.0556	129.482	2.46383	0.9441	0.0201	2.49613	0.9319

### 3.7 METHODS USED TO DETERMINE THE TIME CONSTANT OF SENSOR IN FBR

The thermocouple in thermowell is considered as a second order system by considering various thermal resistances and capacitances in the heat transfer path from environment to the thermocouple junction. Theoretical modeling shows that, the sensor is equivalent to two first order systems in series. The transfer function of the sensor is considered as a first order system where thermal lag (L) is summation of two time constants. The time constant is defined as the time required by the sensor to reach 63.2 % of the final temperature when step or ramp input is given. The transfer function can be used to determine

the dynamic response and identify the system's response time to any input such as step, a ramp or a sinusoidal.

For step input,

$$C(s) = K/(s*(1+ L s)) \quad (3.9)$$

where,  $L = \tau_1 + \tau_2$ .

Inverse Laplace transform gives the step response of the system

$$C(t) = T_{ss} + K(1-e(-t/ L )) \quad (3.10)$$

where, K is the amplitude of the step input and  $T_{ss}$  -steady state temperature.

Typical temperature response of thermocouple for various time constants of the sensor for step input is tabulated in Table 3.2 and the temperature vs time graph for various time constants for step input is shown in Fig. 3.8.

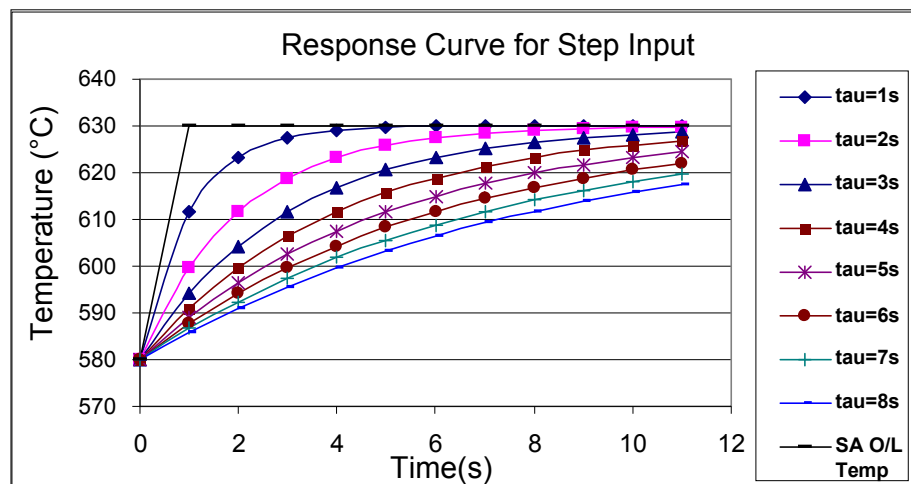


**Fig. 3.8 Computed sensor temperatures as a function of response time for step input**

**Table-3.2 Thermocouple reading for different time constant for a step input of 50 K**

Time (s)	Thermocouple readings (°C) for various values of $\tau$								SA exit Temperature (°C)
	1 s	2 s	3 s	4 s	5 s	6 s	7 s	8 s	
0	580	580	580	580	580	580	580	580	580
1	611.6	599.7	594.2	591.1	589.1	587.7	586.7	585.9	630
2	623.2	611.6	604.3	599.7	596.5	594.2	592.4	591.1	630
3	627.5	618.8	611.6	606.4	602.6	599.7	597.4	595.6	630
4	629.1	623.2	616.8	611.6	607.5	604.3	601.8	599.7	630
5	629.7	625.9	620.6	615.7	611.6	608.3	605.5	603.2	630
6	629.9	627.5	623.2	618.8	614.9	611.6	608.8	606.4	630
7	630.0	628.5	625.2	621.3	617.7	614.4	611.6	609.2	630
8	630.0	629.1	626.5	623.2	619.9	616.8	614.1	611.6	630
9	630.0	629.4	627.5	624.7	621.7	618.8	616.2	613.8	630
10	630.0	629.7	628.2	625.9	623.2	620.6	618.0	615.7	630
11	630.0	629.8	628.7	626.8	624.5	622.0	619.6	617.4	630

Similarly, for ramp input,

$$C(s) = R/s^2*(1+ Ls) \quad \text{-----(3.11)}$$

Inverse Laplace transform gives the ramp response of the system as

$$C(t) = T_{ss} + R*t -R* L (1-\exp(-t/ L)) \quad \text{-----(3.12)}$$

where, R is ramp rate and  $T_{ss}$  is the steady state temperature.

Typical temperature data for various time constants of the sensor for ramp input is presented in Table 3.3 and temperature Vs time graph of various time constants for ramp input is depicted in Fig. 3.9. In the case of FBTR, Lowering of Control Rod (LOR) is followed for normal shut down of reactor which generates a ramp input while Safety Control Rod Accelerated Mechanism (SCRAM) causes a step input. With this information, the response time of all the temperature sensors can be arrived at.

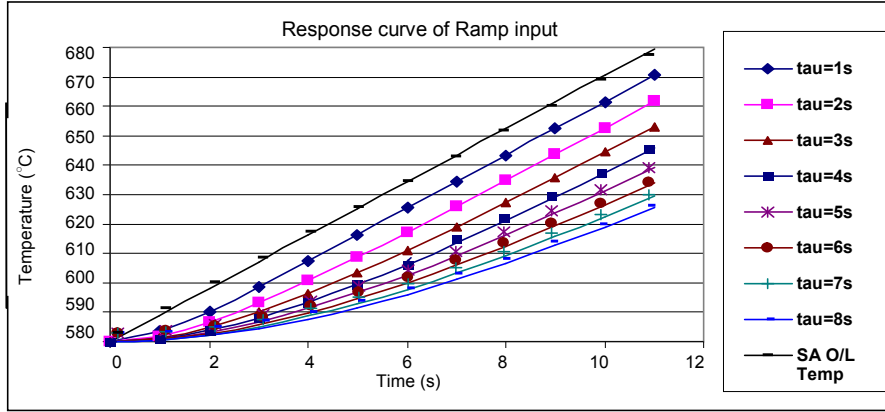


**Fig. 3.9 Computed sensor temperatures as a function of response time for ramp input**

**Table-3.3. Thermocouple reading for different time constants for ramp input**

Time (s)	Thermocouple readings (°C) for various values of $\tau$								Subassembly exit Temperature (°C)
	1 s	2 s	3 s	4 s	5 s	6 s	7 s	8 s	
0	580	580	580	580	580	580	580	580	580
1	583.34	581.93	581.36	581.04	580.85	580.72	580.62	580.54	589.05
2	590.29	586.67	584.90	583.86	583.19	582.71	582.36	582.09	598.1
3	598.59	593.11	590.01	588.07	586.75	585.80	585.08	584.52	607.15
4	607.37	600.59	596.24	593.34	591.30	589.80	588.64	587.73	616.2
5	616.33	608.69	603.27	599.46	596.68	594.58	592.94	591.63	625.25
6	625.36	617.17	610.88	606.23	602.72	600.01	597.87	596.13	634.3
7	634.41	625.88	618.91	613.50	609.31	606.01	603.35	601.17	643.35
8	643.47	634.74	627.23	621.18	616.36	612.48	609.31	606.69	652.4
9	652.54	643.67	635.76	629.16	623.76	619.34	615.68	612.62	661.45
10	661.61	652.66	644.44	637.38	631.47	626.54	622.41	618.92	670.5
11	670.67	661.68	653.23	645.79	639.43	634.03	629.46	625.54	679.55

### **3.8 ESTIMATION OF TIME CONSTANT OF CORE MONITORING SENSORS IN FBTR**

In order to validate the proposed method, the LOR data of FBTR is utilized. The central subassembly temperature measured by 2 mm ungrounded thermocouple having a faster response time (150 ms), is considered as the reference. The response to power variation obtained from neutronic signal is immediate and is shown in Fig. 3.10. It was observed that ramp signal is generated during LOR. The central subassembly thermocouple senses the temperature change 1 s later to the neutronic power signal as shown in Fig. 3.10. The ramp rate was estimated by matching the response curve of the central subassembly as shown in Fig. 3.11. The ramp rate taken from reference is  $3.74^{\circ}\text{C/s}$  and considering the duration of 3 to 9 s, the time constant is estimated for all other thermocouples. The time constant for ramp input is defined as the asymptotic response of the system delayed with respect to the input by the value that is equal to the time constant from the step response. During LOR, the normalized rate of change of power experienced by each subassembly is constant. Since mass flow rate is fixed for each subassembly, the rate of change of difference in subassembly outlet and inlet temperature is also constant for each subassembly.

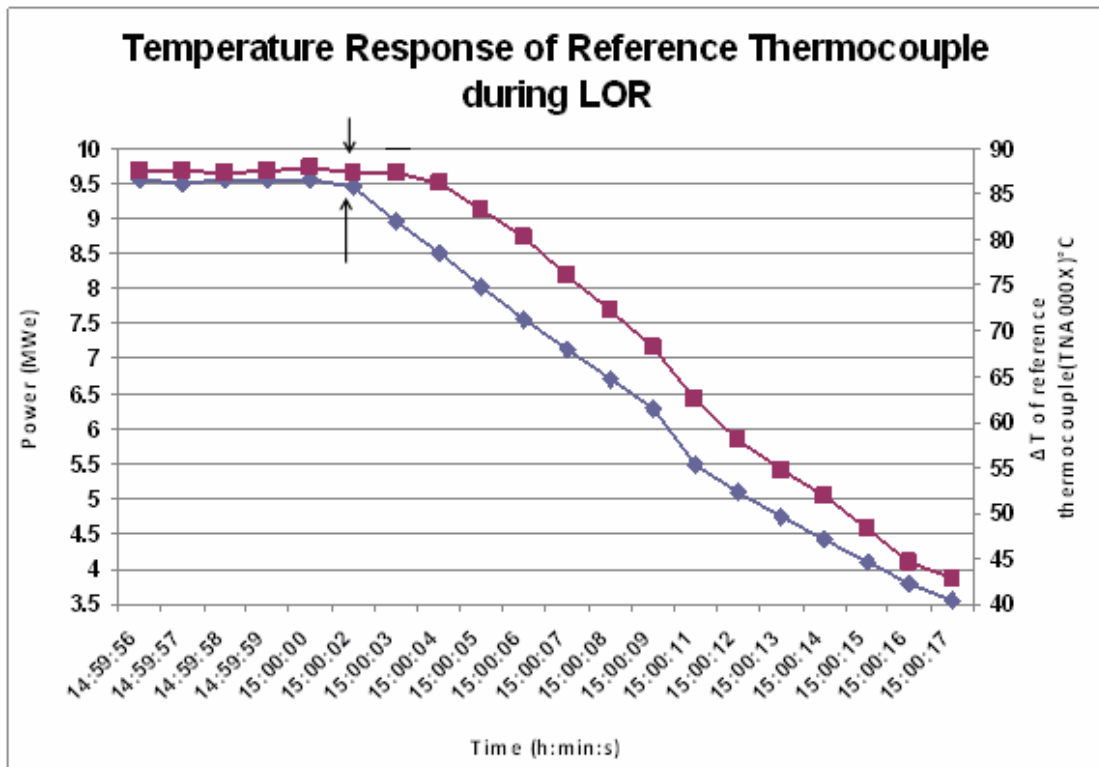


Fig. 3.10 Response of power and temperature of reference thermocouple during LOR

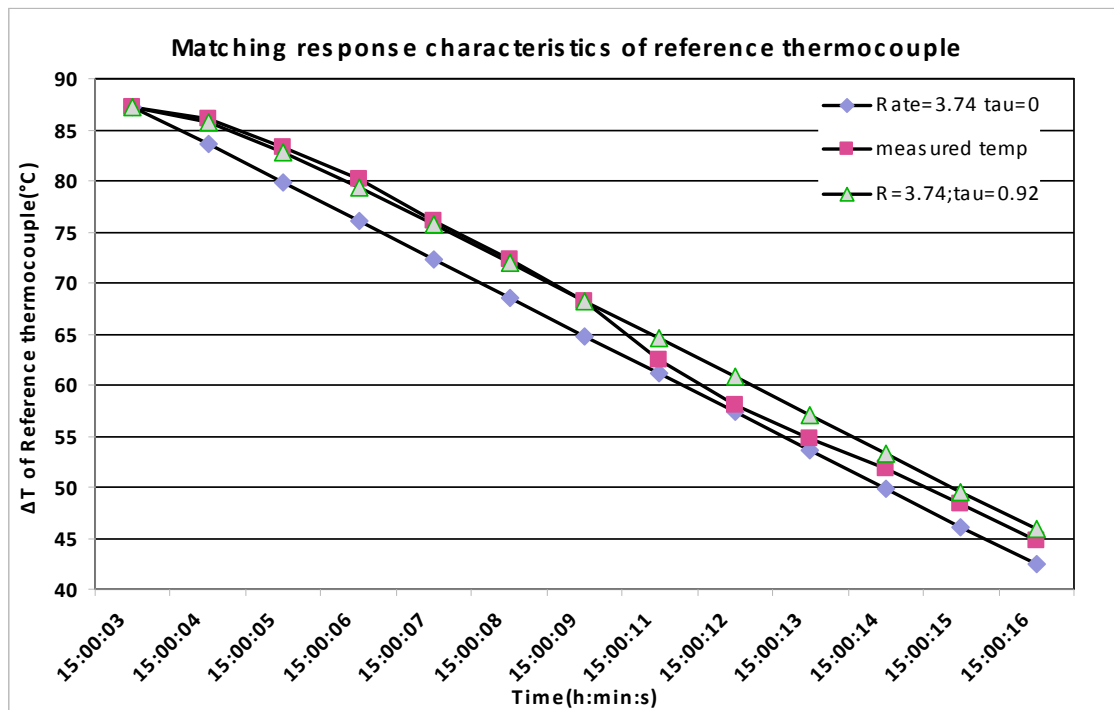


Fig. 3.11 Estimation of ramp rate

As the same ramp rate is experienced by all the subassemblies, the time constant of all the temperature sensors were estimated using an iterative method. The calculated values are presented in Table 3.4. The calculated time constant includes the time constant of the process as well as the time constant of the thermocouple.

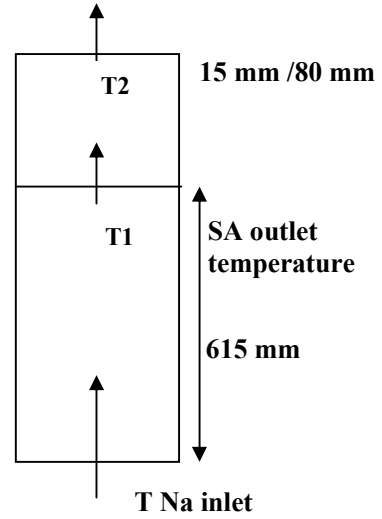
### 3.9 ESTIMATION OF PROCESS TIME CONSTANT

The time constant of the process was obtained by solving the thermal energy equation. Two control volumes are considered for calculation of sodium temperature and upwind scheme is implemented.

$$\dot{m} C_p (T_{na} - T_1) = (M C_p)_{ss+Na} \frac{dT_1}{dt}$$

$$\dot{m} C_p (T_{na} - T_1) = (M C_p)_{ss+Na} \frac{[T_1^n - T_1^o]}{\Delta t}$$

$$\dot{m} C_p (T_{na} - T_1^n) = (M C_p)_{ss+Na} \frac{[T_1^n - T_1^o]}{\Delta t}$$



Grouping  $T_1^n$

$$T_1^n \left[ \dot{m} C_p + \frac{(M C_p)_{ss+Na}}{\Delta t} \right] = \dot{m} C_p T_{na} + \frac{(M C_p)_{ss+Na}}{\Delta t} * T_1^o$$

$$T_1^n = \frac{\dot{m} C_p T_{na} + \frac{(M C_p)_{ss+Na}}{\Delta t} * T_1^o}{\dot{m} C_p + \frac{(M C_p)_{ss+Na}}{\Delta t}} \text{-----3.13)}$$

$$T_1^0 = T_{na}^0$$

$$T_1^n = T_1^0$$

Where

$$(M C_p)_{ss+Na} = (M C_p)_{ss} + (M C_p)_{Na}$$

Where

$T_1$	= Core outlet temperature (ramp rate is experienced here)
$T_2$	= SA top temperature
$T_1^0$	= SA top temperature at a previous instant
$T_1^n$	= SA top new temperature
$\dot{m}$	= Mass flow rate (kg/s)
$M_{ss}$	= Mass of SS structure (kg)
$M_{Na}$	= Mass of sodium (kg)
$(C_p)_{Na}$	= Specific heat capacity of sodium (J/kgK)
$(C_p)_{ss}$	= Specific heat capacity of SS (J/kgK)
$T_2$	= Temperature at 15 mm above SA top

To find out the temperature at 15 mm/80 mm above SA top

$$T_2^n = \frac{\dot{m} C_p T_1^n + \frac{(MC_p)_{ss+Na}}{\Delta t} \cdot T_2^0}{\dot{m} C_p + \frac{(MC_p)_{Na}}{\Delta t}}$$

$T_1$	= SA top temperature
$T_2^0$	= 15mm/80mm above SA top temperature (previous value)
$T_2^n$	= 15mm/80mm above SA top temperature (new value)

The ramp rate generated is experienced at the core top. The temperature at the centre of the core will be absorbed by the stainless steel structure and the volume of sodium. This contributes a time constant which is called the process time constant. The volume of SS and sodium is computed starting from the core centre to the top of the SA and then 15mm and 80mm above the SA top where bare thermocouples and thermocouple in thermowell are placed respectively. Typical FBTR fuel subassembly is shown in Fig. 3.12. blanket portion, shoulder portion and neck of the subassembly. Calculation is made for Zone-1 and Zone-2 as flow in these zones are different. Table 3.4 consists of time constant and temperature profile at subassembly top. Figure 3.13 presents the process time constant for Zone-1 by matching the response curve. Table 3.5 gives the temperature profile and time constant for Zone-2. Figure 3.14 provides the time constant for Zone-2.

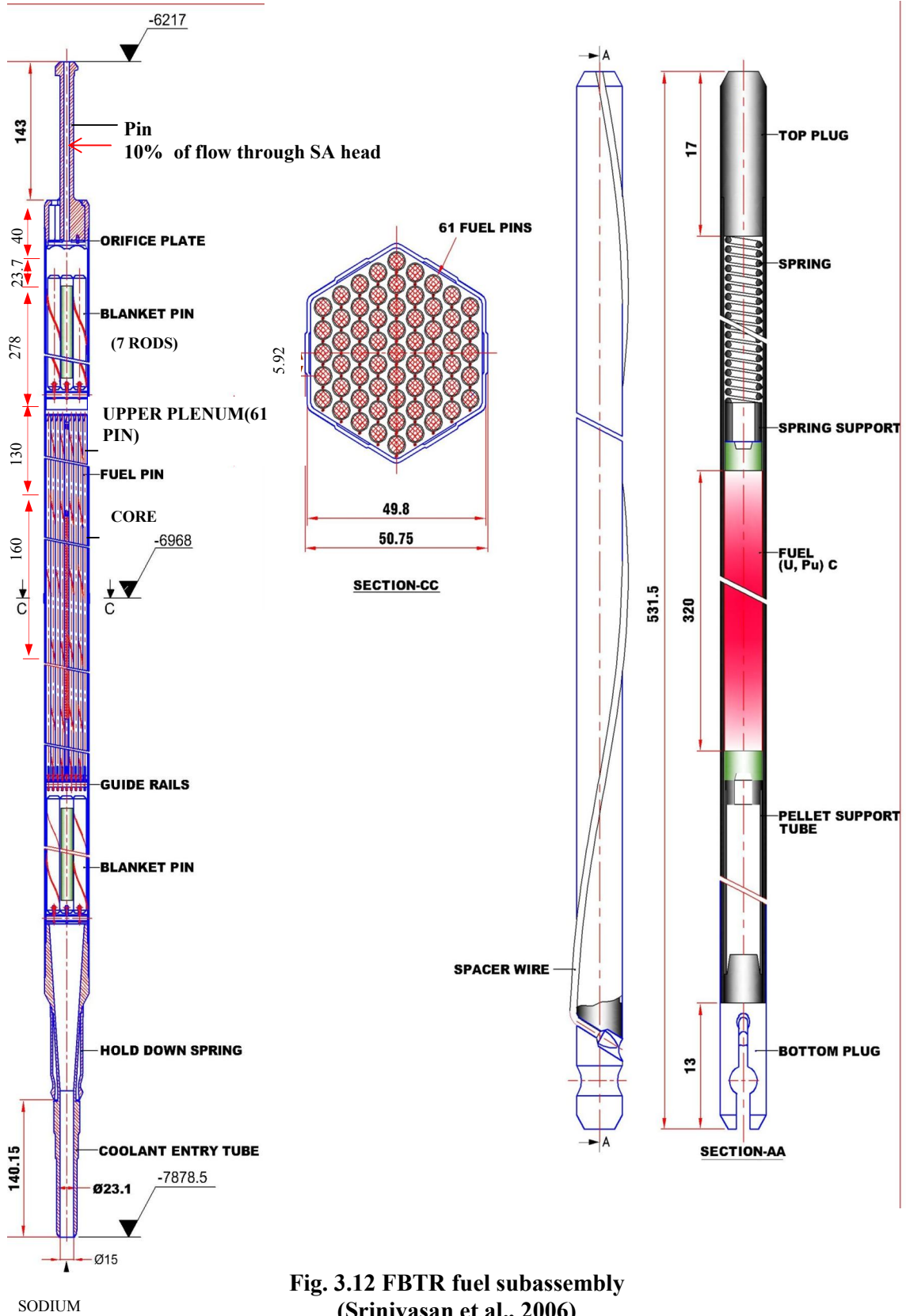
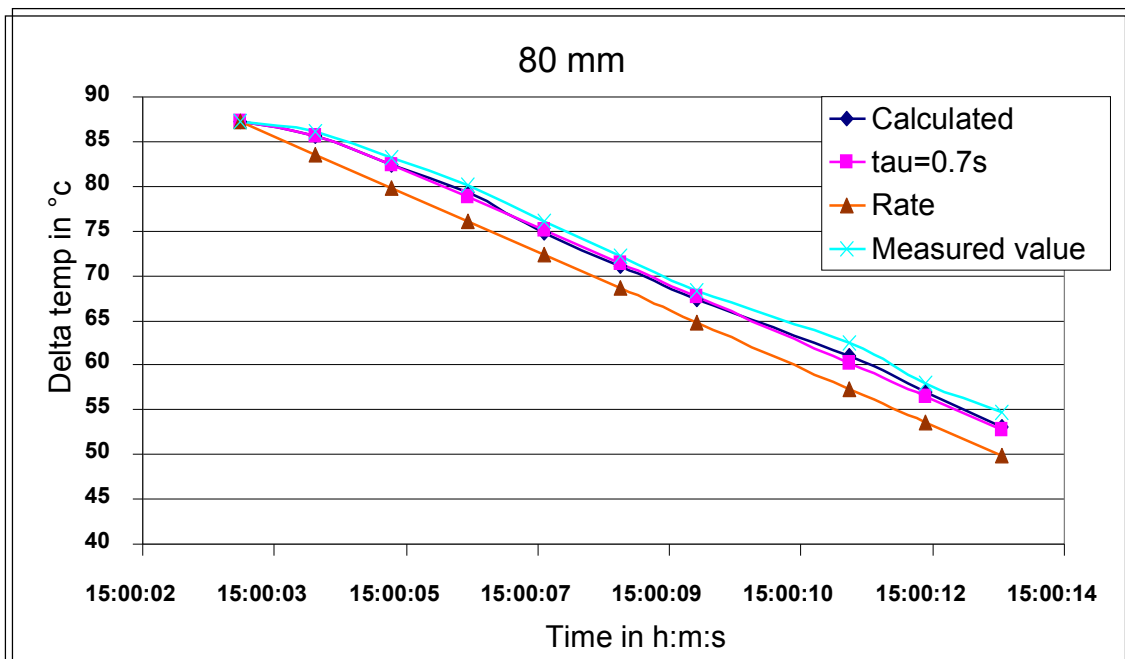


Fig. 3.12 FBTR fuel subassembly (Srinivasan et al., 2006)

**Table-3.4 Time constant and temperature profile for Zone-1**

Time constant (s)		0.64	0.66	0.7
Time (h:m:s)	Rate (K/s)	Subassembly top	Temperature at 15 mm	Temperature at 80 mm
15:00:03	87.274	87.274	87.274	87.274
15:00:04	83.534	85.354	85.426	85.460
15:00:05	79.794	81.958	82.082	82.143
15:00:06	76.054	78.283	79.426	79.496
15:00:07	72.314	74.55	74.703	74.777
15:00:08	68.574	70.817	70.967	71.040
15:00:09	64.834	67.078	67.227	67.352
15:00:11	57.354	59.598	59.748	59.822



**Fig. 3.13 Process response time for Zone-1**

**Table-3.5 Time constant and temperature profile for Zone-1I**

Time constant		0.8s	0.82s
Time (h:m:s)	Rate (K/s)	Subassembly top	80 mm
15:00:03	87.274	87.274	87.274
15:00:04	83.534	85.730	85.732
15:00:05	79.794	82.730	82.731
15:00:06	76.054	79.640	79.641
15:00:07	72.314	75.234	75.235
15:00:08	68.574	71.681	71.682
15:00:09	64.834	67.932	67.933
15:00:11	57.354	61.622	61.623

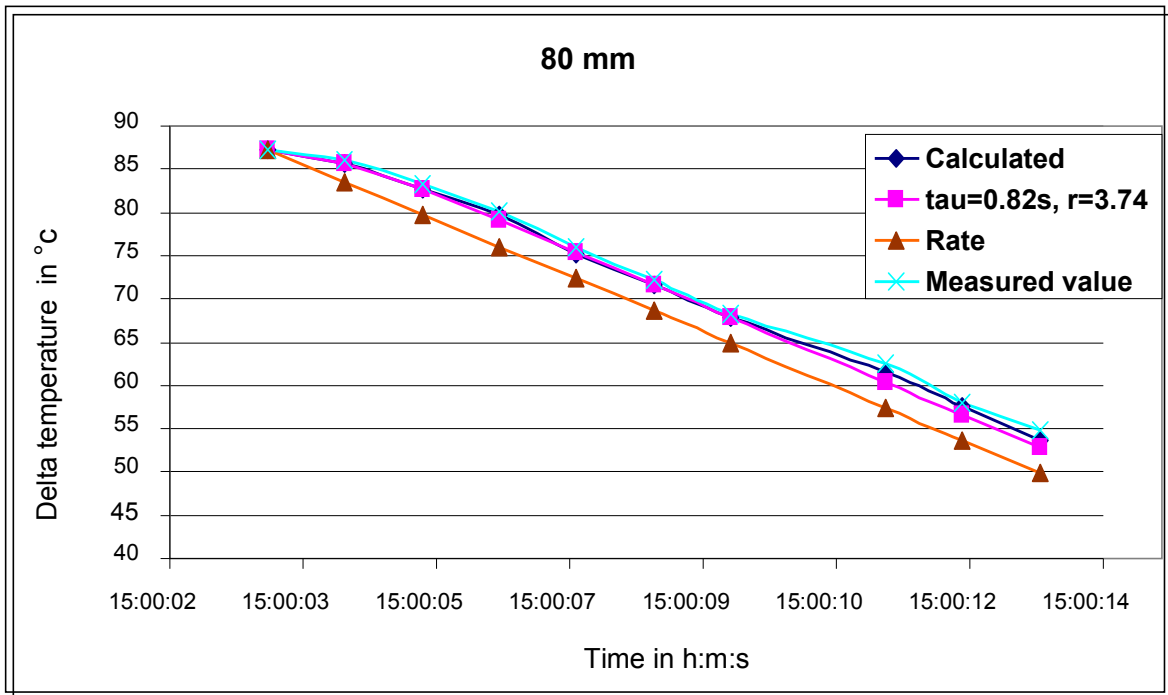


**Fig. 3.14 Process response time for Zone-II**

After finding  $T_2$ , temperatures at 15 mm above SA top and 80 mm above subassembly top and time constant have been estimated. Finally, the actual time constant of the thermocouples is estimated by subtracting the process delay as given in Table 3.6. Two different data sets measured in the reactor, viz., set – 1 (2007 data) and set – 2 (2012 data) have been used. Table 3.5 corresponds to 2007 data set while Table 3.7 corresponds the time constant estimated by using 2007 and 2012 data sets.

**Table-3.6. Estimated time constant of thermocouples (process time subtracted)**  
**(2007 data)**

T/C No	Time const (s)	T/C No	Time const(s)	T/C No	Time const(s)	T/C No	Time const(s)
<b>Ring-1</b>		TNA011X	7.9	TNA022Y	7.8	TNA033Y	6.3
TNA001X	5.32	TNA011Y	6.22	TNA023X	7.3	TNA034X	4.6
TNA001Y	4.46	TNA012X	6.89	TNA023Y	<u>10.8</u>	TNA034Y	5.7
TNA002X	6.55	TNA012Y	3.52	TNA024X	<u>8.6</u>	TNA035X	7
TNA002Y	7.34	TNA013X	4.1	TNA024Y	5.5	TNA035Y	4.4
TNA003X	4.56	TNA013Y	5.44	TNA025X	<u>8</u>	TNA036X	<u>10</u>
TNA003Y	4.87	TNA014X	4	TNA025Y	4.4	TNA036Y	4.9
TNA004X	4.89	TNA014Y	<u>8.44</u>	TNA026X	6.4		
TNA004Y	7.19	TNA015X	3.5	TNA026Y	<u>8.2</u>		
TNA005X	5.09	TNA015Y	<u>12.1</u>	TNA027X	<u>8.4</u>		
TNA005Y	5.84	TNA017X	4.64	TNA027Y	5.6		
TNA006X	4.17	TNA017Y	3.84	TNA028X	6.7		
TNA006Y	4.78	TNA018X	<u>9.09</u>	TNA028Y	5.1		
<b>Ring-2</b>		TNA018Y	3.2	TNA029X	6.6		
TNA007X	<u>8.39</u>	<b>Ring-3</b>		TNA029Y	<u>9.5</u>		
TNA007Y	6.39	TNA019X	4.89	TNA030X	4.9		
TNA008X	7.55	TNA019Y	5.34	TNA030Y	<u>10</u>		
TNA008Y	4.64	TNA020X	7.49	TNA031X	<u>13.9</u>		
TNA009X	<u>8.84</u>	TNA020Y	5.5	TNA031Y	6		
TNA009Y	4.64	TNA021X	6.82	TNA032X	<u>9</u>		
TNA010X	6.84	TNA021Y	<u>11.69</u>	TNA032Y	<u>13.3</u>		
TNA010Y	4.39	TNA022X	7.7	TNA033X	<u>11.5</u>		

Ring refers to various flow zones of FBTR fuel subassemblies. The indices X and Y refer to two thermocouples housed inside a common thermowell.

**Table-3.7. Estimated time constant of thermocouples  
(process delay subtracted)  
(2012/2007 data)**

Thermocouple Number	Time Constant in s	
	2007 data	2012 data
<b>TNA 007X</b>	8.39	8.32
<b>TNA 009X</b>	8.84	9.3
<b>TNA 015Y</b>	12.1	8.63
<b>TNA 021Y</b>	11.69	10.2
<b>TNA 023Y</b>	10.8	10.97
<b>TNA 025X</b>	8.0	12.82
<b>TNA 028X</b>	6.7	12.28
<b>TNA 029Y</b>	9.5	8.57
<b>TNA 030Y</b>	10.0	9.62
<b>TNA 033X</b>	11.5	11.61
<b>TNA 036Y</b>	10.0	9.14

### **3.10 UNCERTAINTIES IN TIME CONSTANT MEASUREMENT**

The estimation of time constant of thermocouple consists of two parts.

- (i) The measurement of time constant of the thermocouple along with process delay
- (ii) Calculation of time constant of the process delay from core centre to subassembly top

For estimating the error in time constant of thermocouple, error has to be calculated in two steps. Error in estimation of time constant of thermocouple along with process delay is obtained from the equation

$$T_m = (T_{SS} - R t) + R \tau (1 - e^{-t/\tau}) \quad \text{-----(3.14)}$$

where,  $t = t_1 - t_2$

$T_m$  = Measured SA outlet temperature at  $t_2$

$T_{SS}$  = Steady state temperature at  $t_1$

R = the ramp rate

Error in thermocouple measurement = 0.4 % of reading

Error in scan interval = 1 millisecond

The error obtained for time constant of thermocouple with process is 3.1%. The detailed calculation is explained in Annexure – 2.

Error estimation for finding out the process delay is obtained from the governing equation using numerical approach

$$T_2^n = \frac{\dot{m} C_p T_1 + \left[ \frac{(MC_p)_{SS} + (MC_p)_{Na}}{\Delta t} \right] \cdot T_2^o}{\dot{m} C_p + \left[ \frac{(MC_p)_{SS} + (MC_p)_{Na}}{\Delta t} \right]} \quad \text{-----(3.16)}$$

Error in  $C_{PSS}$  and  $C_{Pna}$  = 1.5 %

Error in flow = 2 %

Error in mass of sodium and stainless steel = 0.1 %

The error in temperature estimation for 80 mm above the subassembly top is 0.35% of the reading. The error in process time constant is found to be of the order of 4.2%. And detailed calculation is shown in Annexure-2. Total error in time constant estimation after subtracting the process delay is 4.12 %.

### 3.11 RESULTS AND DISCUSSION

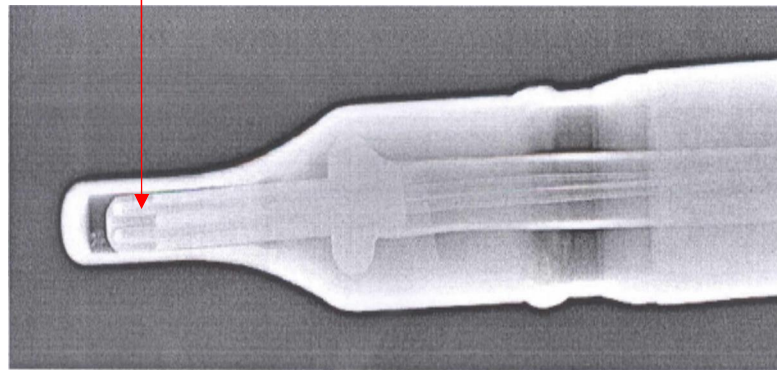
For small ramp rates of 3 to 9 s, the calculated time constants are in the range of 3 to 14 s. Power variation due to LOR is immediate and ramp starts at 15:00:02 s (Fig. 3.13). The thermocouple signal started changing after 1 s which is due to computer scan time of 1 sec. The time constant of the reference thermocouple is determined to be 0.92 s which includes the process delay and the time constant of the thermocouple. Process time constant is estimated for the temperature to reach from the centre of the core to the bottom of the thermocouple considering the subassembly mass flow rate and the mass of stainless steel structure and sodium. After considering the process delay, the time constant of the central bare thermocouple alone is found to be 0.26 s for TNA 000X. The thermocouples in first ring of the core are from TNA 001 to 006.

The indices X and Y refer to the two thermocouples housed inside a common thermowell for each SA. The estimated time constants are well within the limits of 4 to 8 s. The second ring thermocouples are from TNA 007 to TNA 018. The third ring thermocouple is from TNA 019 to TNA 036. In some of the thermocouples in the second and third rings, one of the redundant thermocouples (X or Y) shows higher values. The reason could be due to lesser pressure contact on one side of the gripper as shown in Fig. 3.15(a). Sensors in the third ring show higher response time which may be due to the complex thermal hydraulic mixing of peripheral sodium jets with the hotter sodium jets from the inner SA rings when the mobile core cover plate is positioned at 80 mm position. Detailed thermal hydraulic analysis indicates that increased time constant due to possible mixing is not a concern (Velusamy et al., 2010).

The reason for higher response time is explained with radiography analysis of thermocouple not touching thermowell as shown in Fig. 3.15(b). Deviation of  $\pm 2$  or 3 s in time constant from typical value (5.6 s) depends on the variation in the surface roughness

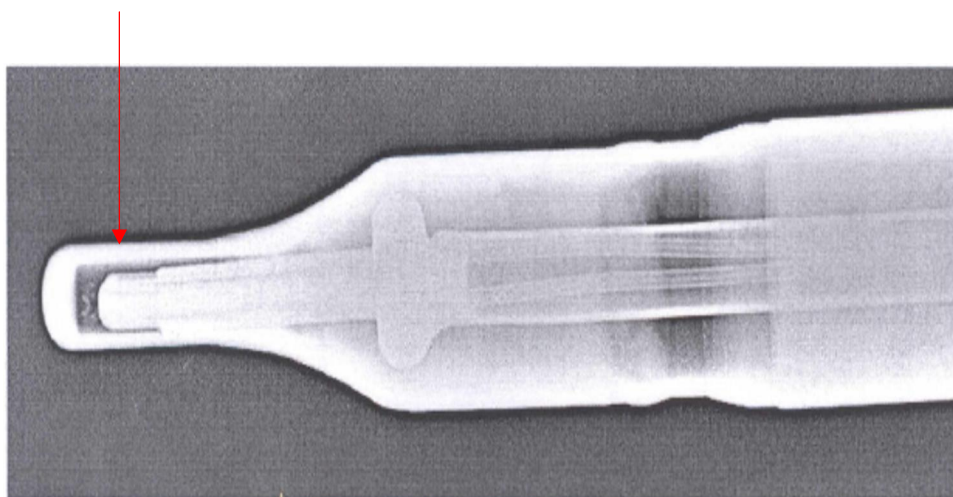
inside the thermowell which in turn modifies the contact pressure. This has been experimentally verified earlier during sodium testing. The time constant values of more than 9 s arise from an improper spring action which may be due to creep, thermal fatigue and vibration effects. Another data of 2012, set is also analysed and from the Table 2.6 it is found that the thermocouples showing higher response time in 2007 data set is also showing the same effect in 2012.

**Low pressure contact**



**a) Low pressure contact**

**Poor contact**



**(b) Poor contact**

**Fig. 3.15 Radiography examination of thermocouple**

### **3.12 CLOSURE**

Estimation of sensor response characteristics is necessary to satisfy requirements on allowable response time for nuclear power plants. The SA temperature measurements have to be performed periodically to ensure that the reactor protection limits are respected. An in-situ time constant measurement approach for FBR core temperature sensors is proposed which can utilize the ramp signal generated during LOR. The thermocouple in thermowell is modeled and the characteristic graph between contact resistance and time constant has been established. The time constant is seen to greatly depend on the contact resistance between thermocouple and the thermowell. The installed time constant of the thermocouple matches satisfactorily with the estimated time constant. The proposed technique can be implemented in FBRs.

## **CHAPTER-4**

# **DEVELOPMENT OF ULTRASONIC TECHNIQUES FOR PROTRUSION DETECTION IN CORE TOP**

## **4.1 INTRODUCTION**

As already explained in chapter-1, the core and the mechanical components which make up the primary sodium circuit are totally immersed in sodium, with the core being at ~5 m below the sodium surface. Examination of the internal structure is therefore a difficult task, visual techniques being impossible because of the opacity of the liquid metal. In the present study, ultrasound technique is explored for seeing through liquid sodium.

The use of ultrasound under sodium has been for two purposes. First is to detect any fuel subassembly projecting from its original location which may interfere with the fuel-handling operation. Another is to image and locate the top of some of the core assemblies so that estimates can be made of the bending or bowing caused by the fast neutron induced damage on the structural metal. These two purposes are called 'ranging' and 'imaging'. During fuel handling, it is essential to ensure that the region between the core top and control plug structure is not obstructed. Failure to do so could result in components breaking or at the worst case, jamming. In the UK Prototype Fast Reactor, mechanical arms sweep the core to ensure that it is clear. In the French fast reactor a simple high frequency sonar like device performs the same task (Lions, 1974). Sweep arm devices have also been considered for German reactors. The Japanese have examined the use of ultrasonic viewing systems for improving fuel transfer efficiency (Usegi, 1980).

Core distortion is caused mainly by a phenomenon known as neutron-induced void. When components are irradiated in fast reactors, fast neutrons displace atoms in the structural metal, producing voids and causing the structure to expand. Uneven neutron flux produces uneven growth and bending. The problem is severe in the fuel wrappers in the core which tend to bow away from the core centre (Bishop, 1981). Un inhibited bowing would

lead to difficulties in fuel extraction and remedial action is therefore an important part of fuel management. The role of scanner is also to image and locate the heads of some of the core subassemblies so that estimates of bow could be made. In FFTF prototype reactor a device to image the core top was developed. Trials in sodium facility of FFTF have been reported (Day, 1974). Ultrasonic rigid under sodium viewer was also loaded into the PFR. Its main purpose is to assist in the assessment of core component distortion. The technique used in the Indian Prototype Fast Breeder Reactor for bow measurement is discussed by Swaminathan, (2012). The choice of ultrasonic transducer is PZT (lead zirconate titanate) and is encapsulated in Nickel casing (Bishop,1980 and Swaminathan 1990 ).

In the present study, two methods are envisaged for finding the presence of an object in the gap between subassembly head and thermowell sleeves. Figure 4.1 shows the schematic of gap between bottom of the thermowell sleeves mounted in lattice plate and top of the subassembly, known as above core plenum. Receiving the echo directly from the projected object is called direct imaging and other one is indirect imaging using shadowing effect of protruded object on peripheral subassemblies.

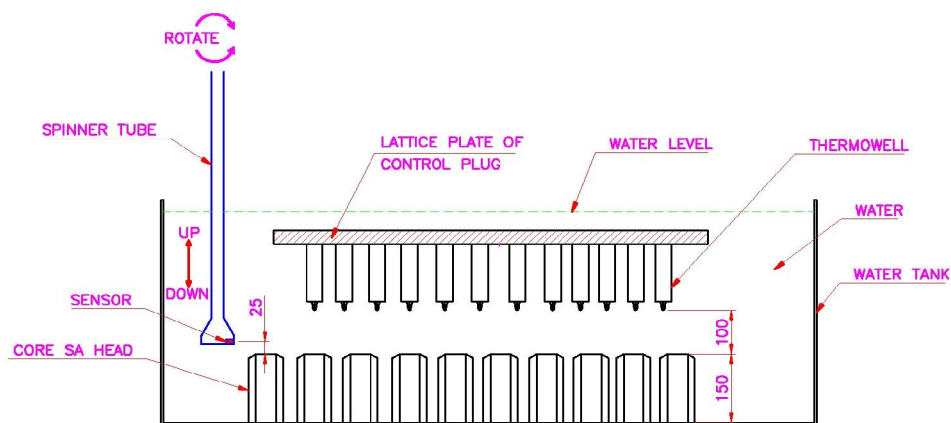


**Fig. 4.1 Schematic of above core plenum (100 mm gap)**

#### **4.1 .1 Principles of Ultrasonic Techniques**

When sound waves travel through sodium or any other medium they are reflected and refracted by targets placed in their path. This occurs whenever the dimension of the target is large compared with the wavelength of sound, and the acoustic impedance of the target is significantly different from that of sodium. This principle is applicable for most reactor targets. The acoustic impedance mismatch between sodium and stainless steel results in about 83% of incident sound energy being reflected. When considering the choice of operating frequency, it is a compromise between resolution and attenuation. High frequencies are required for good resolution but attenuation increases as square of frequency. In ranging purposes, 1 MHz frequency is selected where attenuation is sufficiently low to allow transmission through several metres in sodium. Ultrasonic technique works on pulse echo principle. In this a single transducer acts both as a transmitter and receiver of sound. Good resolution is achieved by limiting the spread of sound, i.e. by ensuring that the ratio of transducer diameter to wavelength is large and the pulses are of short duration.

#### **4.2 CONCEPT OF DETECTION METHOD**

The core in the case of PFBR consists of 1758 subassemblies (Fig. 4.2). Out of these, about 40% of the subassemblies that are located in the centre are hexagonal in shape. The remaining 60% of the subassemblies that are positioned in the periphery of the core are cylindrical in shape. These cylindrical shielding subassemblies are permanent in the reactor, while the hexagonal subassemblies are frequently changed. There are 9 rows of shielding subassemblies. The last row of shielding subassemblies is projected by 100 mm above all the other subassemblies. These subassemblies are denoted as SSA. From the shielding subassemblies, echo will be obtained as shown in the first A-scan. If any reactor components or fuel subassemblies are protruded by a differential growth of 45 mm from the normal subassembly top, as shown in the Fig. 4.3, the echo received from SSA vanishes due to the

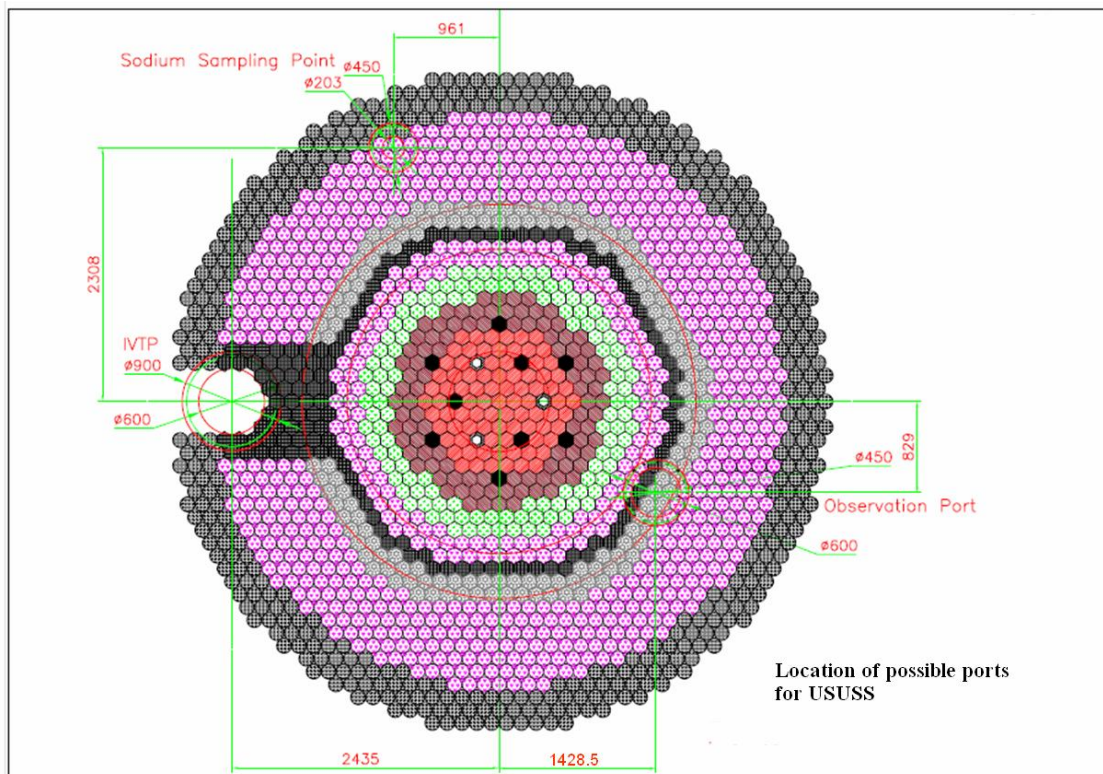


**Fig. 4.2 PFBR core (Chetal et al., 2006)**

protrusion. If the object is favorably oriented, the echo is received from the object, as well as there will be decrease in echo amplitude from the SSA. From this, location of the protruded object can be directly inferred. This is referred as direct imaging technique. This is demonstrated in second B-scan. If the protrusion is not favorably oriented then, there will not be any echo received from the object. But, at the same time, there will be a reduction in echo amplitude received from the SSA. By detecting the decrease in signal strength from SSA, the protrusion can be detected. This method of protrusion detection is referred as indirect imaging technique.

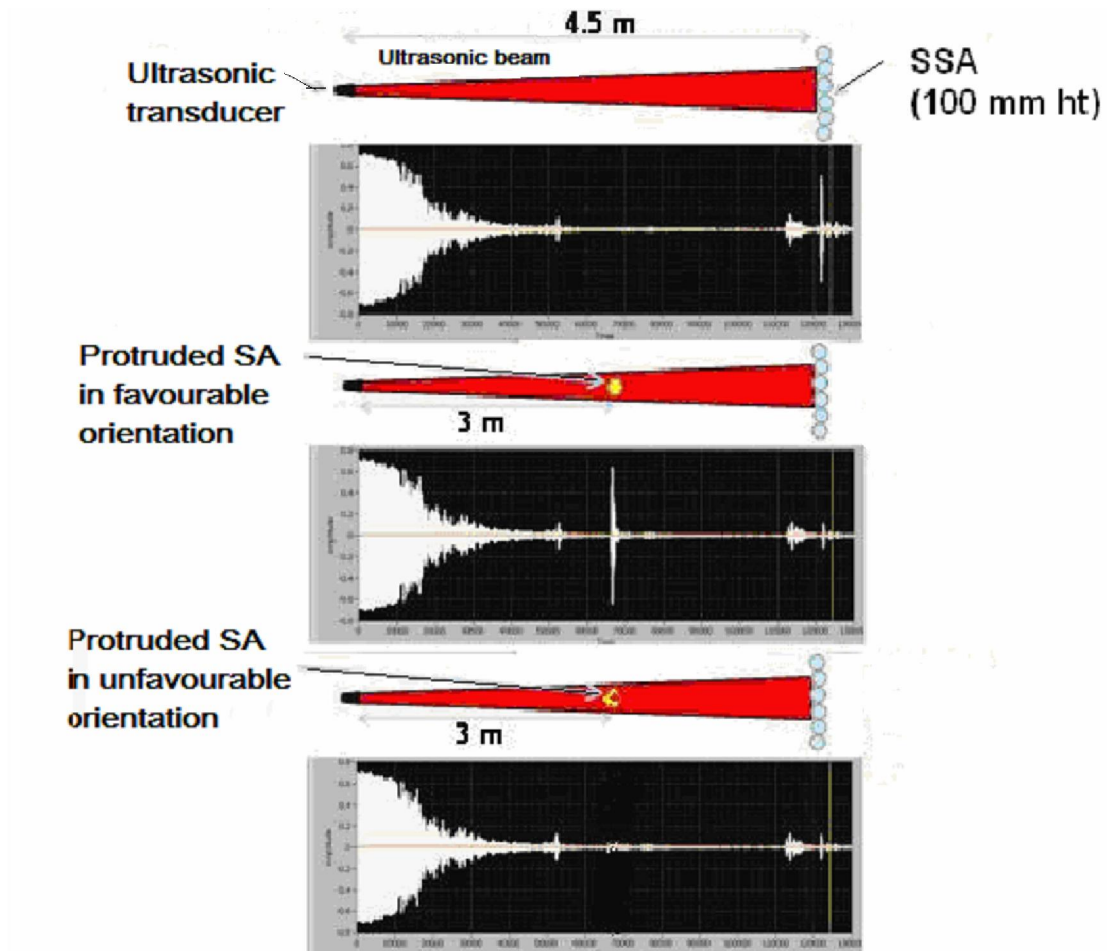


**Fig. 4.3 Principle of protrusion detection**

#### **4.3. ULTRASONIC IMAGING USING DIRECT IMAGING TECHNIQUE**

For example, in the case of PFBR (Chetal et al., 2006), there are two types of absorber rods, namely Control and Safety Rods (CSR) and Diverse Safety Rods (DSR) which are part of reactor core. In the current generation fast reactors, two types of absorber rods are used. One set of primary rods are used for power regulation and shut down while the other set of secondary rods are used only for reactor shut down. Provision of two sets of absorber rods enhances the reliability of the shut down system. The respective drive mechanisms are Control and Safety Rod Drive Mechanism (CSRDM) and Diverse Safety Rod Drive Mechanism (DSRDM) housed in the upper core structure known as control plug (see, Fig. 1.2). In the reactor, nine CSRs gripped by the respective CSRDM are used for control as

well as shutdown of the reactor. Diverse Safety Rods (DSRs) are used only for reactor shut down. DSR is attached to DSRDM. During fuel handling operation, CSRDM and DSRDM are lifted above the bottom of control plug so that there is a clear 100 mm gap in the plenum and the plug rotation can be performed safely. However, in case of any fault, CSR / DSR is not detached from CSRDM / DSRDM or if it is not lifted above the bottom of control plug, then it will hinder the plug rotation. Hence, it is necessary to detect and locate the projected object, if any before rotation of plug during fuel handling operation. The absorber rod drive mechanisms are located at fixed distance and hence gating is provided based on their location and image is constructed.

#### **4.3.1 Simulation of Projected Component in Reactor**

During reactor operating condition, gripper of CSRDM holds the head of CSR. During fuel handling operation, the CSRDM is positioned far away from the subassembly head after detaching the CSR into the core. In case of the condition in which, CSR is not detached from the CSRDM or the latter is not lifted to safe position, then it will project into the core cover plenum as shown in Fig. 4.4a. During reactor operating condition, an electromagnet of DSRDM holds the mobile DSR. In the case of reactor shutdown condition, the DSR is dropped inside the active core and DSRDM is taken out of the above core plenum. If DSRDM is not withdrawn properly, then it will be within the above core plenum as shown in Fig. 4.4b. The DSR will be within the subassembly and it will not come out along with the mechanism. Hence DSR simulation is not required. The projected components which need simulation are CSRDM gripper, DSRDM electromagnet and CSR. The portion of CSRDM gripper and DSRDM electromagnet within ~ 600 mm height can appear in the above core plenum as it moves into the SA for a distance of ~ 500 mm in addition to the 100 mm above core plenum. In order to simulate this condition in the water tank, the height of the cylindrical object is reduced to obtain overall height of ~ 230 mm by keeping the complex shapes of

same size, which is suitable to carryout experiments in the water tank. Prior to sodium testing, water testing is required, to validate the experiment as it has almost same acoustic properties as that of sodium and also handling the objects in water is easy. As the projected object has different shapes at different elevations, support rods with manual lifting arrangement are used to move the object up and down to get the image from different profiles within the 100 mm gap.

**Reactor Operating Condition**

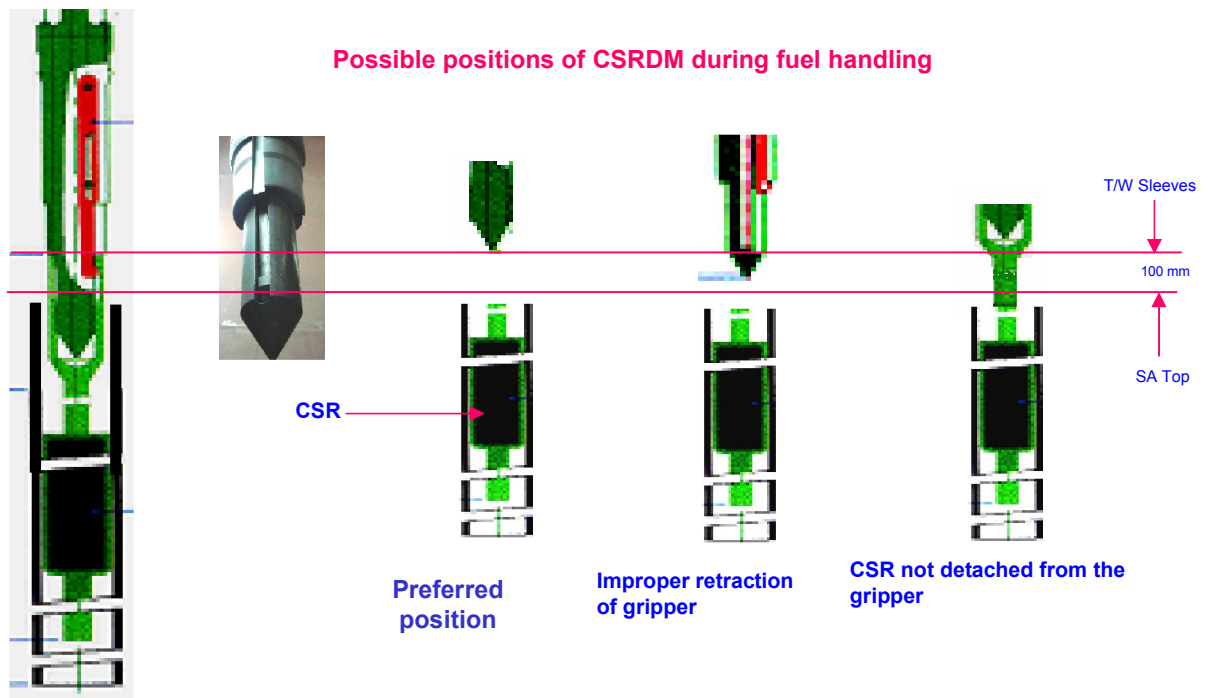


**Fig. 4.4a Portion of CSR in 100 mm plenum**

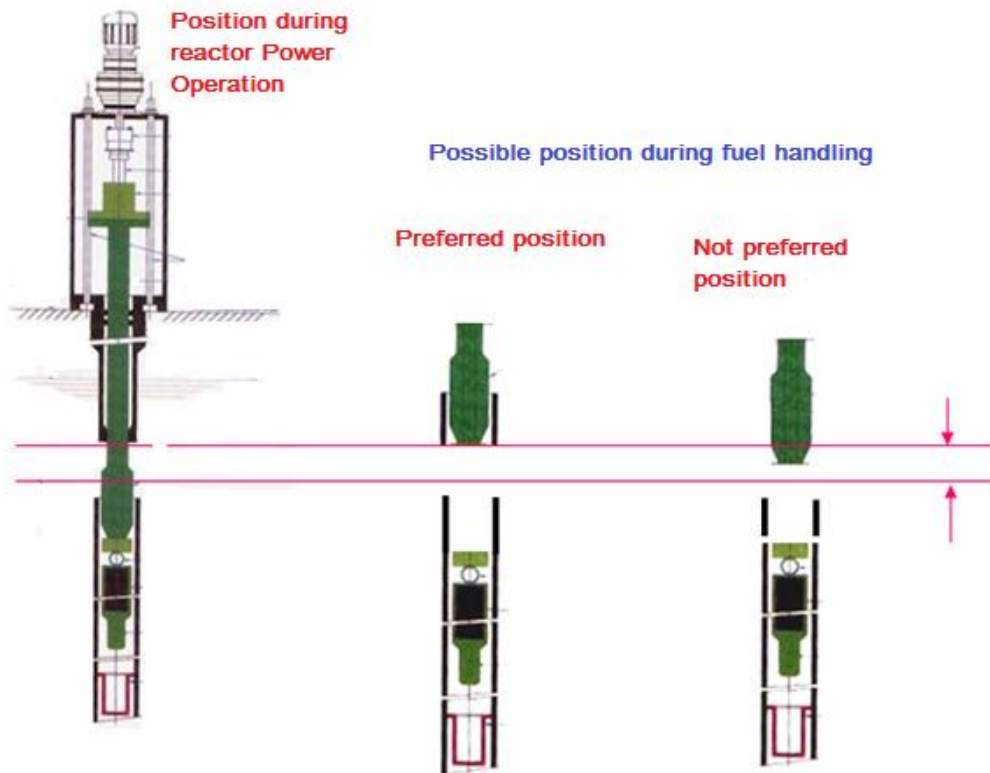


Fig. 4.4b Portion of DSRDM through 100 mm above -Core Plenum

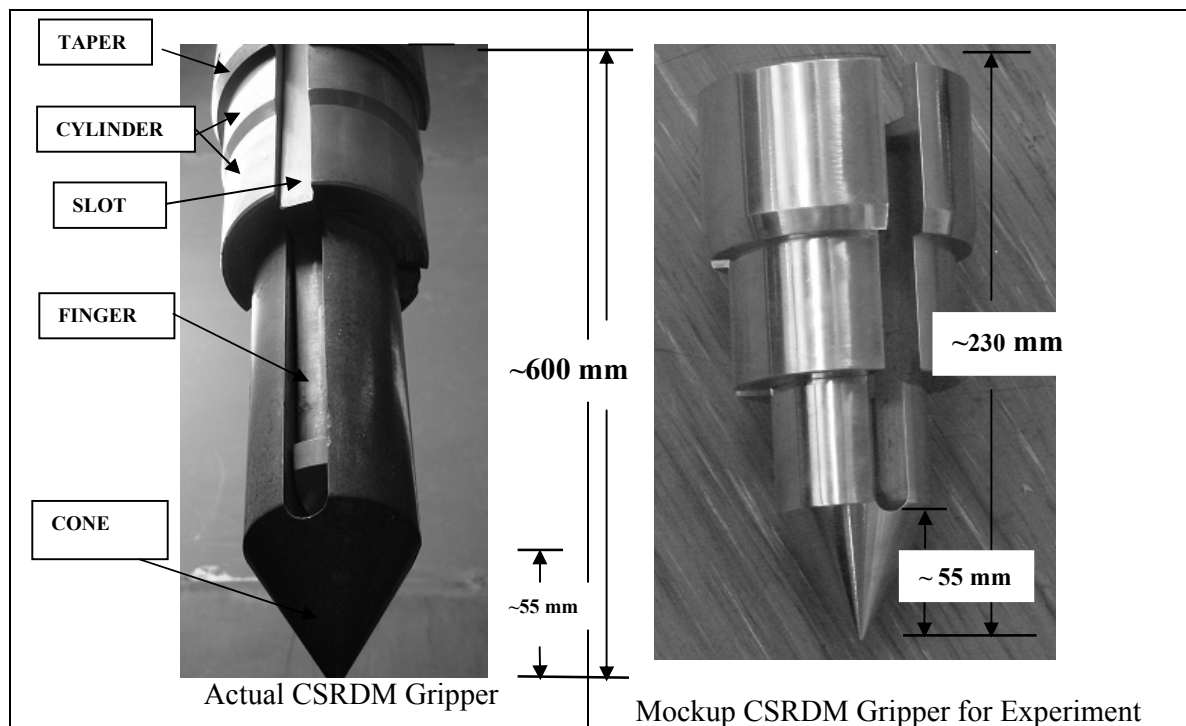
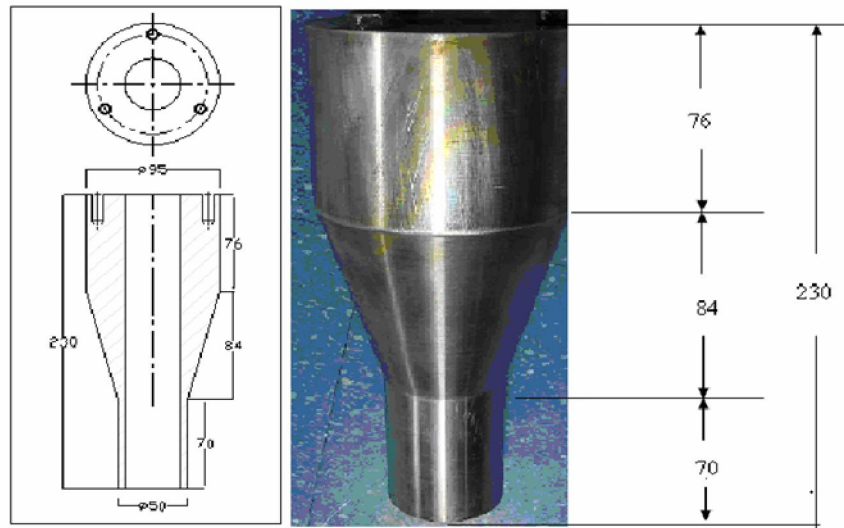
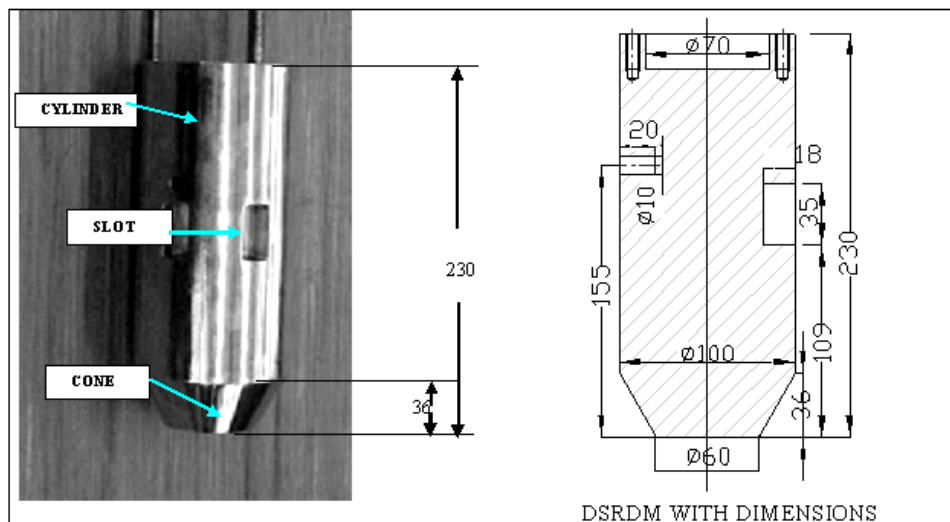


Fig. 4.5 Actual and Mockup CSRDM gripper with important dimensions

In the case of CSRDM gripper, the complex shapes are cone, cylinder, slot and taper portions. The actual size of CSRDM gripper and the mock up used for simulation are shown in Fig. 4.5. The CSR head has three different shapes, two cylindrical and a conical shape. The shapes in DSRDM are rectangular slot, conical portion and cylindrical surface. Geometric details of experimental CSR and DSRDM are shown in Figs. 4.6 and 4.7 respectively.



**Fig. 4.6 Experimented CSR**



**Fig. 4.7 Experimented electromagnet of DSRDM with support rod**

### 4.3.2. Orientation of CSRDM and DSRDM

Deployment of the scanner requires two openings in the top shield (Fig. 1.2). In the case of PFBR, the In-Vessel Transfer position (IVTP) access port and Observation port are used for this purpose as depicted in Fig. 4.8. Locations of CSRDM and DSRDM and distance from the transducer are depicted in this figure.

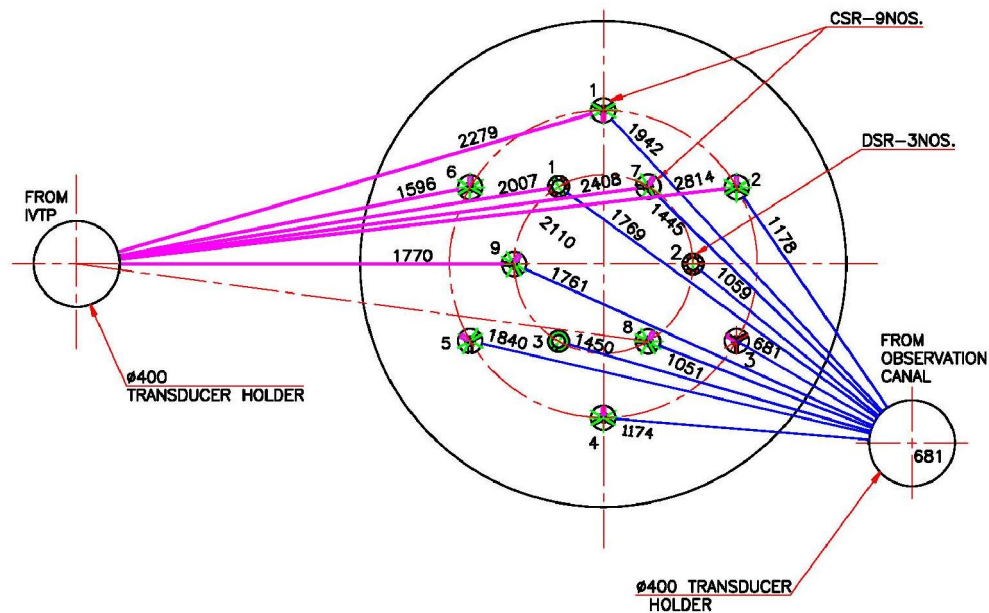


**Fig. 4.8 Orientation of CSRDM and DSRDM from IVTP access port and Observation port**

The straight line shows the direct view of both CSRDM and DSRDM from IVTP access port and Observation port. The maximum distance for CSRDM from IVTP access port is 2814 mm. The same is simulated in the water experiments.

### 4.3.3 Experimental Setup

For construction of ultrasonic images the ultrasonic transducer should be scanned systematically over the object known as ‘scanning’. The experimental set up consists of mechanical scanner, ultrasonic transducer, ultrasonic equipment and the Personal Computer (PC) based automation system.

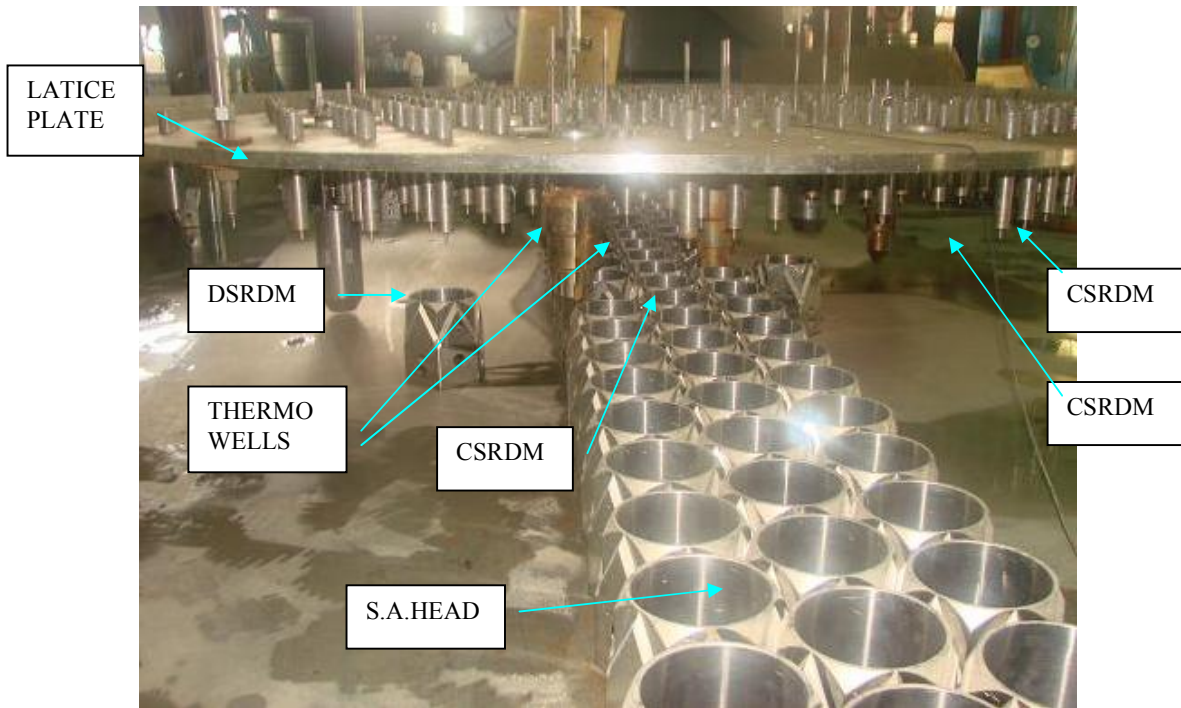


**Fig. 4.9 Experimental setup**

- **Mechanical Setup**

To carry out the ultrasonic imaging experiments, a set up has been erected in conjunction with the 5 m water tank as shown in Fig. 4.9. The setup consists of ultrasonic scanner fitted with 1 MHz ultrasonic transducer, located at one extreme end of water tank. The mockup scanner consists of 6 m long 33 mm diameter stainless steel tube called the spinner located inside a 90mm diameter guide tube. The spinner tube is inserted through the guide tube which carries transducer holder at its bottom end. The guide tube serves to maintain the lengthy spinner tube vertical and without wobbling during it's up /down and spinning movements. An ultrasonic transducer is mounted inside housing at the bottom of the spinner tube with its active face looking sideways. The liquid sodium proof transducer consists of piezoelectric crystal soldered on to the nickel casing to operate at high temperature. The spinner tube is allowed to move vertically by 300 mm and allowed to rotate about its axis. The spinner tube is attached with 2 stepper motors one for rotary movement and other for axial movement. The lattice plate of 2.25 m diameter is fixed using

tie rods at the centre of the tank. The lattice plate consists of thermowell sleeves and has the provision to locate the CSRDM and DSRDM. The simulated CSRDM gripper is fixed on the holder provided in the lattice plate (6 CSRDM + 3 DSRDM). The height of the water pool is 500 mm. The tank bottom is leveled by mounting thick S.S. plate. The water tank has the facility to fill and drain the water. The subassembly heads of 150 mm height have been fabricated and mounted in the tank. The lattice plate height is adjusted such that the gap between the bottom of the thermowell sleeves and subassembly top is maintained as 100 mm. The transducer centre is placed at 25 mm above the subassembly top and the remaining 75 mm is scanned by the ultrasonic transducer. The 25 mm length is known as the dead zone which is due to the dimension of the transducer.

- **PC based automation system**

A PC based automatic ultrasonic scanning system is developed to carry out ultrasonic experiments in water. Fig.3.10 shows the schematic of the PC based automation system. The system consists of mechanical scanner, liquid-sodium proof transducer, stepper motor and drive system, Ultrasonic equipment, Industrial PC with digitizer card and the software for acquisition of ultrasonic data and C scan plotting.

- ***Ultrasonic scanner***

The scanner consists of 6 m long tube about 90 mm diameter called guide tube and smaller diameter tube called spinner tube which is kept inserted through the guide tube carrying transducer holder at its bottom end. The spinner tube is allowed to move vertically 300mm and allowed to rotate about its axis. The spinner tube is attached with 2 stepper motors

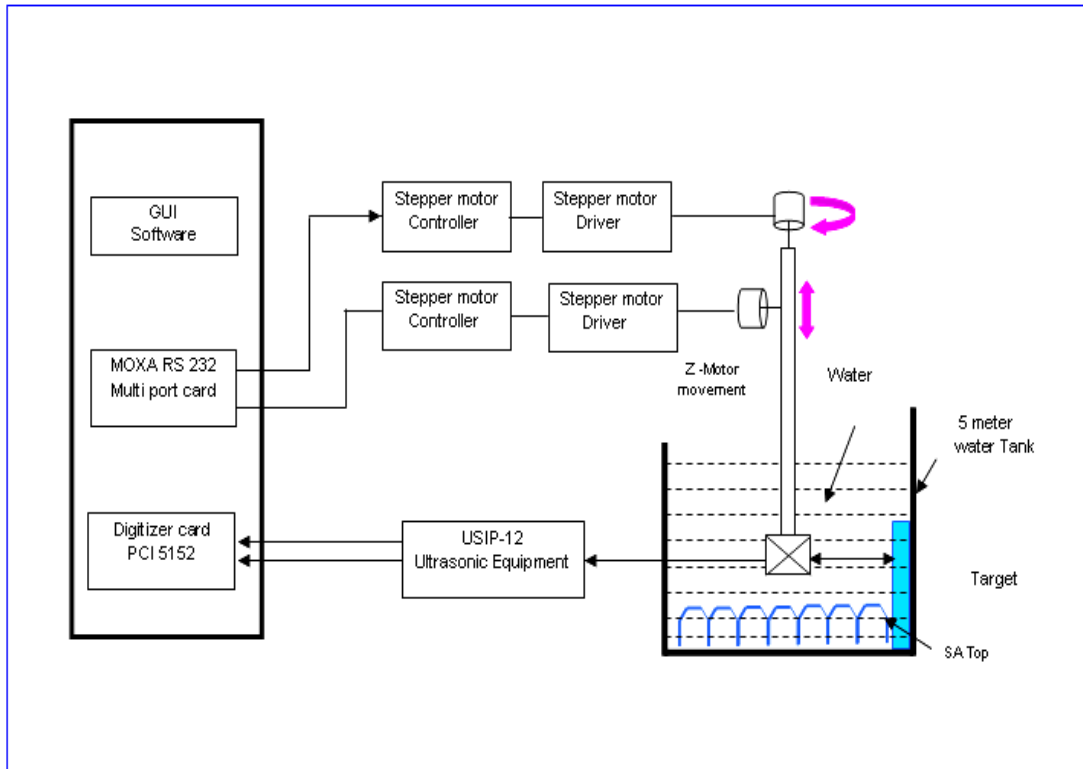


**Fig. 4.10 Scheme of Automation system**

- ***Ultrasonic Transducer***

Ultrasonic experiments are carried out in water for ranging purposes. Therefore 1 MHz PZT plain-A crystal having curie temperature of 380°C is used for transducer design. The transducer is assembled in a nickel casing which is having good wettability at reactor shut down temperature of 180°C. The crystal is soldered to the diaphragm inner surface using high temperature solder alloy having melting point of 220°C. For sodium application, 3 mm dia. Mineral insulated cable with copper conductor along with contact plate serves the purpose of carrying electrical pulses to the crystal which is insulated from the body using alumina ceramic. For water application, co-axial cable is used. The transducer is used as transmitter as well as receiver.

- ***Ultrasonic test instrument***

The ultrasonic test instrument is an important instrument in the PC-based automation system. The function of the instrument is to supply high voltage pulse in the form of ‘spike’/tone burst to the transducer which is then allowed to vibrate at its natural frequency of 1 MHz. This ultrasonic echo travels back to the transducer which converts it back to a voltage pulse. The instrument has provision to give RF output. This is interfaced with the high speed digitizer card mounted inside the industrial PC. USB based external digitizer card is adopted for reliable long term application. Therefore the acquisition scheme was modified to acquire RF signal and view the distance of 5 m by suitably selecting 100 Hz pulse repetition rate. Analog amplification of the radio frequency ultrasonic signal is straight forward (Da Silva 2005; Pro-Wave 2005). The RF signal is digitized to permit real-time or post acquisition signal processing. Digitization permits signal averaging, frequency analysis, implementation of software filter and special algorithms to improve signal to noise ratio (Karasawa, 2000).

- ***Stepper motor and its drive system***

A high performance micro stepping driver and a stepping motor (Alpha Step) with built-in-rotor-position sensor is used in the set up. The speed and the amount of rotation are constantly monitored during the operation, so that when an overload is about to cause the motor to misstep, any deload in response is corrected and operation continues at maximum torque. In addition to the four-gear types ideal for low-speed high torque operation, a model equipped with an electromagnetic brake is used. This is suitable for holding the load in position during Z-axis or  $\Theta$ - axis movement. The stepper motor is connected to a separate a DC power supply of 24V DC through a shielded cable separately connected to the electromagnetic brake.

The stepper motor drive system consists of a translator circuit (Photo Transistor) that receives a signal that includes the number of steps and direction. The translator circuit sends four individual control signals to the switch set circuit and the switch set circuit sends power signals to each of the two phases (windings) in the stepper motor. The signal for the number of steps is a series of square wave pulses (one for each step) which is used to move the rotor. The signal for the direction is constant-voltage signal that is either positive or negative. The translator receives the signal from a Programmable Logic Controller (PLC). The PLC sends a command signal that consists of the number of steps the motor should run and the direction signal indicates the direction. The LED in the PLC module can detect the steps signal.

There are 2-inputs connected to the driver, viz., Direction and step active signal

1. When the DIR input is ON, a rise of the “PLS input” from OFF to ON will rotate the motor one step in CW direction.

2. When the DIR input is OFF, a rise of the “PLS input” from ON to OFF will rotate the motor one step in CCW direction.

For carrying out the experiment, the scanner automated with 2 geared stepper motors with micro stepping drive for Z and Theta movements are used. The USIP-12 equipment/Ritec pulser receiver with spike/tone burst excitation is used in pulse echo mode. The in house developed ultrasonic transducer of 1 MHz frequency is connected to this equipment. The RF signal output from USIP-12/Ritec is interfaced to the PCI 5152 digitizer card with the following specification

- 300 MHz bandwidth
- 2 GS/s maximum sampling rate
- 2 simultaneously sampled channels
- onboard memory - 64 MB/ch
- 10 V input range

The digitizer card is located inside the Industrial PC and a software has been developed in Lab view for acquiring A scan data, B scan data, C scan data, offline analysis and movement of stepper motors. For controlling the stepper motor, controllers and drives are required. The controller is controlled by sending commands through RS232C communication port from PC. The MOXA make RS 232 multiport communication card is used in PC which provides additional communication ports for controlling the two stepper motors.

- ***Software Architecture***

The main user interface consists of buttons, from which one can navigate to different screens such as configuration panel, A-scan, B-scan, C-scan, offline analysis and exit. The Main panel consists of two main loops, viz., upper loop to handle the front panel buttons and lower loop to carry out the operation such as motor movement, then acquisition of ultrasonic data, finding out transit time based on gate settings, plotting of images based on menu driven commands from A-scan, B-scan, C-scan and offline analysis.

- ***Commissioning of automation system***

For carrying out water experiments, the scanner having 2 geared stepper motor with micro-stepping drive for Z and theta movement is successfully interfaced to the PC. The ultrasonic equipment with spike excitation is used in pulse echo mode. The in house developed ultrasonic transducer is connected to the equipment. The RF signal is interfaced to the digitizer board located in industrial PC. A software has been developed for acquiring A scan, B-Scan and C-Scan data. Software filters are provided to acquire noise-free signal. For constructing the images C-scan facility is used. Once the amplitude crosses the threshold limit, point is plotted on the screen corresponding to the motor movement.

The color of the point is based on the transit time data thereby constructing the pseudo 3D images.

#### 4.3.4 Details of Experiments

Different experiments have been conducted by systematically moving the ultrasonic transducer (center beam) from 25 mm height (above the normal SA top surface) to 100 mm height in steps of 1 mm in the upward direction and  $0.2^\circ$  steps in the  $\theta$  direction. Based on different orientation and shapes of the components, criteria for the different case studies are selected.

- **Case – 1**

Fig.4.11a shows the plotted image of CSRDM and DSRDM with minimum amplitude threshold of 0.1V which is just above the noise level. It shows top view and side view of three CSRDMs and two DSRDMs. The different shapes and profiles of CSRDMs and DSRDMs have been simulated in the first case study.

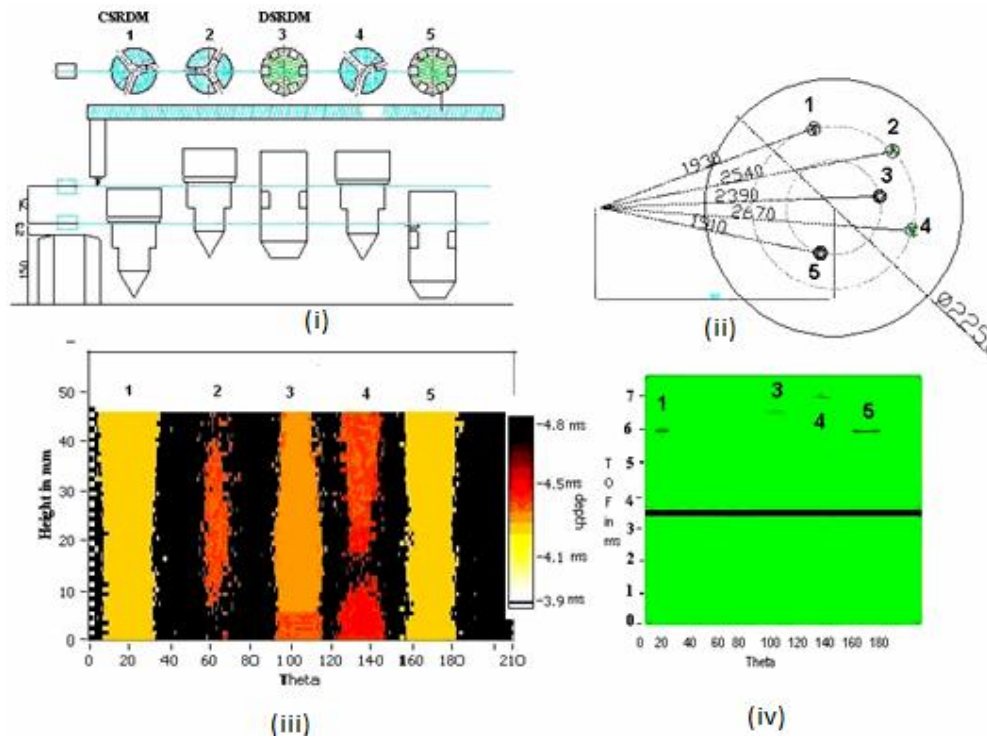


**Fig. 4.11a Case-1 objects and Ultrasonic image with threshold of 0.1V at 0 mm elevation**

**(i) Side view of objects (ii) Top view of objects (iii) C-scan image (iv) B-scan image**

In CSRDM, taper, and stepped cylindrical portion with and without slot and in DSRDM, cylindrical portion with and without slot have been experimented. The shapes of the objects and their side and top views are tabulated in Table - 4.1.

**Table-4.1 Shape of objects in case-1**

Object No.	Name of the object	Shape of the object in Side view	Shape of the object in Top view
1	CSRDM	Tapered and cylindrical portion	Without slot
2	CSRDM	Cylindrical portion	With slot
3	DSRDM	Cylindrical portion	With rectangular slot
4	CSRDM	Two cylindrical portion of varying dimension	Without slot
5	DSRDM	Cylindrical portion	Without rectangular slot

The image is constructed with different colors for different depths. The image is very distinct with good echo strength irrespective of the tapered portion in Object No.1 which is CSRDM. Because the slot is in direct view to ultrasonic transducer, echo is not of sufficient strength and hence the image was not distinct in the second object. The third object is DSRDM cylindrical portion with rectangular slot in 100 mm plenum. The image is clear but not broader when compared with object No.5 due to the presence of slot in the cylindrical portion. The fourth object is CSRDM with slot slightly away from the direct view of transducer and two cylindrical surfaces of varying dimensions in 100 mm plenum. The variation in transit time due to difference in dimensions of the cylindrical portion is observed in the image by two different colours. In the case of fifth object, the echo strength is very good and broader image is obtained from the cylindrical portion of DSRDM.

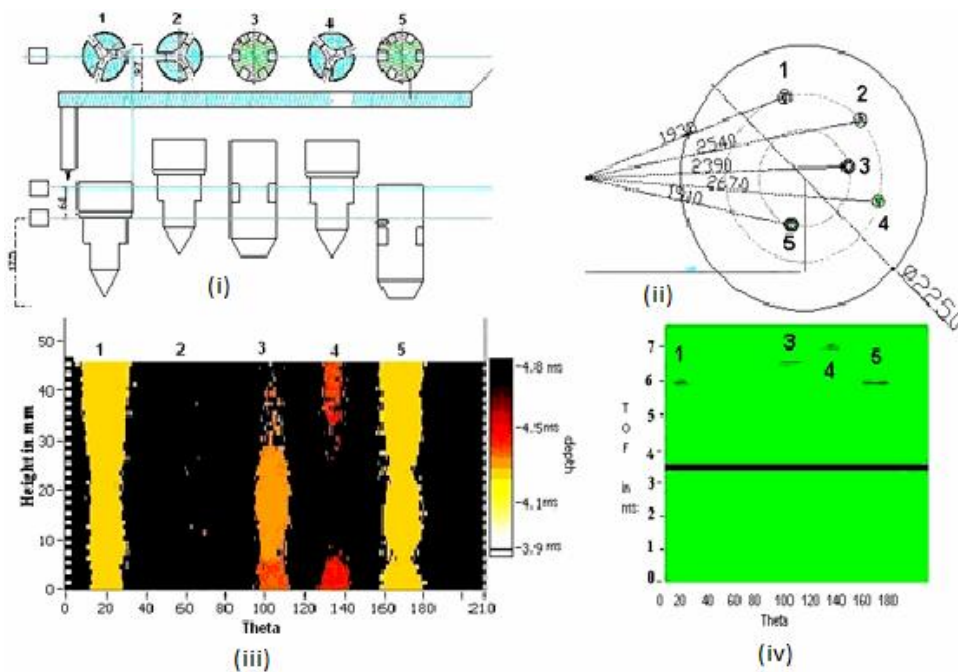


**Fig. 4.11b Case-1 objects and Ultrasonic image with threshold of 0.15V at 0 mm elevation : (i) Side view of objects (ii) Top view of objects (iii) C-scan image (iv) B-scan image**

The same data is analysed by varying the amplitude thresholding. Figure 4.11b shows the same image plotted with amplitude thresholding of 0.15V. The difference in images of the DSRDM objects 3 and 5 is clearly observed. The signal strength from the slot is less compared with cylindrical surface without rectangular slot. The B-scan image at 0 mm elevation gives the depth information of the objects. The objects 1 and 5 give better echo strength compared with 3 and 4 which are represented in darker lines in B-scan. Due to the sudden change in the dimension, discontinuity is observed in the image of object no.4. To confirm the discontinuity in image due to sudden dimensional change, experiment is repeated. Fig.4.11c shows the repeated trials of CSRDM object and its image.

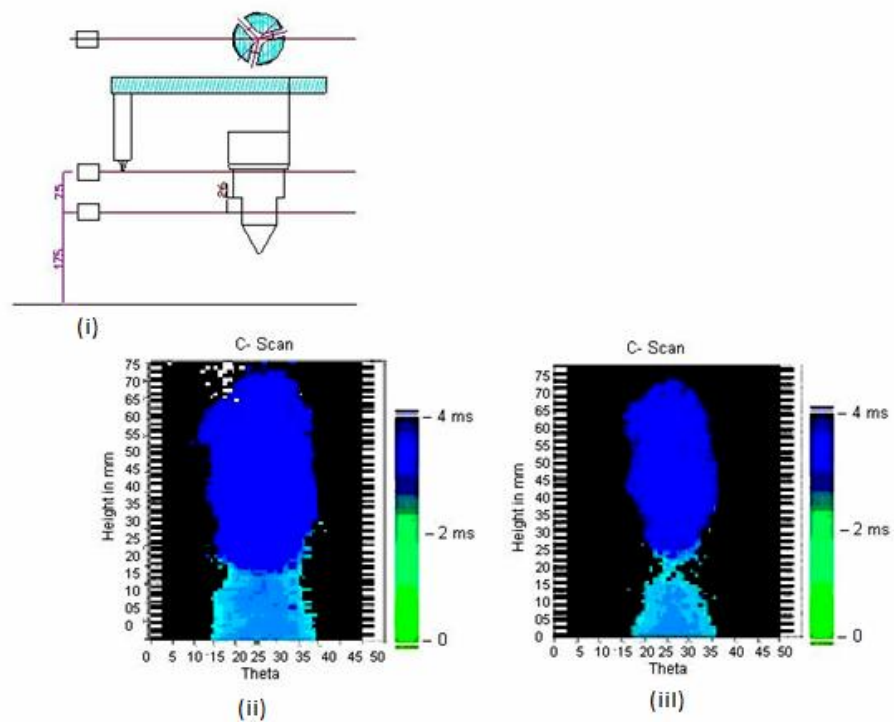


**Fig. 4.11c Case-1 CSRDM object and its ultrasonic image**  
**(i) Side view of objects (ii) C-scan image of CSRDM (iii) C-scan image with higher amplitude thresholding**

Difference in transit time is observed as two different colors in the image. The discontinuity is observed in the image with higher amplitude thresholding.

- **Case – 2**

In case -2, the ultrasonic imaging of conical portions of CSRDM and DSRDM are aimed at. The first and fourth objects are used as reference. In the case of second object (CSRDM), conical portion is in the 100 mm plenum, hence, reflected ultrasonic energy does not come back to the ultrasonic transducer and no echo is observed from the object. In the case of third object (DSRDM) also, conical portion is in the 100 mm plenum, hence image is not obtained. Fig. 4.12 shows ultrasonic imaging of conical portions of CSRDM/DSRDM.

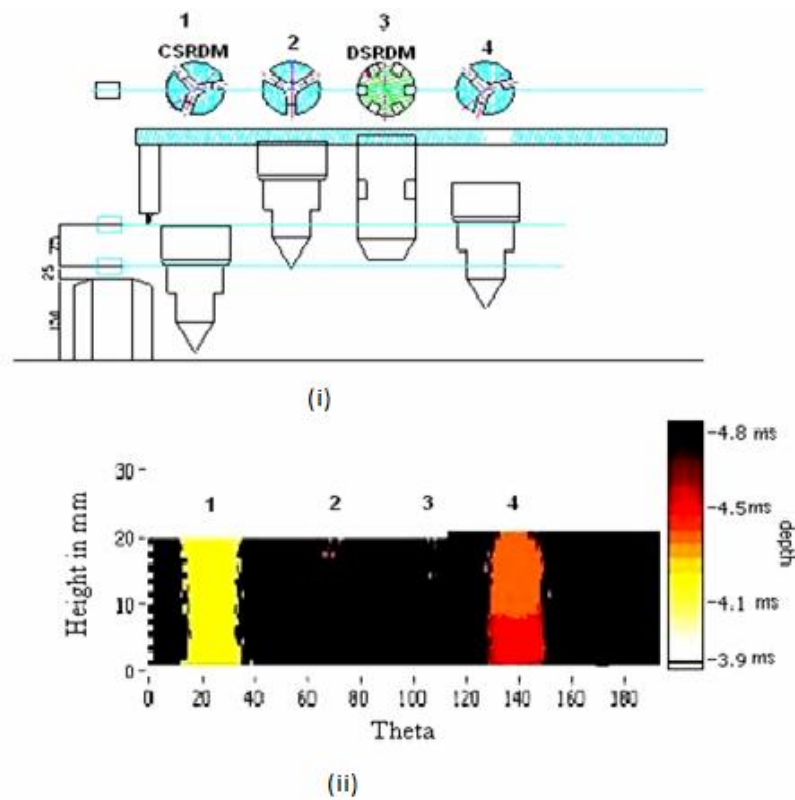


**Fig. 4.12 Case-2 Ultrasonic image of conical portions of CSRDM/DSRDM**

**(i) Side view of objects (ii) C-scan image of objects**

- **Case – 3**

Figure 4.13 shows the object and its ultrasonic image. The first object is CSRDM in which the slot is in direct view to ultrasonic transducer with cone and cylindrical surfaces in

side view. A feeble echo is received from the cylindrical portion above the conical portion. But no echo is received from the conical portion. In the case of second object (DSRDM) with rectangular slot, the image is plotted in full strength but with a slight change in echo strength near the rectangular slot portion.

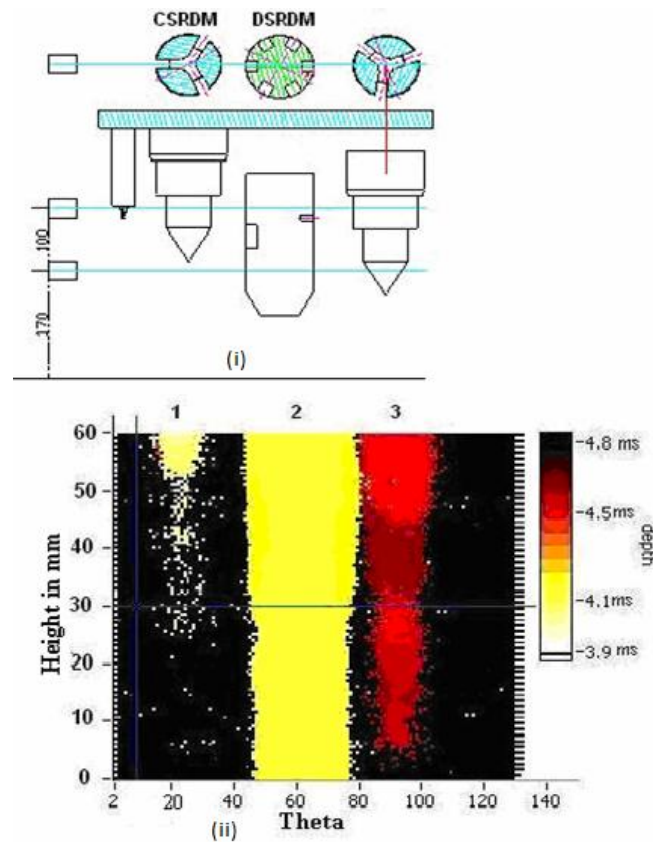


**Fig. 4.13 Case-3 Objects and its ultrasonic image**

**(i) Side view of objects (ii) C-scan image**

The third object is CSRDM with slot at slight deviation from the direct path and small conical portion with cylindrical surface in the above core plenum, No echo is received from conical portion and good image is obtained from the cylindrical portion.

- **Case – 4**

Figure 4.14 shows the ultrasonic image of CSR object. In the first orientation, 16 mm cylindrical portion above the subassembly top contributes to good image and due to

beam divergence, the image is constructed for longer elevation. Also, at 75 mm height again, image is obtained from the starting point of cylindrical portion.

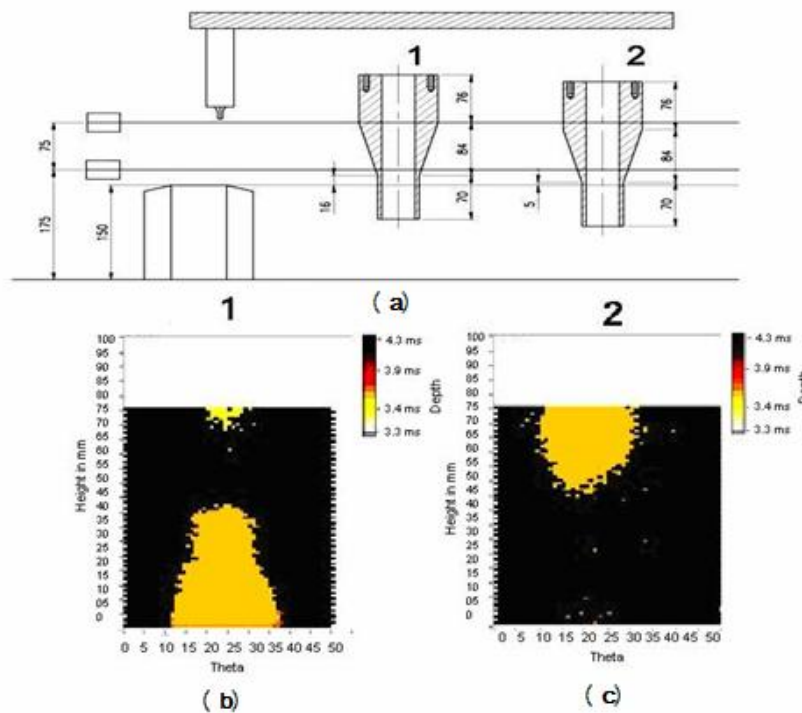


**Fig. 4.14 Case- 4 Ultrasonic image of CSR at two different orientations**

**(a) Side view of objects (b) C-scan image of object-1 (c) C-scan image of object-2**

The echo started appearing from the top cylindrical portion also. In the second orientation, 5 mm cylindrical portion 84 mm conical portion and 11 mm cylindrical portion are viewed through above core plenum. No image is obtained from 5 mm cylindrical portion. But, 11 mm top cylindrical portion gives raise to sufficient echo. Due to beam divergence, at lower elevation onwards image is obtained.

#### **4.3.5 DISCUSSION**

From case-1, it is concluded that, if the CSRDM slot is not in direct view and cylindrical portion is in above core plenum, broad and distinct image can be obtained. The small tapered portion in between two cylindrical surfaces is not having any impact due to

beam divergence effect. If the slot is in direct view and cylindrical surface is with in the plenum, only feeble echo is received and the image is not distinct. For two different diameters of cylindrical portions with step change in CSRDM, different transit times are observed and are represented in two different colors. Due to sudden change in cylindrical portion, a small discontinuity is observed in the image for higher amplitude thresholding. In the case of DSRDM, the cylindrical portion without slot gives rise to broad and distinct image compared to the cylindrical portion with slot. However in both the cases, images are obtained.

From case-2, it is concluded that the conical portion of CSRDM and DSRDM at the end will not give back echo and hence image cannot be obtained. The images of the objects 1 and 2 are used as reference.

From case-3 it is concluded that if the CSRDM slot is in direct view to transducer, and also conical and cylindrical portion are in above core plenum, no echo is received from the conical portion and feeble echo is observed from the cylindrical portion. In the case of CSRDM, if the slot is in slight deviation from direct ultrasonic path, good images are obtained.

From case-4, it is concluded that the strong echo is received from the cylindrical portion of 16 mm of CSR and echo started appearing from the top cylindrical portion also. No echo is obtained from conical portion. Due to beam divergence, the image is plotted for longer distance. In the orientation-2, a strong echo is obtained from the top cylindrical portion of height 11 mm and no echo is received from the bottom cylindrical portion of 5 mm.

To summarise the result, in the case of CSRDM, the cylindrical portion gives rise to very good image provided the slot of the CSRDM is not in direct view of ultrasonic

transducer. The conical portion of DSRDM and CSRDM will not give back echo irrespective of position of the slot using direct imaging technique.

#### **4.4 ULTRASONIC IMAGING USING INDIRECT IMAGING TECHNIQUE**

In the case of PFBR, 30% of the hexagonal fuel subassemblies are oriented favorably to ultrasonic beam and remaining 70% are unfavorably oriented to ultrasonic beam. In indirect imaging technique, protrusion is detected by shadowing effect of protruded object on cylindrical peripheral shielding subassemblies (SSAs). The peripheral SSA has 100 mm extra projection above any other subassembly and located in the last row of the core. The possible protruded objects are hexagonal fuel subassembly head as shown in Fig. 4.15 and absorber rod drive mechanisms which are not geometrically favorable to ultrasonic beam in some orientation. In indirect imaging technique, there is a change in the echo pattern and reduction in amplitude received from the SSA due to the protruding object. The challenge is to analyse the data using specific methodology for protrusion detection. The ultrasonic scanner is deployed in two ports namely, In-vessel Transfer Position access port (IVTP) in large rotating plug and Observation Port.

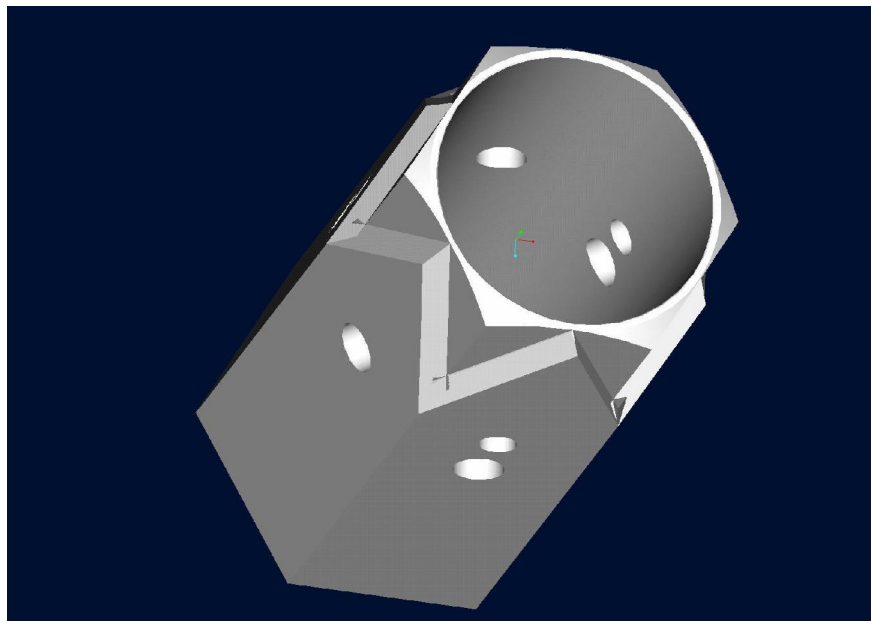


**Fig. 4.15 Fuel subassembly head**

#### 4.4.1 Simulation

The reactor core consists of different sectors. Each sector contains a group of subassembly arranged in specific patterns. These patterns are simulated in 5 m water tank and experiments were carried out using transducer having 0.6 MHz frequency to simulate the beam divergence effect equivalent to that in sodium for 1 MHz frequency. The beam spread half angle in water and sodium are given by the formula

$$\sin\theta_1 = K\lambda_1/d, \quad \sin\theta_2 = K\lambda_2/d \text{ -----(4.1)}$$

Where  $\theta_1$  ----- beam spread half angle for water

$\lambda_1$  ----- wavelength of 1 MHz frequency transducer in m

D ----- distance of the object in m

$\theta_2$  ----- beam spread half angle in sodium in deg.

From the experiment, the half beam angle for 1MHz transducer is found out to be 3° in water.

A cylindrical rod of 3 mm diameter is placed at various distances and the transducer was moved through an angle of 18 deg. and the intensity of the echo signal is plotted in Fig. 4.16.

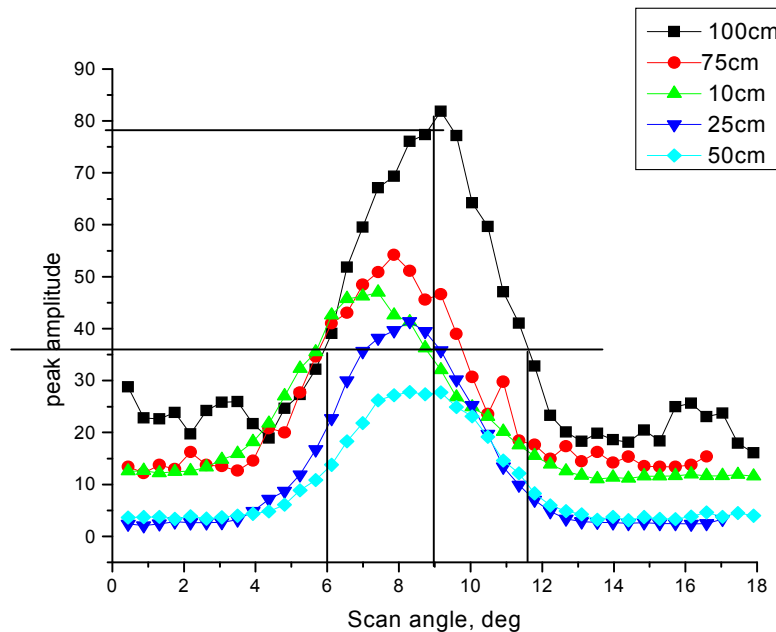


**Fig. 4.16 Determination of beam spread in water using 1 MHz transducer**

From the peak value, the angular distance for 70% of the signal drop is obtained. The half beam angle obtained from the graph is 3°.

The half beam angle for sodium can be calculated using the formula

$$\sin\theta_1 / \sin\theta_2 = \lambda_1 / \lambda_2 \text{ -----(4.2)}$$

The wave length is calculated using the formula

$$V = n \lambda \text{ -----(4.3)}$$

For water  $1500 = 1 \times 10^6 \times \lambda_1$  and for Sodium (Na)  $2500 = 1 \times 10^6 \times \lambda_2$

$$\lambda_1 = 1.5 \times 10^{-3} \text{ m}$$

$$\lambda_2 = 2.5 \times 10^{-3} \text{ m}$$

Using eq, (4.2) half beam angle in sodium is found to be

$$\theta_2 = 5^\circ$$

For the same medium, velocity of sound remains same. Therefore we have

$$\sin\theta_1 / \sin\theta_2 = f_2 / f_1 \text{ -----(4.4)}$$

The frequency required for the transducer to simulate the same beam angle in water equivalent to that of sodium is found to be

$$f = 0.6 \text{ MHz}$$

A water proof transducer with PZT crystal of 500 kHz resonant frequency has been fabricated and is excited using 0.6 MHz frequency sine wave. Experiments are carried out in water using this frequency. The two factors which vary in sodium and water are

1. Beam divergence
2. Beam attenuation

The beam divergence equivalent to that of sodium is simulated in water using 0.6 MHz frequency. The attenuation of the signal amplitude  $A$  can be described by the general law of attenuation  $A = A_0 e^{-\alpha x}$ . For two different sound paths  $x_1$  and  $x_2$  the following linearised form results:  $2 \cdot \ln(A_2/A_1) = \alpha \cdot (x_1 - x_2)$ . The attenuation coefficient ( $\alpha$ ) of the liquid is determined experimentally. Based on the attenuation coefficient, Distance Amplitude

Correction (DAC) will be suitably applied in the electronics to compensate for the attenuation loss.

#### 4.4.2 Algorithm

The signal strength from each cylindrical Blocking SA (BSA) varies due to its orientation. And also due to beam divergence effect, there will be bunch of echoes received from the BSAs. The reflections from the adjacent BSAs due to divergence effect arrive at different time of flight compared with reflections from BSA which are at direct line of sight. Therefore angle specific gating was provided and with in gating, summation algorithm was used for plotting the C-scan image. The algorithm with in gating was represented as

$$\text{Intensity of signal within the gate} = \frac{\sum_{i=1}^n |A_i|}{n} \text{-----(4.5)}$$

Where, n is the no. of samples within gate and

mod A is the amplitude of the rectified signal.

In case of protruding subassembly not being favorably oriented, scanning from one port will provide information about protrusion and to exactly locate the position, ultrasonic scanning is to be carried out from another port.

#### 4.4.3 Details of Experiments

The reactor core is shown in Fig. 4.17 along with 6 retro reflectors. The details of sector-1 to sector-5 are marked in reactor core. The peripheral subassemblies are cylindrical in shape except 6 subassemblies. The reference targets (retro) are fixed over cylindrical subassembly at 6 different places. The reference target is used to assess the inclination of the transducer in the installed condition of the scanner. The following experiments have been performed in water tank simulating the retro reflector also.

The retro reflectors are corner cube reflectors used to measure the vertical orientation of the side viewing transducers. The complete core is simulated in 5 m water tank in different sectors with 40° scan angle. The scanning experiment is carried out with 1° step angle and 1 mm vertical height. Totally 9 experiments have been carried out with the above specific algorithm. Two representative results are presented along with the above experiments, viz.,

- Effect on inclination of objects with respect to ultrasonic beam and
- Effect of random protrusion of 20 mm

**Table-4.2 Simulation of sector in clockwise direction**

<b>Sector</b>	<b>Simulation</b>
Sector 1 (Half)	Without Retro
Sector 3	Retro 1 (OP-R2)
Sector 4	Retro (IVTP-R2)
Sector 5	Retro (OP-R1)

**Table-4.3 Simulation of sector in anti-clock wise direction**

<b>Sector</b>	<b>Simulation</b>
Sector 1 (Half)	Without Retro
Sector 3	Retro 2 (IVTP-R3)
Sector 4	Without Retro
Sector 5	Retro(OP-R3)

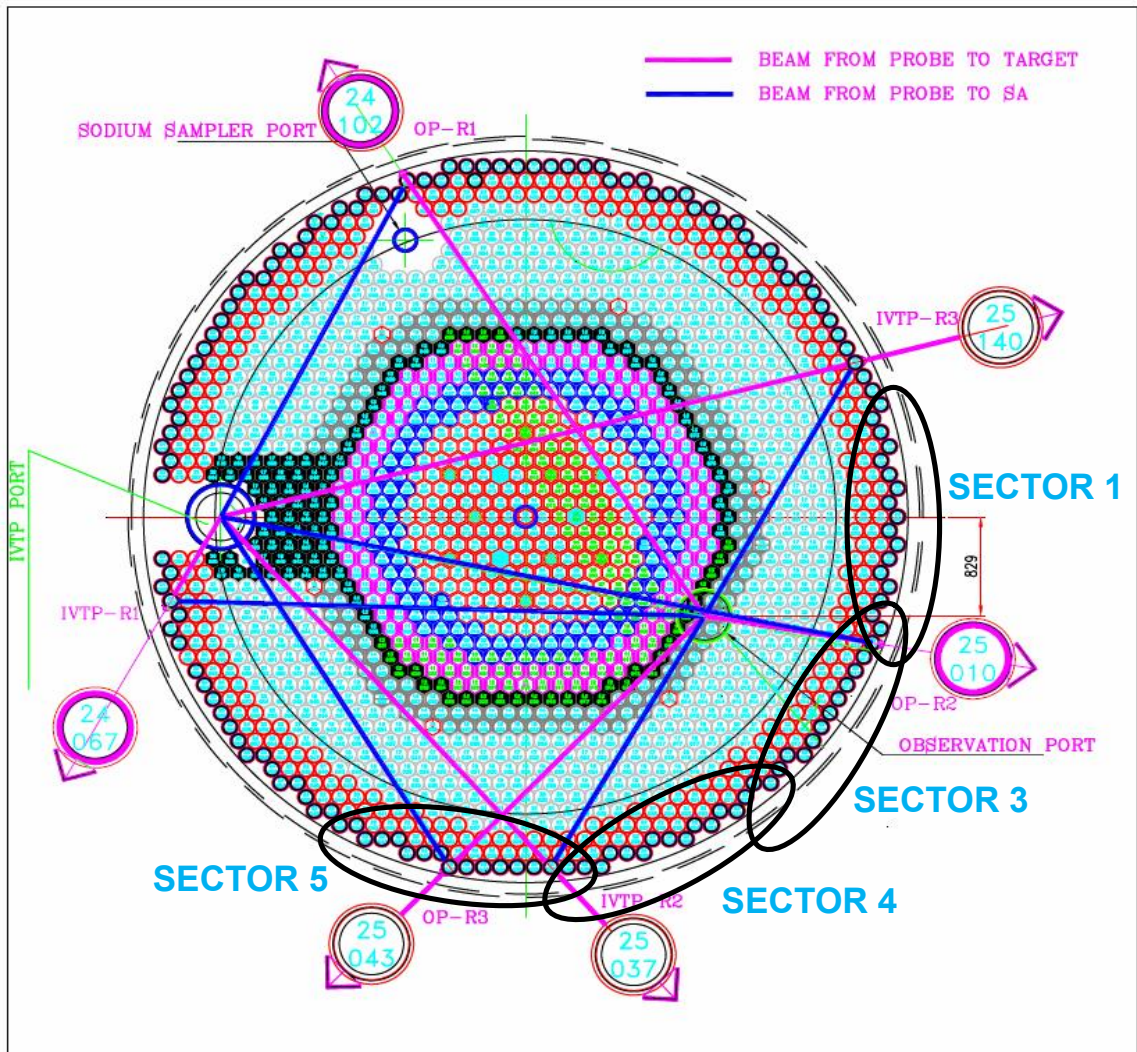


**Fig. 4.17 Reactor Core of PFBR**

- **Experiments in Sector -1**

Sector-1 is simulated at a distance of 4.3 m in water as in Fig. 4.18. The reactor conditions such as average fuel subassembly growth of 20 mm as shown in Fig. 4.19 and the above core plenum of 90 mm from normal subassembly top were simulated in water setup. Actual gap between normal subassembly top to bottom of thermowell sleeves is 90 mm. Due to the growth of fuel subassembly, the gap is considered as 70 mm which is conservative. The experiment is simulated for IVTP access port location, where dummy subassembly (i.e., no growth) is present beneath the transducer holder during scanning. The transducer is positioned

25 mm above the normal SA top. Therefore, the effective ultrasonic scan region is 65 mm from transducer position. The actual distance in the reactor is 5137 mm whereas in the simulation it is 4300 mm in sector -1 due to dimensional limitation of water tank. Overlap between sectors (3 SSAs) are made in order to avoid missing information due to beam divergence effect.

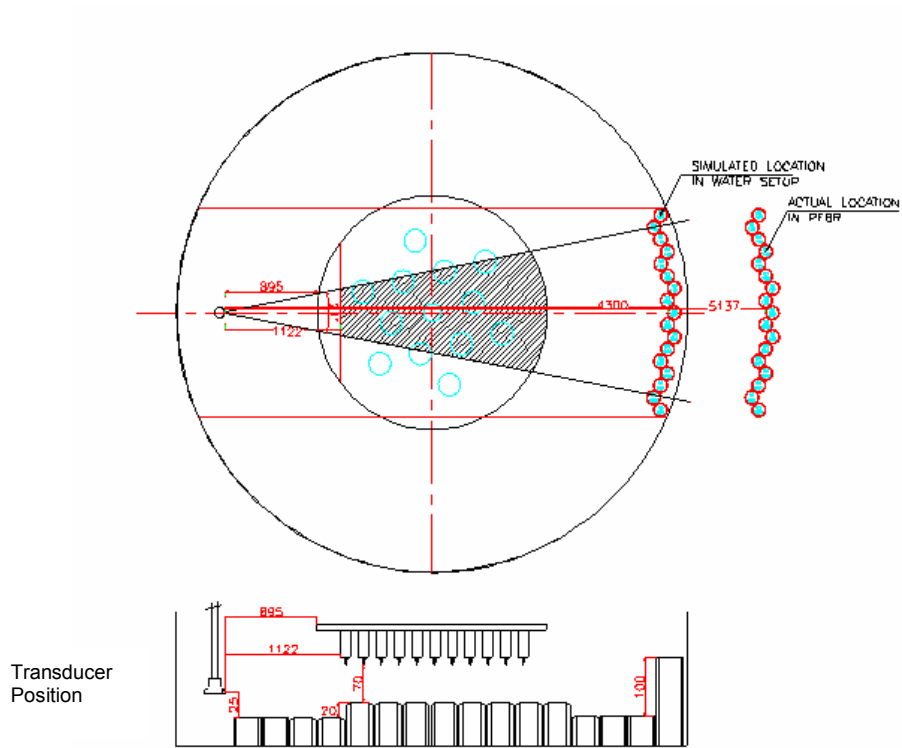


**Fig. 4.18 Sector-1 in Water Setup**

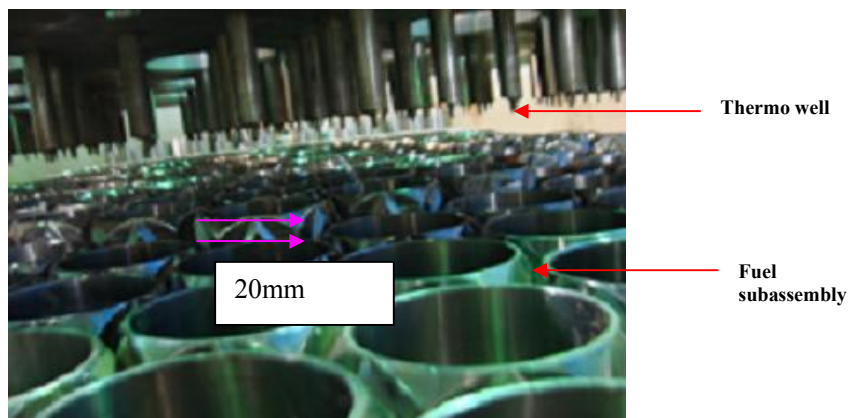


**Fig. 4.19 Simulation of 20mm growth of fuel subassembly**

As the signal strength is not uniform from all the cylindrical SSA, experiments are carried out at 3 different conditions. The photograph of sector-I is shown in Fig. 4.20

- Protrusion of objects at same angle at different distances
- Protrusion of objects at different angles at same distances
- Protrusion of conical portion of CSRDM from top of the thermowell (T/W) sleeves

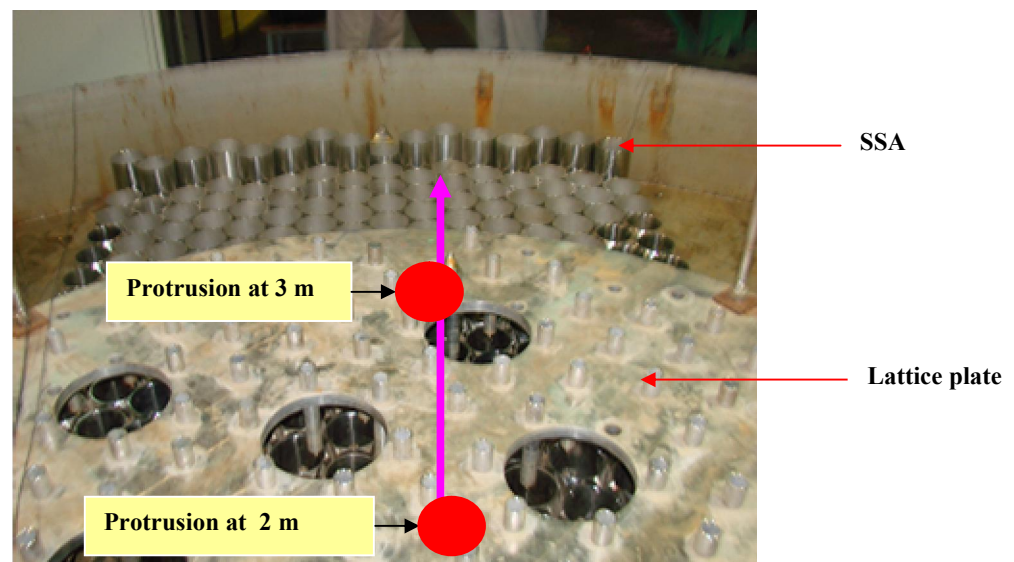


**Fig. 4.20 Photograph of Sector-I setup simulating protrusion at same angle at different distances from 1 m ,2m &3m**

- **Protrusion at same angle at different distance**

The ultrasonic data are collected using a PC based automatic scanning system for various conditions, such as without any protrusion which serves as a reference data and for 65 mm growth of fuel subassembly at various distances of 1 m, 2 m and 3 m leaving clear space of 25 mm from the top of the thermowell sleeve. Then protrusion is made at different distances 1 m, 2 m and 3 m at same angle. From the collected data, C-scan image is constructed using summation algorithm with angle specific gating as shown in Fig. 4.21. The dip in amplitude

shows the angle at which the object is protruded. In C-scan image, the protruded object is marked with an arrow. The C-scan image obtained shows that there is no useful data from 0 to 25 mm of ultrasonic scan region.

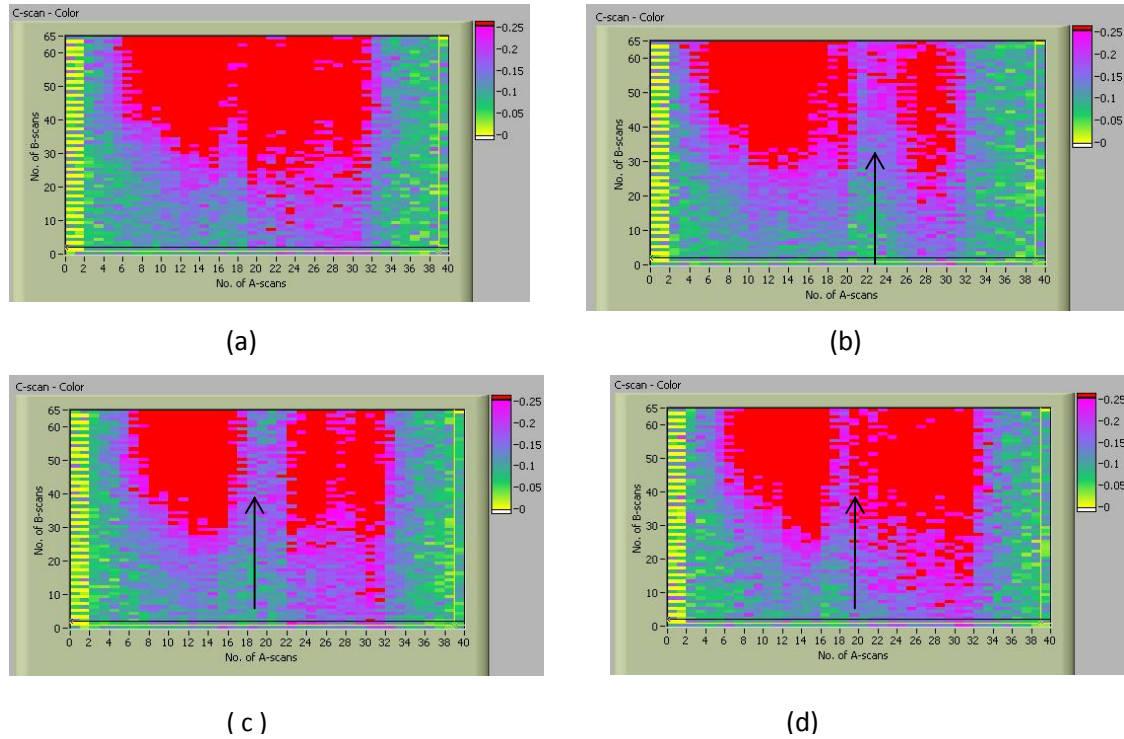


**Fig. 4.21 Sector -1 C-Scan image by protruding the SA at same angle**

**(a) Background (b) protrusion at 1 m distance (c) @ 2 m (d) @ 3 m**

It is found that there is a clear dip in echo signal strength at same angle (one subassembly left or right) at different distances. As the protrusion is nearer, the blocking effect is seen in wider angles compared with protrusion at longer distance. The same effect is seen in the C-scan images. The variable gating is selected in such a way that from the bunches of echo, the peak amplitude echo is targeted.

- **Protrusion at same distance at different angles**

The experiment has been carried out by protruding the object at same distance in different angles. The object simulation is shown in Fig. 4.22. The fuel subassembly is protruded at different angles at same distance of 2 m. The C-scan image is represented in Fig. 4.23. From the image, it is found that there is a clear decrease in the signal strength and was represented in arrow. The experimental results show that the protrusion is detectable at different angles at same distance through above core plenum.

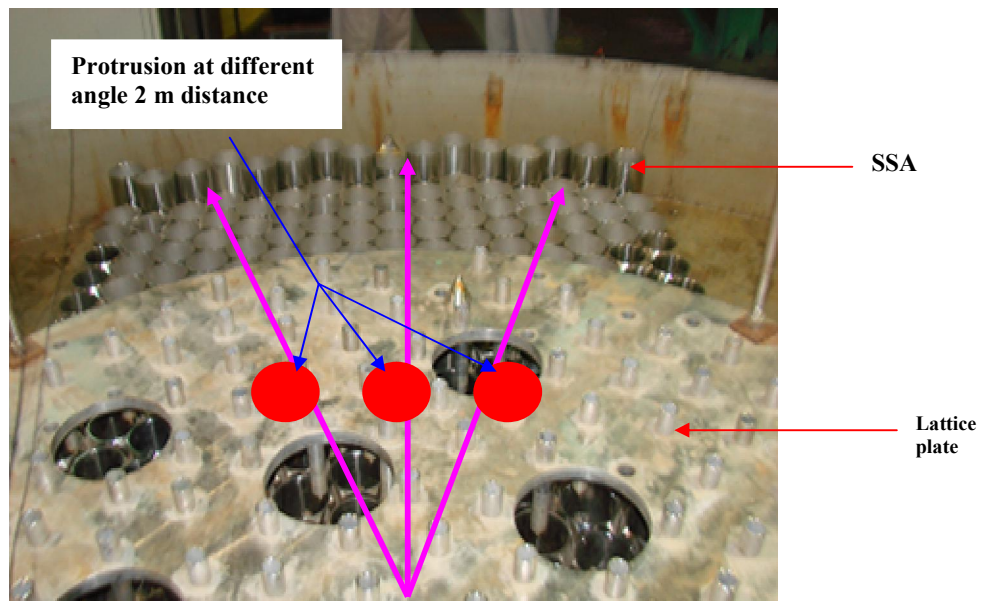


**Fig. 4.22 Photograph of Sector-I setup simulating protrusion at different angle at same distances (2m)**

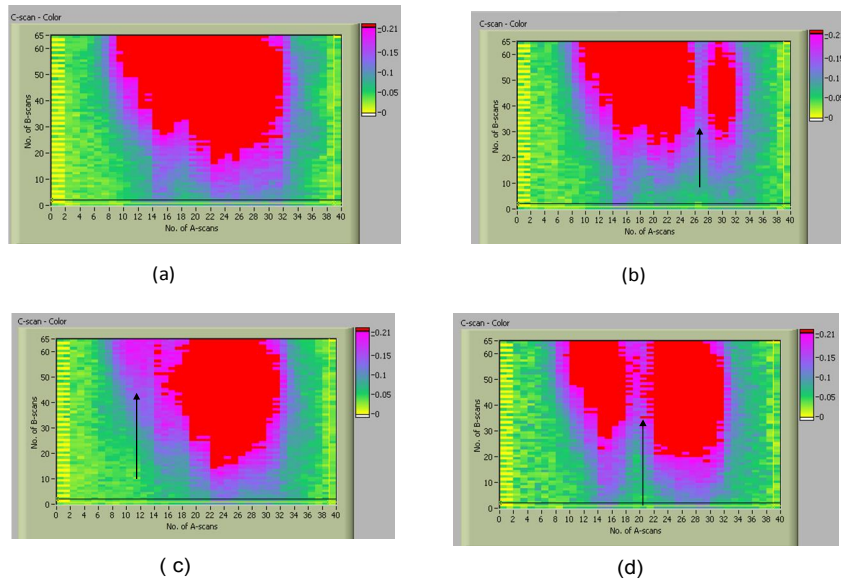


**Fig. 4.23 C-Scan image of protruded SA at same distance(2 m) with different angles**

**(a) Background (b) protrusion @ right (c) @left (d) @centre**

- **Protrusion of CSRDM**

As the CSR conical portion is not detectable by direct imaging technique, experiments have been carried out in Sector-1 by protruding the conical portion of CSR from the top of the core cover plate ( Fig. 4.24). The CSR conical portion is adjusted in such a way that 60 mm of the conical portion is protruded from the bottom of the thermowell sleeves. The farthest CSRDM slot is selected to simulate longer distance of around 2.8 m distance. The C- scan image is taken first without protrusion which serve as a background reference data. Then with various protrusion of conical portion from 60 mm to 20 mm insteps of 20 mm, are simulated and the C- scan image is constructed as shown in Fig. 4.25. From the image it is found that, 60 mm conical portion is detected easily and for protrusion of 40 mm and 20 mm also, there is decrease in the signal strength.

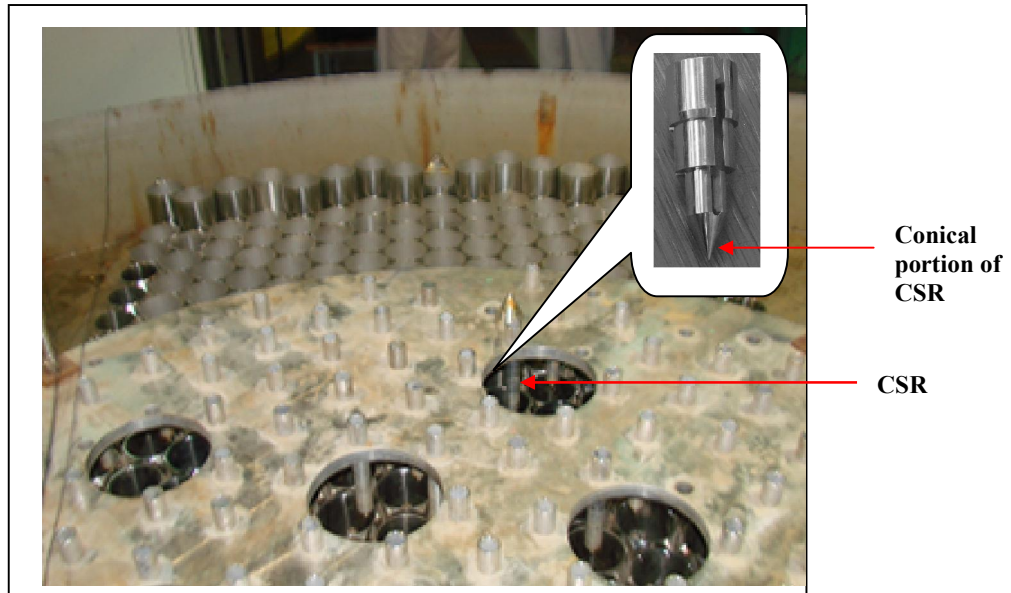


**Fig. 4.24** Photograph showing position of protruded CSR conical portion

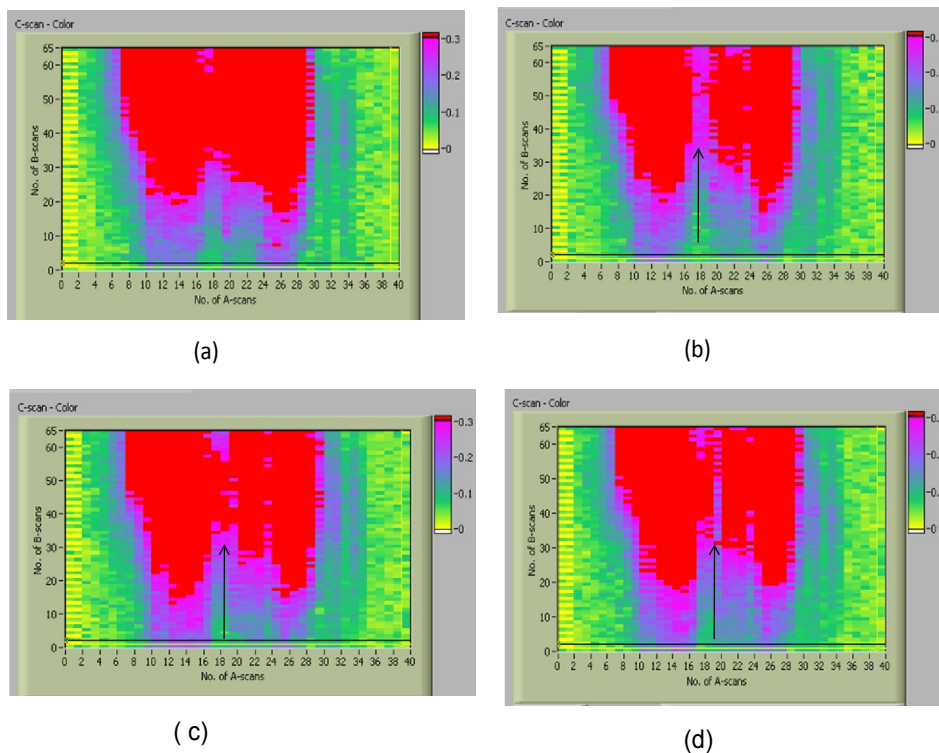


**Fig 4.25** C-Scan image of protruded CSR conical portion at different lengths from top

**(a) Background (b) protrusion of 60 mm CSR conical portion**

**(c) 40 mm CSR conical portion (d) 20 mm CSR Conical portion**

- **Experiments in Sector-4**

The actual distance of sector-4 is 4281 mm and the simulation distance is 3857 mm. The simulation details of sector-4 are shown in Fig. 4.26. The fuel subassembly growth of 20 mm projection is simulated below the lattice plate. The scan is started in the clockwise direction. At the starting portion, the image construction is started from 20 mm elevation and after that, image construction is started even earlier and this is seen clearly in the image which represents the normal subassembly.

The photograph of Sector -4 is shown in Fig.4.27 with retro. The experiment is carried out with and without retro. The C-scan image without retro is shown in Fig. 4.28 (i). The protrusion is made on FSA beneath the core cover plate at different distance without retro. The C- scan image is plotted and found that protrusion is detectable and is represented by arrow in the figure. Again experiment is carried out with retro and projection is made at different angles other than fuel subassembly and the image is obtained. The protrusion is clearly visible in the image as shown in Fig. 4.28(ii).

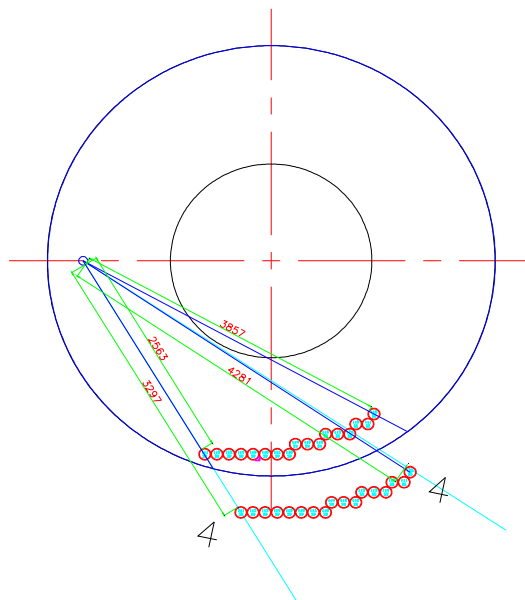


**Fig. 4.26 Simulation details of Sector-4**



**Fig. 4.27 Photograph of Sector-4**

Sector-4 without retro

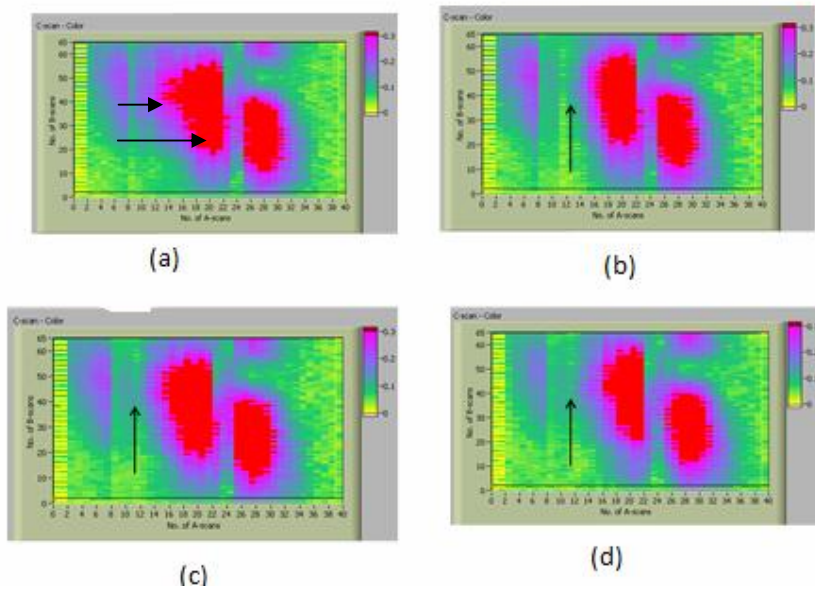


**Fig. 4.28 (i) C- scan image of protruded object at 1m,2,and 3m**

**(a) Background (b) protrusion @ 1 m distance (c) @ 2 m (d) @ 3 m**

### Sector-4 with retro

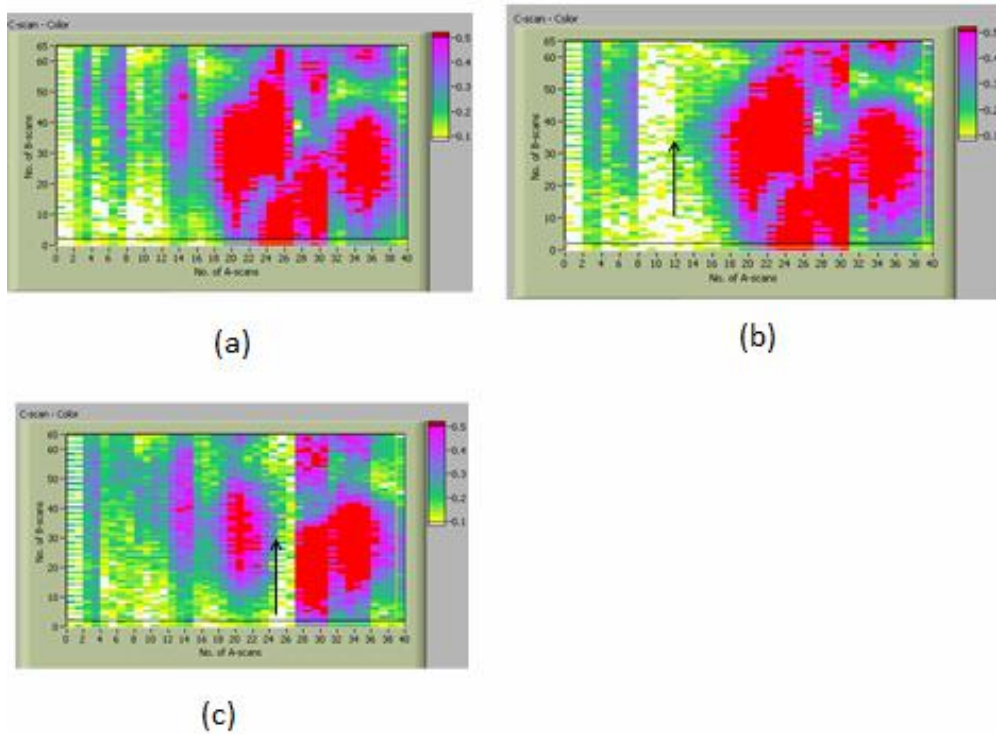


**Fig. 4.28 (ii) C- scan image of protruded object at 1m, 2m distance**

**(a) Back ground (b) protrusion at 1 m (c) @ 2m**

- **Study on effect of inclination of SSA**

A cylindrical blocking subassembly is kept at a distance of 4300 mm away from the transducer with ultrasonic beam passes through the above core plenum of 90 mm. Initially, the background data is obtained by taking  $10^\circ$  sweep in B-scan at 45 mm elevation. The A-scan data is obtained as shown in Fig. 4.29. Then the SSA is inclined to  $0.22^\circ$  using the shim. The signal strength is obtained from B-scan and A-scan data. With different inclination in steps of  $0.22^\circ$ , up to  $0.86^\circ$  is obtained. It is found from Fig. 4.29 that beyond  $0.44^\circ$ , the signal strength is weak and not detectable which shows that inclination up to  $0.44^\circ$  is tolerable to ultrasonic beam.

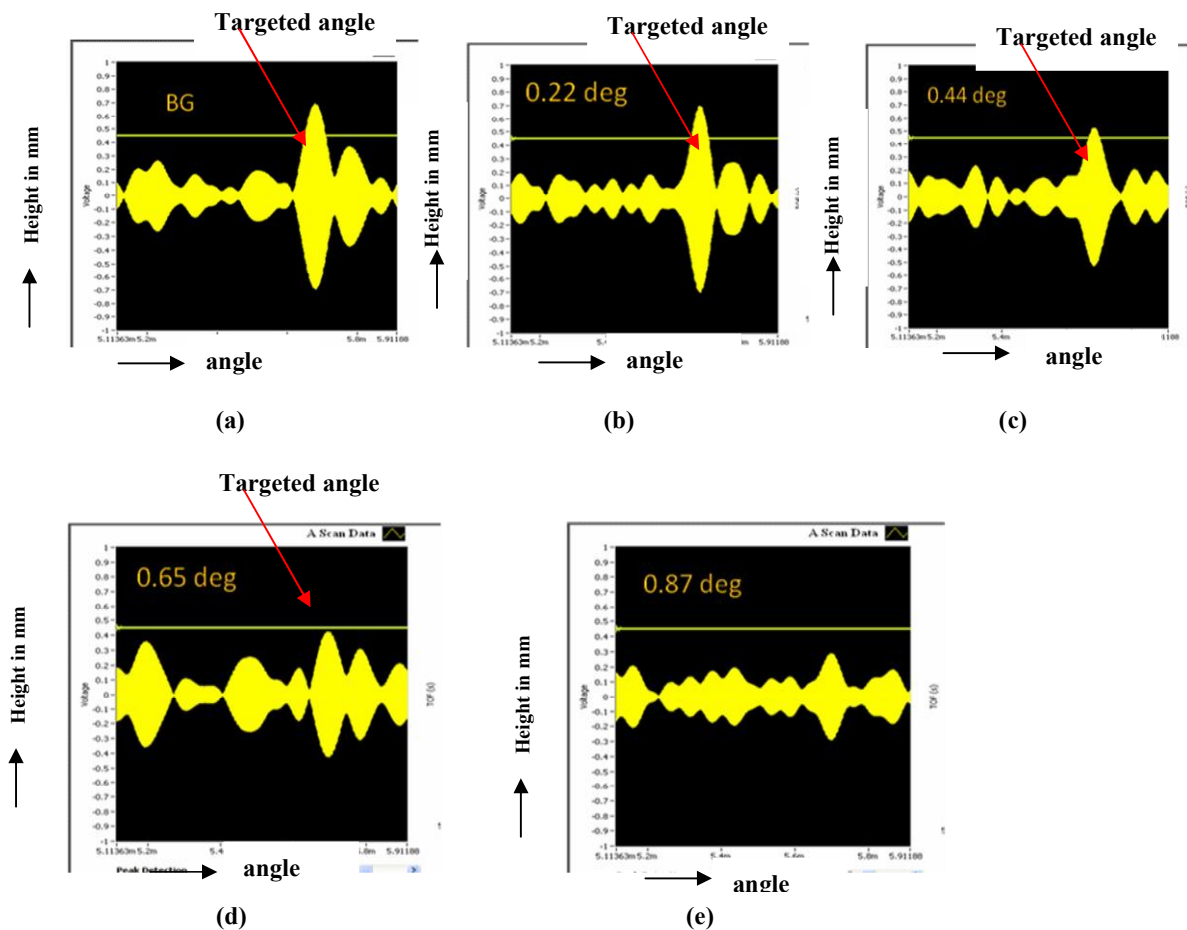


**Fig. 4.29 Echo from single SSA at different inclination**

**(a) Background (b) SSA inclined at 0.22°(c) SSA inclined at 0.44°**

**(d) SSA inclined at 0.65° (e) SSA inclined at 0.87°**

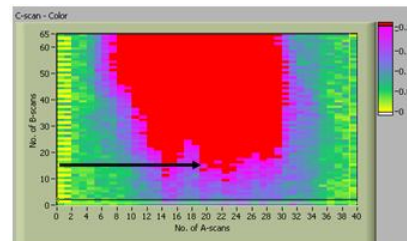
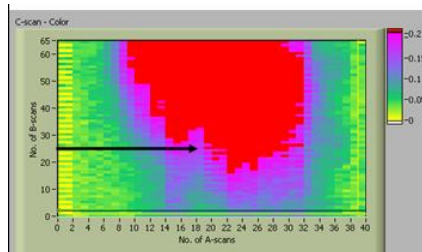
- **Study on Random protrusion**

In the reactor, once in every ~8 months fuel handling operation is carried out and one third of the core will be handled. The freshly loaded fuel subassembly grows to a smaller extent than the old fuel subassemblies. The probable maximum growth of the fuel subassembly is ~20 mm which is due to neutron irradiation and differential expansion. Therefore, the experiments are carried out by providing equal protrusion of 20 mm growth and the random protrusion of partially 5 mm, 10 mm , 15 mm and 20 mm growth. This

experiment is carried out in sector-I and C- scan images are obtained. The result shows that some more information is available in random growth and it starts from 15 mm elevation onwards and for equal growth, information starts from 25 mm only. Therefore result obtained from simulation of equal fuel subassembly growth is conservative.

**BG- Equal 20mm growth of FSA**

**BG- random growth (5-20) mm**



**Useful scan region starts from 25mm**

**Useful scan region starts from 15mm**

**(a)**

**(b)**

**Fig. 4.30 Effect on random and equal protrusion of SSA**

**(a) Background from 20mm equal growth of fuel subassembly**

**(b) Background from 5-20mm random growth of fuel subassembly**

#### **4.4.4 Discussion on Results**

Experiments have been carried out in water simulating the beam divergence effect equivalent to that of sodium. The core cover plate with thermowell sleeves is simulated and various experiments have been performed simulating the reactor sectors. Sufficient overlapping between sectors are provided to avoid loss of information. Beneath the core cover plate, Fuel subassemblies are located and which will undergo maximum growth of 20mm. Equal growth of fuel subassemblies are provided in the simulation experiments. The angle specific gating algorithm is selected for detecting the protruded object. The signal strengths from the SSA at different orientations are not the same and hence experiments have been carried out to detect the protrusion of object at different angles and also at different distances. From the results it is found that protrusion detection is possible up to 3 m distance at any angle. The detection capability is restricted to 3 m only. The conical portion of

CSRDM is also detectable using indirect imaging technique. The effect of inclination of SSA beyond  $0.44^\circ$  in vertical plane with respect to ultrasonic beam is not detectable.

#### **4.5 CLOSURE**

A PC based automatic scanning system has been designed and developed to carry out the experiments. Critical reactor components, namely, CSRDM/DSRDM/CSR have been simulated by keeping the complex shapes to true dimensions and cylindrical surface at reduced height to carry out the experiments. Ultrasonic imaging software with special offline features and different ways of representing the ultrasonic signals such as A-scan, B-Scan and C-Scan displays have been developed and utilized for imaging the reactor components. Different case studies have been carried out.

It is seen that, the cylindrical shapes are easily detectable while the conical shapes cannot be detected. However, conical shapes along with 10 mm cylindrical surface in the above core plenum are detectable. Two cylindrical surfaces of varying dimensions can be identified by the change in the transit time which is represented by two different colours in the C scan display. A sudden change in the dimension of cylindrical surface shows a slight discontinuity in the image when amplitude of thresholding is increased. A small taper portion within the cylindrical surface cannot be identified in the image due to beam divergence effect. The distances of various objects are obtained by the B-Scan data at that elevation.

The DSRDM has a rectangular slot and conical portion. The cylindrical portion of DSRDM without rectangular slot and DSRDM with rectangular slot are detected as they give strong echoes. Echo is not received from conical portion which is at the extreme end. In the case of CSRDM, the cylindrical portion gives rise to a good image, provided the slot of the CSRDM is not in direct view of ultrasonic transducer beam. The conical portion does not give back echo irrespective of position of the slot. The CSR consists of cylindrical

portion at both the ends with conical portion in the middle. Experiment shows that conical portion does not give back echo but the cylindrical portion at both the ends give sufficient amplitude echoes. Therefore CSR can be ultrasonically imaged using direct imaging technique in all possible conditions.

In the case of indirect imaging technique, protrusion of objects which is geometrically unfavorable to ultrasonic beam can be detectable using angle specific gating with summation algorithm. Initially, without any protrusion, the core is scanned and the C-scan image is constructed which serves as the reference data. The gating is set based on reference data targeting SSA. The objects such as hexagonal subassembly having differential growth of 45 mm can be detectable as observed in water experiments. The objects such as the conical shape or any irregular shape hanging from the top of the thermo well sleeves by 20 mm is also detectable. The inclination effect of peripheral SSA is also studied and found that  $0.44^\circ$  inclination in vertical plane with respect to ultrasonic beam is tolerable to ultrasonic beam.

The direct imaging method is efficient when the protruded objects are favorably oriented to ultrasonic beam (30 %). In such cases, the protruded object can be easily localized using direct imaging method. But if the protruded objects are unfavorably oriented to ultrasonic beam (remaining 70 %), indirect imaging method is used to find the angle at which the object is protruded. To localize the protrusion, the scanner will be deployed in Observation Port also and from the intersection point, the protrusion is localized. Therefore both the methods are required based on the need.

## **CHAPTER - 5**

# **DEVELOPMENT OF MUTUAL INDUCTANCE TYPE SODIUM LEVEL SENSOR WITH A NEW TEMPERATURE COMPENSATION TECHNIQUE**

## **5.1 INTRODUCTION**

The under sodium ultrasonic viewing system efficiently functions only if the components are adequately immersed in sodium pool. This is ensured using level measuring system. Even though the traditional continuous level sensors used in small experimental reactor is also of non contact type working on mutual inductance principle, for large power reactors robust, longer length (~ 10 m) level probes are required. Hence, the third part of the research work is targeted towards development of a long length level probe with application focused towards PFBR. As the temperature gradient is more for longer probes, better temperature compensation technique is required and a new temperature compensation technique has been devised to improve the accuracy which also simplifies the electronics. Detailed developmental activities in sensor, new temperature compensation technique, studies to improve the sensitivity, its electronics and sodium testing results are discussed in this chapter.

As already discussed in chapter-1, the primary and secondary circuits of FBR have a large number of free liquid –sodium surfaces. Control of the relative level is important during various conditions of the reactor operation. Hence, a large number of measurements of high temperature sodium level sensors are required. As an alkali metal, sodium is highly reactive with air and water and it is incompatible with many commonly used engineering materials. In addition to the essential requirement of compatibility of the sensors used with liquid sodium up to 823 K, the integrity of the system should be maintained even in the case of breach of the sensor. So, conventional instrumentation devices cannot be readily used in sodium systems. The above requirements necessitate specially developed sensors for use in

liquid sodium. The characteristics required for level sensors include (i) wide and high operating temperature with simple temperature compensation technique, (ii) should be of non contact type with minimum weld joints, (iii) should not depend on wetting effects and (iv) should be robust and withstand cross flow during normal operation. Operationally the levels at the pool region and secondary circuit must be measured continuously to find the gross sodium hold up in the primary circuit, to ensure that an adequate level is maintained at the heat exchanger inlet to prevent vortex and gas entrainment and also to monitor entry of secondary sodium into primary sodium. The typical installations of level sensors in PFBR is shown in Fig. 5.1

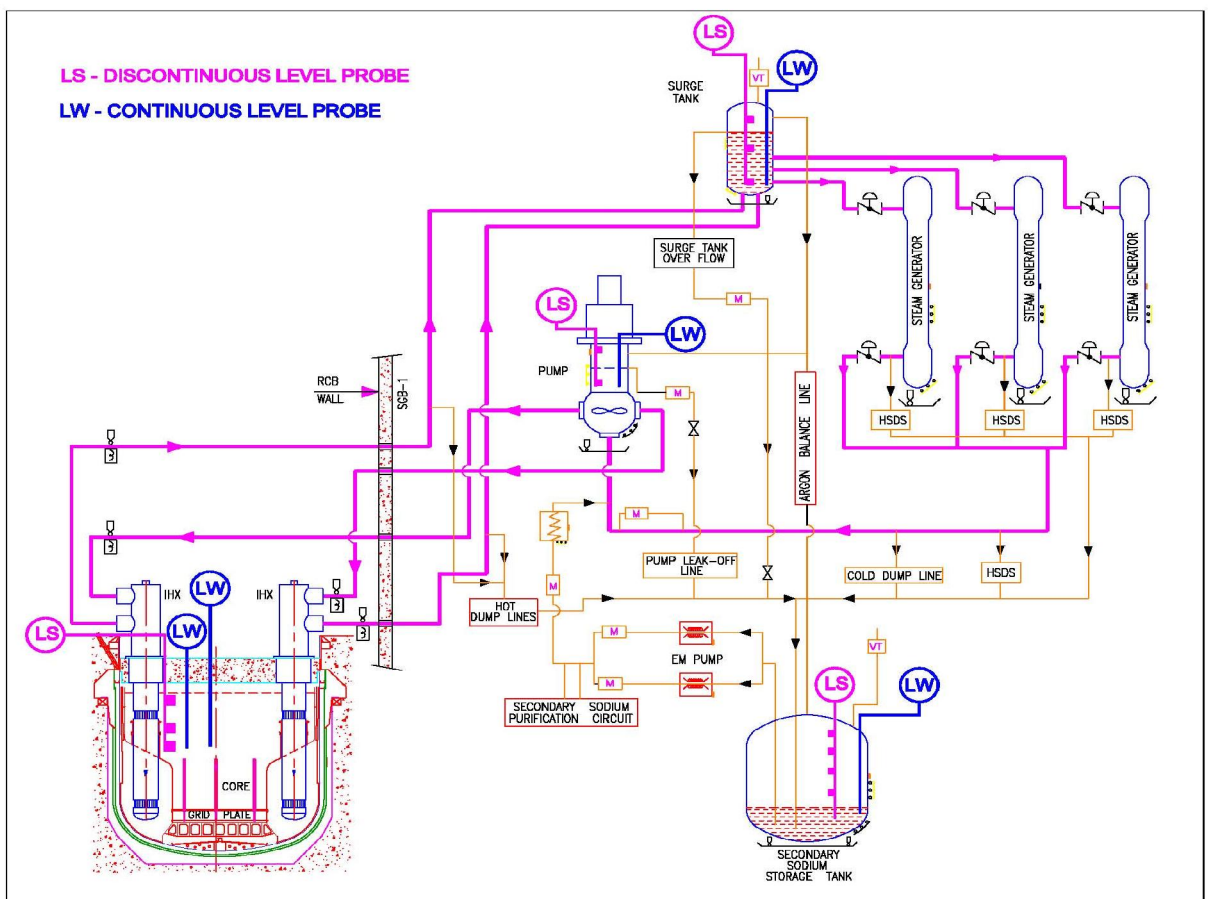


**Fig. 5.1 Typical Installation of Level sensors in PFBR (LS-Discontinuous level probe, LW- Continuous level probe) (Safety Report on PFBR)**

Discontinuous level measurement is needed to guard against any gross loss of coolant from the system. It is used for safety purposes and also provides redundancy. Typical discrete level sensors works on the principle of step change in resistance when sodium touches the sensing portion. The major disadvantages of this system include (i) poor wettability at low temperature (200°C) and (ii) effect of vapor deposition on probe surface. To overcome these problems, non contact, mutual inductance type discontinuous level sensors are essential.

## 5.2 THEORY OF LEVEL PROBES

Consider a long solenoid, wound in insulated wire and is surrounded by a liquid metal of high electrical conductivity. If a constant alternating current is passed through the solenoid, the alternating flux produced will induce alternating electro motive forces in the surrounding liquid metal. Schematic of magnetic field lines due to current through the solenoid are shown in Fig. 5.2. Each turn produces circular magnetic field lines near itself. Near the solenoid's axis, the field lines combine into a net magnetic field that is directed along the axis. The closely spaced field lines there indicate a strong magnetic field. Outside the solenoid, the field lines are widely spaced, where the field is very weak.

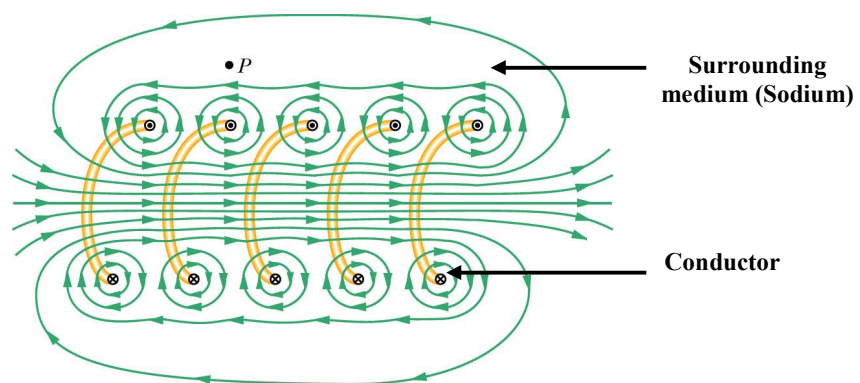


**Fig. 5.2 Magnetic field lines due to a current through the solenoid**

The surrounding liquid metal contributes to this reduction in self inductance. An annulus of liquid sodium of thickness equal to twice the skin depth corresponding to the operating

frequency, is virtually equivalent to an infinite sea of sodium (Mcgonigal, 1971). The change in self inductance is proportional to the depth of immersion. The measurement of self inductance of the coil is hampered by the series resistance of the winding. When the series resistance is high and the self inductance is low, the measurement becomes very difficult and inaccurate. To overcome this, bifilar coil system is used, where the effect may be regarded as change of mutual inductance between the two coils. When alternating constant current is fed into primary coil, e.m.f. induced in the secondary does not depend on resistances of the coils. It depends only on coefficient of coupling and the magnitude of eddy currents produced in the surrounding medium. Change of inductance is caused by eddy currents which produce a magnetic field in opposition to that produced by the primary current in the coil. The penetration of these eddy currents into the surrounding conducting medium is a function of the resistivity of the medium and the frequency of input current. Expressions for mutual inductance (M) and e.m.f induced in secondary coils (e) are given below.

$$M = \frac{\mu_0 \mu_r N_1 N_2 \pi r^2}{l} \text{----- (5.1)}$$

$$e = -M \frac{dI}{dt} \text{----- (5.2)}$$

$$M = k \sqrt{L_1 L_2} \text{----- (5.3)}$$

Where  $k$  is the coupling factor, for loosely wounded windings  $k \neq 1$

$L_1$  self inductance of primary coil

$L_2$  self inductance of secondary coil

M mutual inductance between coils

The induced magnetic vector potential at (r, z) (Nestor, 1979) produced by a driving coil with a fixed alternating current in solenoid coil is given below.

$$A^{(1,2)}(r, z) = \frac{\mu_0 I_1 n_1}{\pi(r_2 - r_1)(l_2 - l_1)} \int_0^\infty \frac{1}{\alpha^3} \{ [I(r_2, r_1) * I_1(\alpha r) \Sigma(\alpha)] * [\sin \alpha(z - l_1) - \sin \alpha(z - l_2)] \} \\ + \frac{\pi}{2} J(r_2, r_1) J_1(\alpha r) (2 - e^{-\alpha(z-l_2)} - e^{-\alpha(z-l_1)}) \} d\alpha \text{-----} (5.4)$$

$r_1$  Inner radius of coil

$r_2$  Outer radius of coil

$l_1$  Distance from bottom of coils to  $z = 0$  plane

$l_2$  Distance from top of coils to  $z = 0$  plane

$l = (l_2 - l_1)$  Coil length

$n_1$  Number of primary coil turns

$n_2$  Number of secondary coil turns

$I_1$  Primary exciting current

$\mu_0$  Free space permeability

$\alpha$  Separation constant

$z$  Transfer impedance

$\omega$  Angular frequency of  $I_1$

Alternating magnetic field produced by current in primary coil along with magnetic field produced by eddy currents generated in surrounding electrically conducting mediums led to generation of e.m.f in secondary coil. E.m.f induced in secondary coil is given below.

$$V_2 = \frac{j2\omega n_1 n_2 I_1 \mu_0}{(r_2 - r_1)^2 (l_2 - l_1)^2} \int_0^\infty \frac{1}{\alpha^6} \{ 2I^2(r_2, r_1) \Sigma(\alpha) [1 - \cos \alpha(l_2 - l_1)] + \pi J^2(r_2, r_1) [\alpha(l_2 - l_1) + e^{-\alpha(l_2 - l_1)} - 1] \} d\alpha \text{-----} (5.5)$$

### **5.3 PRINCIPLE OF OPERATION**

The Mutual Inductance type Level Probe (MILP) works on the principle of variation of mutual inductance between two windings when they are in the proximity of an electrically conducting fluid such as sodium. The MILP has two windings wound in bifilar fashion on a non-magnetic stainless steel former. The probe is inserted in a stainless steel pocket. The primary winding of the probe is excited with an AC constant current at a constant frequency. Due to mutual inductance, an electro motive force is induced in the secondary coil. The liquid sodium surrounding the probe acts as a short-circuited winding, because sodium is a good electrical conductor. An electro motive force will be induced in sodium also and the eddy current flows in it. The magnetic flux due to eddy current will oppose the main flux produced by the primary winding. Hence, the net flux linked with secondary decreases and thereby the secondary voltage reduces when the sodium level increases. The secondary voltage is an inverse linear function of the sodium level. When the sodium temperature increases, the resistivity of sodium increases. Hence, the eddy current decreases and the induced voltage in secondary coil increases. So, temperature compensation is required in order to make the output voltage independent of temperature.

### **5.4 CONSTRUCTION OF LONG LENGTH LEVEL PROBE**

The sensor consists of sensing element called bobbin and pocket. Traditional level probes R have short active lengths (2.5 m). As long length level probes are required for large power reactors, free insertion and withdrawal of the bobbin into the pocket is required. Therefore, the radial clearance between pocket and bobbin has to be liberal. For the present purpose, a standard pipe of size 1¼” SCH10 (42.16 mm OD, 36.62 mm ID) as pocket and 28 mm diameter bobbin are selected. From the practical point of view, the measurement of the self inductance of a coil is hampered by the series resistance of the windings. To overcome this difficulty bifilar coil system is used.

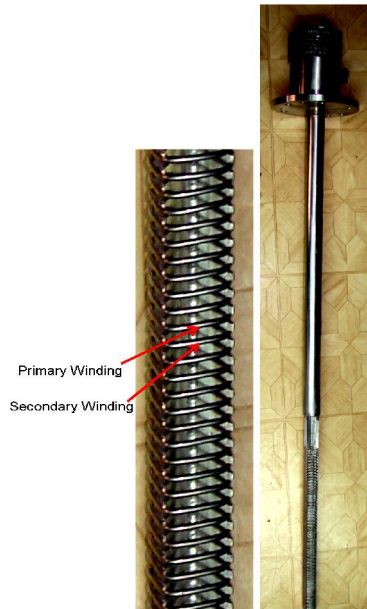


**Fig. 5.3 Mutual Inductance type continuous level probe**

MILP consists of primary and secondary coils wound in bifilar manner on a stainless steel former of cross-shaped cross section as shown in Fig. 5.3. For the high windings, stainless steel sheathed, Mineral (MgO) Insulated (MI) cable with a copper conductor is used. The primary and secondary coils are wound inside the slots provided in the bobbin. The slots are made in the cross shaped bobbin using Electric Discharge Machining technique. In order to avoid sharp corners in the slot, curved electrodes are used so as to prevent damage to MI cable sheath during winding. Slots are provided upto active length of the probe. The depth of the slot is designed such that the MI cable does not get damaged during installation of the probe into pocket and also during handling.

For the present application, probes of total length of 9.6 m are required. To assess the fabricability of long length level probes, a prototype mutual inductance type continuous level probe of active length 6.0 m and non active length 3.6 m has been fabricated. The difficulty of fabricating 6 m long sensing element as a single piece, was solved by providing 3 sections, each of 2 m in length. To ensure very low distortion, a welding jig was fabricated to hold the

bend strips in position for laser welding which was also used for joining the 2 m sections to form 6 m bobbin. Special fixtures and a dedicated winding table with rotary holders were fabricated to hold the bobbin while winding the MI cable. For making a long pocket long welding table was fabricated using machined aluminum plate and V blocks. The long tubes were straightened using hydraulic/screw press and finally the straightness of  $\pm 1$  mm per meter was achieved. The robust and long length level probe has been fabricated successfully.

Further, provision has also been made in the pocket to detect the sodium leak using spark plug type leak detector. Leak tight arrangement is achieved using Lip-seal welding, instead of O-ring arrangement due to high temperature. A stainless steel ring with bolt-nut arrangement is used to avoid load on Lip seal welding. To provide biological shielding, SS balls were used instead of stainless steel blocks for free insertion of MI cable as shown in Fig.5.4. In order to provide leak tightness, MI cable is brazed with stainless steel flange using high temperature brazing alloy. For this, a number of mockups have been carried out successfully to study the fabrication feasibility, as the MI cables are fragile and brazing them to stainless steel flange without affecting the thin copper conductor inside posed a major challenge.

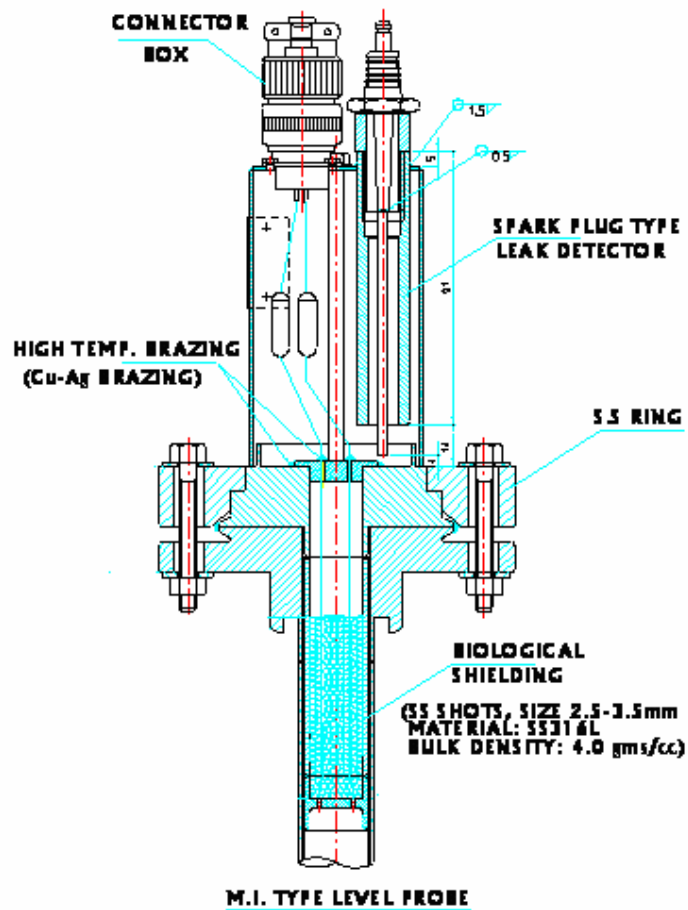


**Fig. 5.4 M.I type level probe with Biological Shielding**

## **5.5 PERFORMANCE EVALUATION**

The gap between the ID of pocket and OD of bobbin needs to be kept to a minimum to achieve maximum sensitivity. To study the effect of dimensional change in bobbin and the pocket, on sensitivity and temperature coefficient, the prototype probe is tested in sodium at various temperatures ranging from 200°C-550°C. The probe has been tested for full level and zero level over a temperature range of 200°C-550°C in steps of 50°C. The current fed to primary coil is 100 mA and the frequency of this primary current is varied from 2 kHz to 3 kHz in steps of 0.1 kHz in the above temperature range. The secondary voltage and change in primary voltage at different temperatures are obtained at zero and full levels.

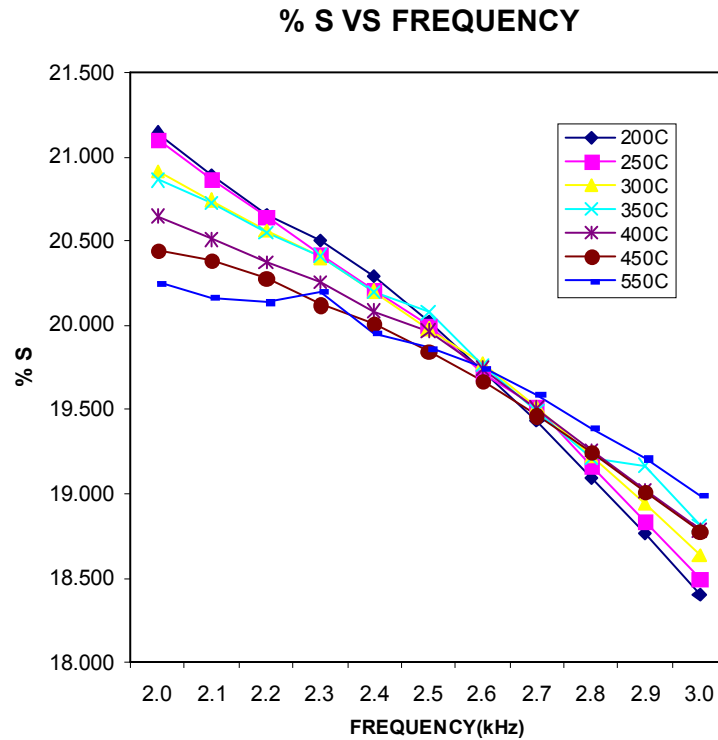


**Fig. 5.5 % Sensitivity Vs frequency**

Using the data a plot is obtained between frequency and % sensitivity (%S) and is shown in Fig. 5.5, where sensitivity is defined by,

$$\%S = \frac{(\text{Zero level secondary voltage} - \text{Full level Secondary voltage}) \times 100}{\text{Zero level Secondary voltage}}$$

It has been found that 2.5 kHz is the optimum excitation frequency to minimize the effect of temperature on the output. The graph shows a crossover at a particular frequency which is due to variation in flux pattern of sodium surrounding the pocket at higher frequencies. Change in the secondary output voltage due to change in level (zero to full) is around 20% and is sufficient enough to adjust in electronics.

## 5.6 DEVELOPMENT ON TEMPERATURE COMPENSATION TECHNIQUE

The probe secondary voltage is a function of sodium level as well as temperature. To find out the actual sodium level using MI probe, effect of temperature on secondary output of

the level probe has to be eliminated. The temperature compensation technique is complicated because of the facts, (i) Electrical conductivities of sodium and stainless steel vary with temperature at different rate, (ii) Temperature coefficient for the sensor uncovered and fully covered with sodium is different, (iii) mutual inductance at both the sodium uncovered and fully covered states increases with increasing temperature but at different rates as shown in Fig. 5.6, and (iv) temperature distribution in the direction of length of the probe cannot be determined because it depends on sodium temperature, sodium level, and temperature at the top of the probe and cover gas temperature (Kuniji, 1975).

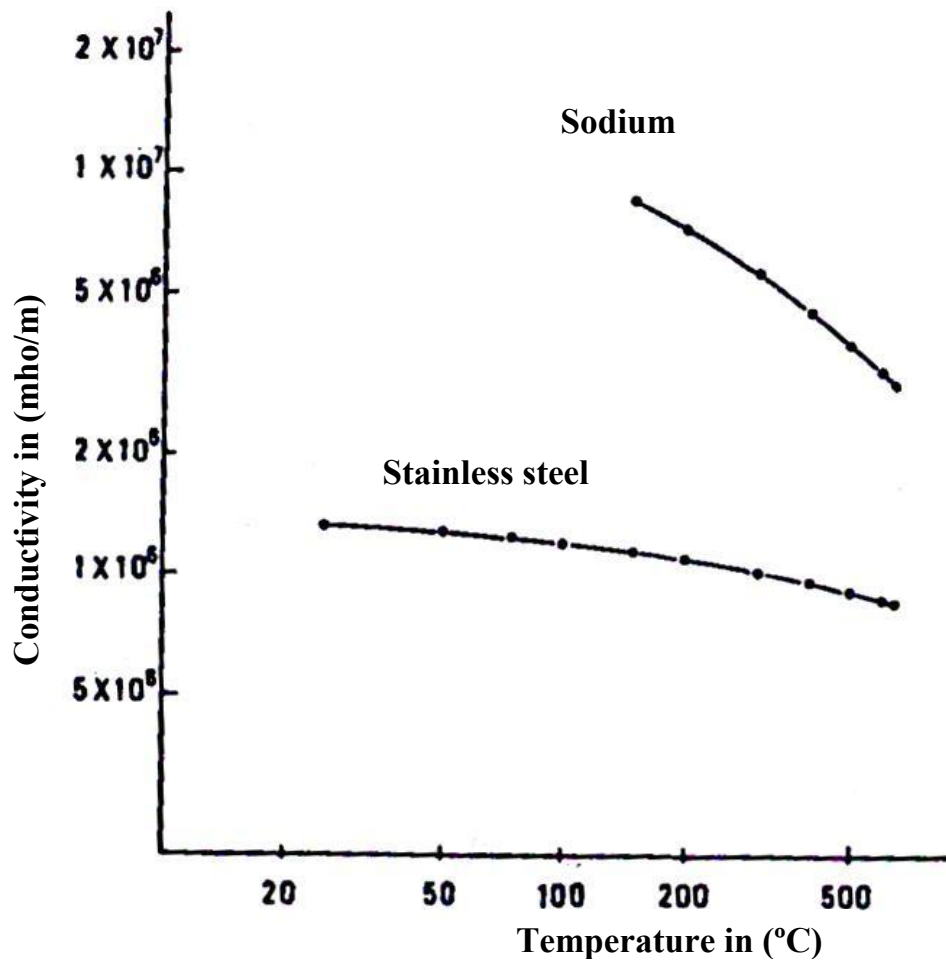
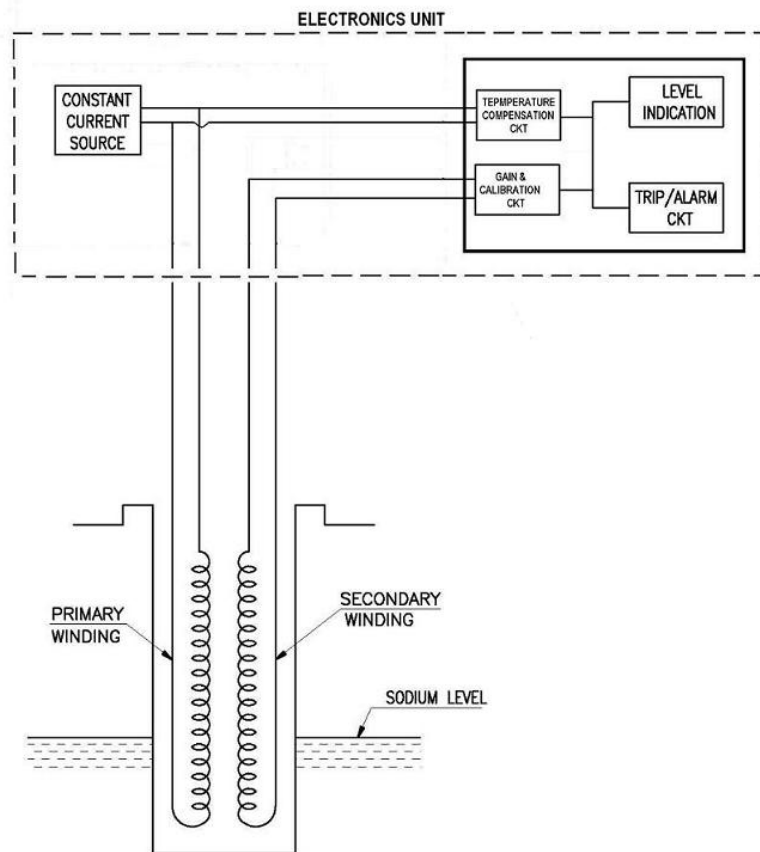


Fig. 5.6 Electrical conductivities of sodium and stainless steel



**Fig. 5.7 Earlier method of temperature compensation**

A basic temperature compensation can be achieved by measuring the primary voltage variation, which is a measure of average temperature of the probe. This method of temperature correction achieved through electronics is shown in Fig. 5.7. The procedure for calibration of electronics is, at the lowest operating temperature the electronics is adjusted for zero level and full level by adjusting gain of an amplifier. At the highest operating temperature, only at full level the temperature compensation amplifier is adjusted to show full level reading. Hence, adjustments are carried out only for full level at two extreme temperatures and this method of temperature compensation is partial. This contributes to an error of  $\pm 3\%$  of span.

### 5.6.1 Principle of new temperature compensation Technique

This method utilizes the internal resistance variation of the coil with temperature and uses variation of internal resistance as a correction factor to compensate temperature effect. In the case of any given level, the internal resistance of the secondary coil increases with temperature. By connecting an external resistance,  $R_{ext}$ , there is a current flow such that the voltage drop within the internal resistance of the probe compensating the increase in the voltage induced within the secondary (Paris et al., 1976). Schematic of the circuit is shown in Fig. 5.8.

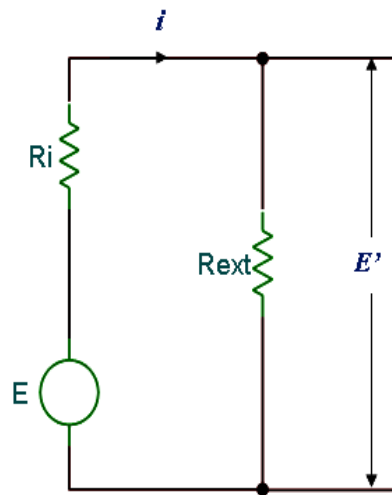


**Fig. 5.8 Schematic of continuous Level probe**

In Fig. 5.8,  $E$  denotes induced voltage in secondary,  $R_i$  denotes internal resistance of secondary,  $i$  is the circulating current and  $R_{ext}$  is the external resistance to be added for temperature compensation. Equation of the circuit in respect of a fixed level of sodium is as follows

$$E' = R_{ext} \times i = \frac{R_{ext} \times E}{R_{ext} + R_i} \text{-----(5.6)}$$

When the temperature varies, the voltage at the terminals of the  $R_{ext}$  varies by  $dE'$ , Which is given by:

$$\partial E' = \frac{R_{ext} \times \partial E}{R_{ext} + R_i} - \frac{E \times R_{ext}}{(R_{ext} + R_i)^2} \partial R_i \text{-----(5.7)}$$

This variation should be reduced to zero (i.e.)  $\partial E' = 0$ ;

Applying this condition to eqn (5.7) we get,  $R_{ext} = \frac{E \times \partial R_i}{\partial E} - R_i \text{-----(5.8)}$

Eqn (5.8) can be written as,  $R_{ext} = \frac{E' \times \Delta R_i}{\Delta E} - R_i$

Where,

$R_i$  = Internal resistance calculated by dividing primary voltage by primary current

$E$  = Secondary output

$R_{ext}$  = External resistance

$\Delta R_i$  = Difference in internal resistance at extreme temperature

$\Delta E$  = Difference in secondary voltage at extreme temperature.

For this calculation, primary resistance is considered as internal resistance of the secondary coil since the winding is bifilar. It is known that secondary output voltage is a function of sodium level, temperature and also the frequency of excitation. Equation 5.3 gives the value of external resistance, which takes care of temperature compensation. Effect of frequency on secondary output is obtained by plotting the value of external resistance and frequency for zero sodium level and full sodium level. The intersection point of these two curves gives value of external resistance for optimum frequency.

### 5.6.2. Experimental Validation

The prototype MI level probe is tested in sodium for implementing new method of temperature compensation technique. At different frequencies the data was collected in sodium for extreme temperature at zero and full level of sodium. The thermocouple measures

temperature of sodium in the heater vessel and required temperature is maintained by PID controller. The calibration procedure is , to fill the sodium at low temperature(200°C) so that the probe to be calibrated is fully immersed in sodium and measure the secondary millivolt and secondary winding resistance at different frequencies. Then quickly drain the sodium so as to maintain same temperature around the pocket at zero level. Measure the secondary millivolt and secondary winding resistance at different frequencies. Follow the same procedure for 550°C. Using Eqn.(5.3), calculate the external resistance at different frequencies. Then plot a graph between frequency versus external resistance. The optimum frequency of operation and the value of external

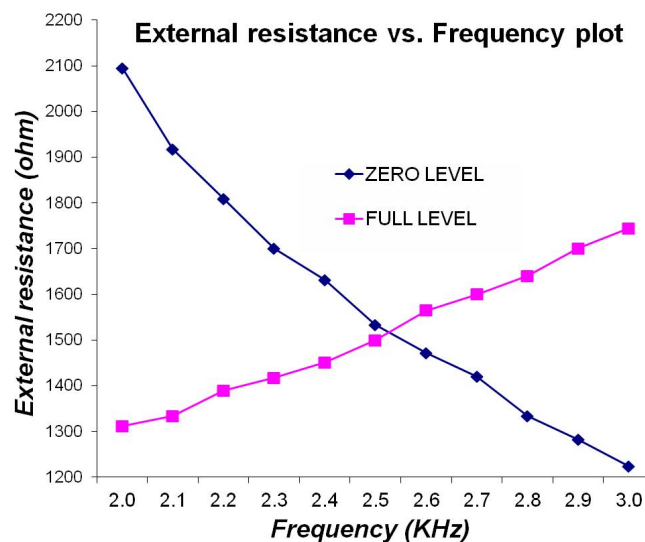


**Fig. 5.9 Frequency vs External resistance**

resistance to be added for prototype level probe at extreme temperature (200 to 550°C) were obtained from intersection point of zero level and full level values as shown in Fig.5.9. This temperature compensation resistor was connected across the secondary of the probe. The level is measured and cross-checked with the Dip-Stick type level probe as reference probe.

**Table-5.1 Secondary output for different temperature with compensation using external resistor**

Sodium level (mm)	Secondary output (mV)				$\Delta E_T$	Error in level (mm)	% Sec.voltage variation w.r.t $\Delta e_{ave}$ for temp. from 200 °C-550 °C
	220° C	350° C	450° C	550° C			
0	146.89	147.05	146.8	146.66	0.39	78	1.33
6000	117.56	117.6	117.35	117.3	0.3	60	1.02
$\Delta E$	29.33	29.45	29.45	29.36	$\Delta E_{Ave} = 29.40$		
%S	19.97	20.03	20.06	20.02	$\%S_{Ave} = 20.02$		
Drop across primary (V)	4.759	6.299	7.317	8.453	Zero Level		
Drop across primary (V)	4.748	6.143	7.12	8.134	Full Level		

$\Delta E$  : Change in secondary O/P from zero level to full level in mV at a particular temperature.

$\Delta E_T$  : Change in secondary O/P in mV w.r.t temperature.

$$\text{Sensitivity} = \frac{\text{Change in secondary O/P from zero level to full level in mV}}{\text{Active length of the probe}}$$

% S : % Variation of secondary O/P w.r.t level change at a given temperature

$$: \frac{\text{Change in secondary O/P } (\Delta E)}{\text{Secondary O/P at zero level}} \times 100$$

$$\text{Error in level} = \frac{\text{Change in secondary O/P w.r.t temperature (mV)}}{\text{Sensitivity (mV/mm)}}$$

$$\left. \begin{array}{l} \text{\% Sec.voltage variation w.r.t } \Delta e_{ave} \\ \text{for temperature from } 200^\circ\text{C} - 550^\circ\text{C} \end{array} \right\} = \frac{\Delta E_T}{\Delta E_{Ave}}$$

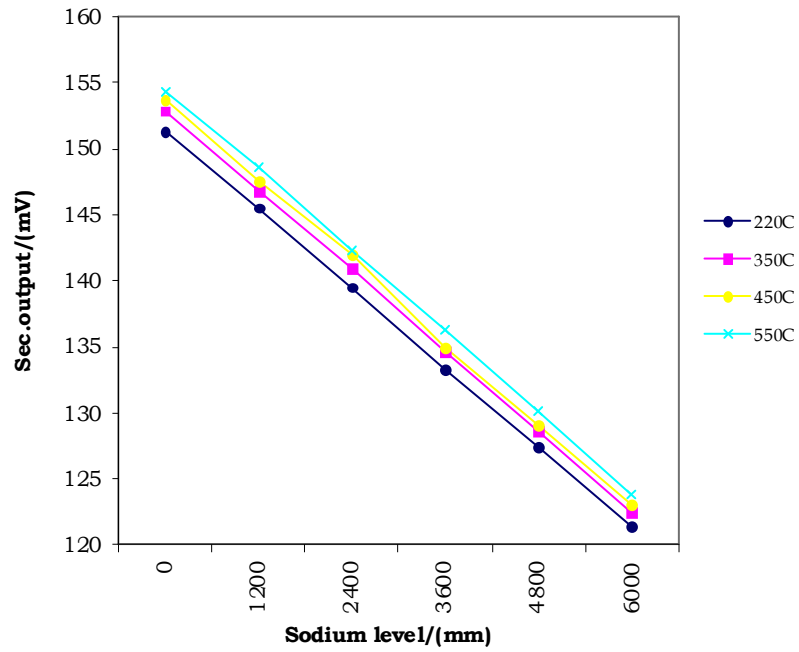


**Fig. 5.10 Secondary output without temperature compensation**

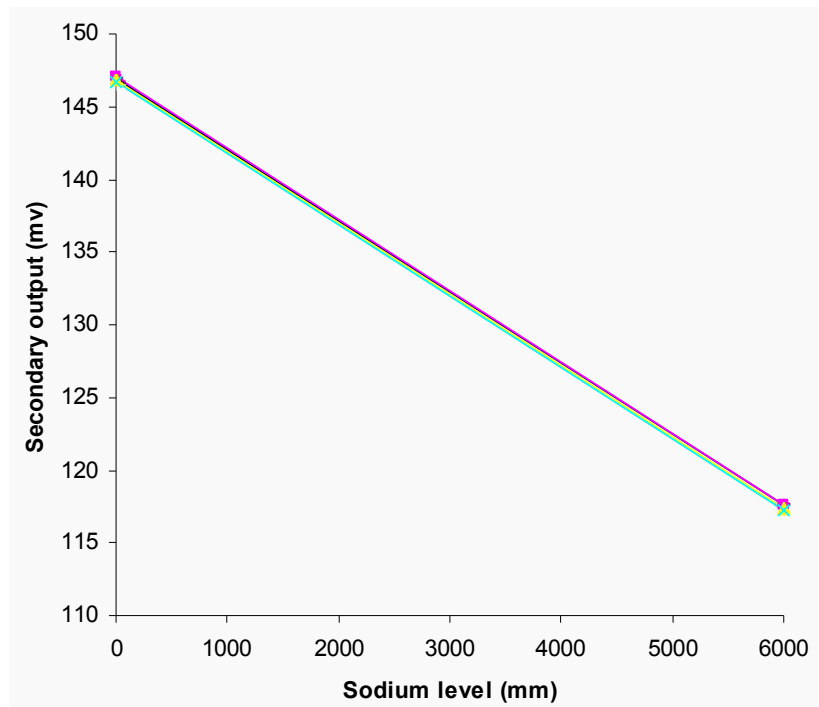


**Fig. 5.11 Secondary output with temperature compensation using external resistor**

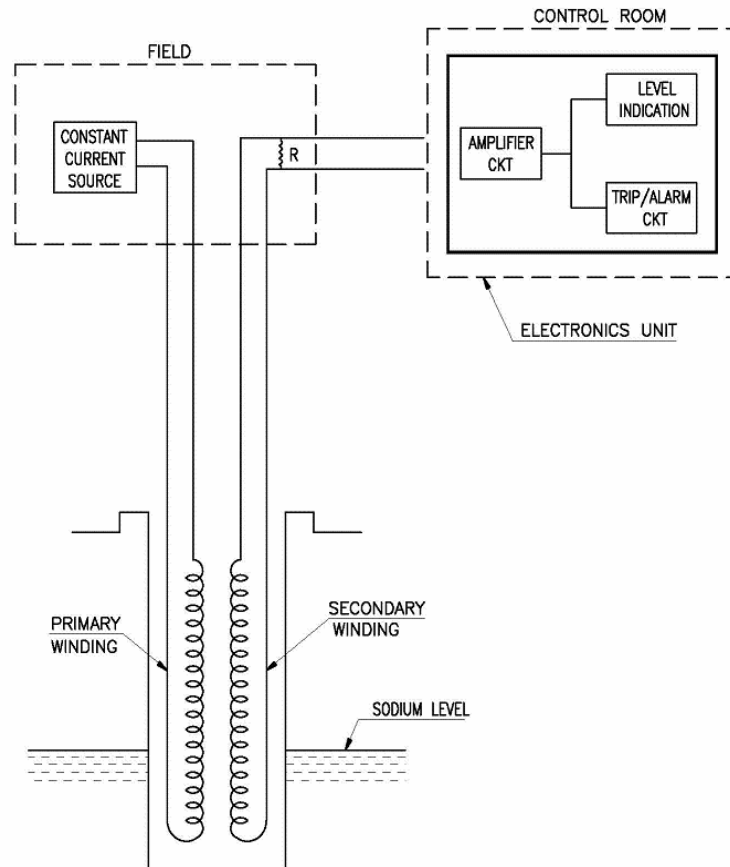


**Fig. 5.12 Level measuring system using new method of temperature compensation**

Figure 5.10 shows the secondary millivolt versus level without temperature compensation. The procedure used is for various sodium temperatures and at different levels the secondary millivolt is measured by quickly draining the sodium so as to maintain constant temperature along the level probe. This experiment is carried out to assess the linearity of the probe at various levels at a uniform temperature. After connecting the resistance across the secondary, the graph between actual level and secondary millivolt with temperature compensation is plotted as shown in Fig. 5.11. The same quick draining procedure for maintaining the uniform constant temperature throughout the pocket is followed to obtain the graph.

To simulate the actual condition, for constant sodium temperature, at various sodium levels, the secondary millivolt is measured after stabilization of cover gas and sodium temperature. In this case, secondary millivolt is found to be independent of temperature. The schematic of the level measuring system with new temperature compensation is shown in Fig. 5.12. Another interesting fact observed is at different temperature ranges, the value of resistance as well as frequency of operation also changes. Table-5.2 below shows the different temperature ranges and the value of external resistance to be added.

**Table-5.2 Variation of frequency and resistance at different temperature ranges**

Temperature range(°C)	Actual Value	
	Freq. (kHz)	Resistance ( $\Omega$ )
200-550	2.47	1535
250-550	2.54	1600
300-550	2.57	1640
350-550	2.57	1790
400-550	2.57	1980
450-550	2.47	2450
200-300	2.28	1290
200-400	2.42	1300

## 5.7 IMPROVED ELECTRONICS CHASSIS

The electronic chassis consists of two independent chains as shown in Fig. 5.13.

- an input chain
- an output chain.

The input chain feeds the primary winding of the probe with constant current and constant frequency. The output chain consists of receiver circuit. The isolated AC signal of secondary winding (5 mV to 250 mV) is processed by this circuit.

The exciter module has sinusoidal oscillator and a constant current drive circuit. The clock is derived from the crystal oscillator and using hardware based Direct Digital Synthesizer, the frequency of range 1 kHz to 10 kHz is selected with the resolution of 1 Hz.

As the signal level in the sensor is low of the order of few millivolts and the sensitivity is as low as 20%, a stringent requirement of sine wave of low distortion and amplitude stability is required in the electronics. The constant current source provides 0 to 200 mA rms isolated current, able to drive 150 Ohms with current stability better than  $\pm 0.05$  %. Isolation amplifier couple the sensor to both the energizing oscillator and the measuring unit to avoid earth loops and interfering pick up signals. As the resistor is connected across the secondary of the probe for providing temperature compensation, isolation amplifier with high input impedance is used to avoid the loading effect. The receiver module is having an active band pass filter in the range of 1 kHz to 5 kHz. In-situ test buttons shall be provided to increase / decrease the probe current at front to check the healthiness of the probe as well as the electronics. The receiver module has isolated input AC signal amplifier and isolated DC output. The following are the parameters of receiver:

Input signal range	: AC signal, 5 mV to 250 mV rms.
Input impedance	: $\geq 10^5$ ohms in the frequency band of 1 kHz to 5 kHz
Band width	: Lower 3 db point – less than 1 kHz Upper 3 db point – greater than 5 kHz
Stability	: 50ppm/°C for ambient variation of 10 to 50°C
Linearity	: better than $\pm 0.2\%$ of full scale
Output	: 0 – 10V DC, 10 mA, isolated.

Trim pots for Zero & Span indication is provided at the front. High and low set points are provided as trip contacts. The level reading is indicated in 1 mm resolution with 0.01% of reading.

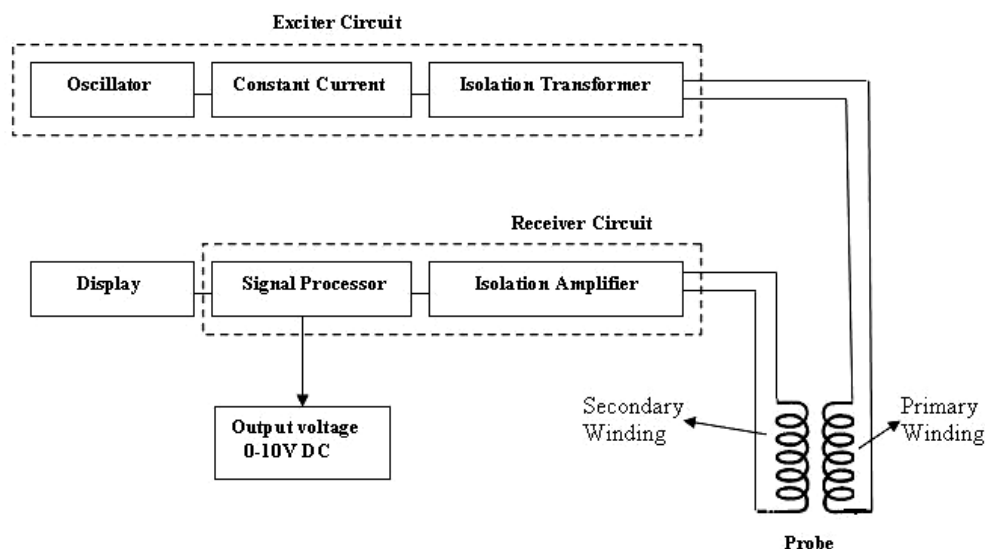


**Fig. 5.13 Improved electronics for continuous level probe**

## 5.8 STUDIES TO IMPROVE THE SENSITIVITY OF THE PROBE

The sensitivity of the level probe can be increased by increasing the number of turns of the windings per unit length or increasing the coil winding diameter. Two bobbins of varying diameters of 30 mm and 32 mm were fabricated and tested in sodium for obtaining the sensitivity using new temperature compensation technique. All the three bobbin diameters 28 mm, 30 mm and 32 mm are tested in sodium in the same pocket of dimension 42.6 mm OD/36 mm ID. As there is 10% variation in pocket dimensions are expected, to eliminate this effect, levels probes are tested in the same pocket one after the other. The secondary mill volt was measured at two extreme operating temperatures from 200 to 550°C. Using the proposed temperature compensation technique, the sensitivity of 3 different probes are found out. From the experimental result it is found that for 32 mm bobbin diameter probe, the sensitivity is 26.5 % which is much better than the 28 mm bobbin diameter probe. Table-5.4 shows the experimental results. Further, 32 mm diameter bobbin probe is easily insertable up to 10 m pocket.

**Table-5.3 Sensitivity studies for varying bobbin dimension**

<b>Particulars</b>	<b>28 mm bobbin size level probe</b>	<b>30 mm bobbin size level probe</b>	<b>32 mm bobbin size level probe</b>
Frequency in kHz	2.25	2.35	2.55
External resistance $R_{ext}$ in $\Omega$	214.6	161	154.46
Sensitivity in %	19.66	23.137	26.50
Radial gap	4.31	3.31	2.31
% Accuracy	0.4	0.8	0.9

### **5.9 DISCUSSION ON RESULTS**

The proposed temperature compensation technique has been validated experimentally for prototype MI type continuous level probe. The method of calculating external resistance with minimum sodium data is established. Using this method, the temperature effect on level is reduced from 10.59% to 1.5% over an extreme temperature without change in sensitivity of the probe. The sensitivity of the probe is around 20% which is sufficient enough to adjust in the electronics. The linearity of the probe is determined to be 0.7%. This technique not only improves the accuracy to 1.5% , but also simplifies the electronic circuitry by eliminating the temperature compensation circuitry. Another interesting fact to be observed is at different temperature ranges, the value of resistance as well as frequency of operation also changes. A comparison of performances of a partial compensation probe against the resistor compensated probe is presented in Table 5.5. It is found that when the new method of temperature compensation is applied to short length probe, the optimum frequency increased to 4.6 kHz with an accuracy of 0.6 %. Studies have been made to improve the sensitivity of long length probe by changing the bobbin diameter. The sensitivity improves from 26.5% to 20%.

**Table-5.4 Results of partial compensation and resistor compensation probe**

<b>Parameter</b>	<b>Partial compensation probe</b>	<b>External resistor compensation probe</b>
Bobbin size	28	28
Pocket	OD-34 mm/ ID-30mm	OD-42.6mm/ ID-36mm
Wall thickness of pocket	2 mm	2.7 mm
Radial gap between bobbin and pocket	1 mm	3 mm
Accuracy	3 %	1.5 %
Sensitivity	30 %	20 %
Active Length	2500 mm	9000 mm
Operating frequency	2.73 kHz	2.5 kHz

#### **5.10 MI TYPE DISCRETE LEVEL PROBE**

The MI type level sensor has certain advantages over the resistance-type level detector. The MI type sensor works on non-contact principle whereas the resistance type sensor works based on its contact with sodium. Besides, MI type is kept in a well or pocket, and so maintenance of the sensor becomes easy. Also, the level sensor is not required to be mounted in the vessel at the time of integrity test of the vessel after fabrication at the manufacturer's shop. Further, non-wetting of sodium with sensor does not affect the operation of MI type sensor. Considering the above advantages of MI type sensor, a prototype discrete level sensor was fabricated with 5 discrete levels (1000 mm active length and 1000mm non active length) and then tested in sodium. The bobbin diameter chosen for this application is 32 mm and located inside a pocket made of a standard pipe of (42.16 mm OD, 36.62 mm ID). The probe is tested in sodium and studies conducted on frequency response of probe.

### 5.11 CONSTRUCTION OF MI TYPE DISCRETE LEVEL PROBE

The sensing part of the probe consists of one primary winding and two layers of secondary windings as shown in Fig. 5.14. Bobbin is made of stainless steel former. The primary and secondary coils are wound at different positions where sensing is required. The primary winding of the bobbins are connected in series and secondary windings are individual as shown in Fig. 5.15. The primary and secondary windings are wound with 1 mm diameter mineral insulated cable with copper conductor. The probe is inserted in a stainless steel pocket. The primary is excited with a constant AC current at a fixed frequency. When the sodium surrounds the bobbin, induced signal in that bobbin secondary is minimal. When there is no sodium around the bobbin the induced signal in secondary is the maximum. The change in the induced signal of the secondary is utilized for sodium level detection. Since the

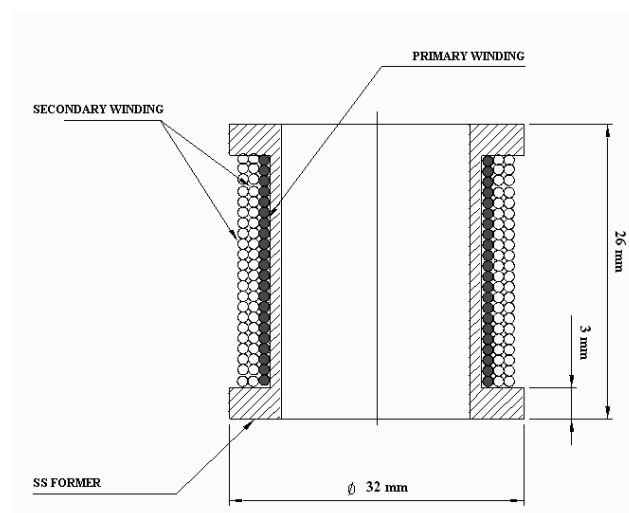


**Fig. 5.14 Bobbin and windings of MI discrete level probe**

coil lengths are much smaller ( $\sim 20\text{mm}$ ) compared to those used in the continuous type, the effect of sodium temperature coefficient on the level detection is negligible. For the same reason, the electronics is also made simpler.

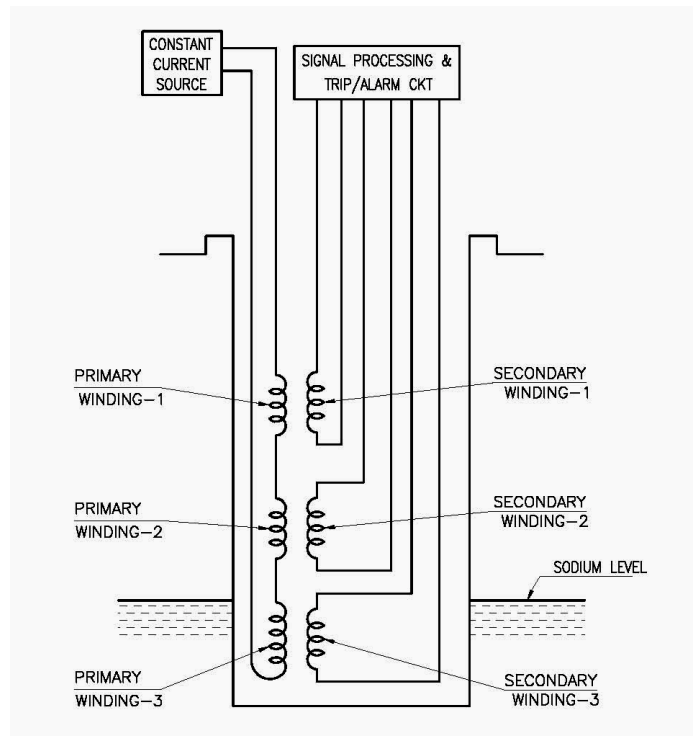


**Fig. 5.15 Schematic of MI discrete level sensor**

## **5.12 FREQUENCY RESPONSE STUDIES**

Experiment has been conducted by exciting the primary coil with an AC constant current of 100 mA. Initially frequency response studies are carried out in sodium by varying the frequency of the primary current from 2 kHz to 5 kHz in steps of 0.5 kHz and the results are recorded. A graph is plotted between % Sensitivity vs Frequency. The plot is shown in Fig. 5.16. From the graph it is found that at a frequency of 2.5 kHz, the percentage variation of secondary output is almost constant for different temperature values.

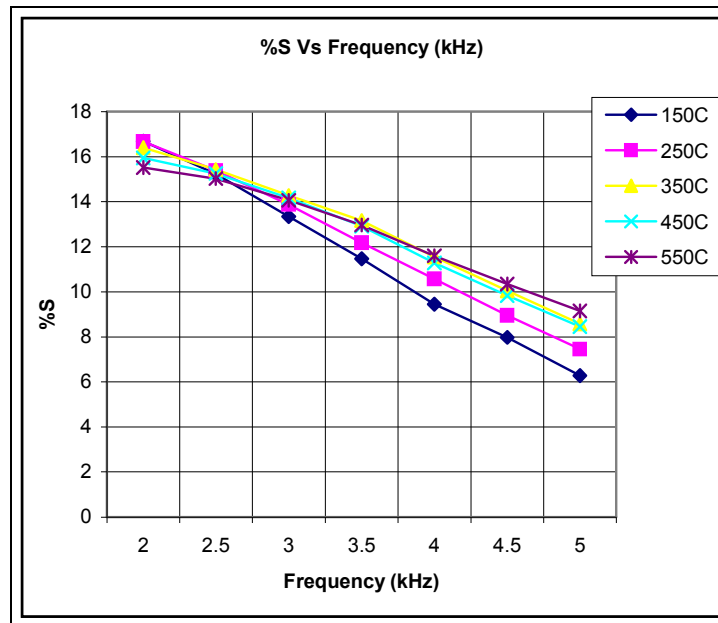


**Fig. 5.16 %Sensitivity Vs Frequency (kHz)**

### 5.13 DISCUSSION ON RESULT

From the experiments, it is found that due to temperature effect, the detection accuracy is around 6 mm from the centre of the bobbin. A value between minimum value of secondary output at bobbin immersed in sodium and maximum value of secondary output at bobbin in argon has been chosen as threshold value. Even though the threshold voltage is same for all the bobbins, each one triggers at different level due to sodium temperature variations as well as  $\pm 1$  turn variation in coil windings.

### 5.14 CLOSURE

As commercially available level sensors cannot be used in hostile sodium environment, these sensors and instrumentation are specially designed based on mutual inductance type. The present invention is directed to a level measuring probe which is easy to use, has improved accuracy of measurement and provides an indication of level which is almost independent of the temperature of the liquid in which the probe is immersed. For large power reactors, long length level probe of active length 6 m and non active length of 3.6

m has been developed and tested in sodium to assess the sensitivity. A new temperature compensation technique employing external resistor has also been developed. This technique reduces the temperature effect on level from 10.59 % to 1.5 % over a wide temperature range of 200°C to 550°C without change in sensitivity of the probe. Using this method, the optimum frequency of excitation and the external resistance to be connected across the secondary coil have been determined simultaneously. The sensitivity of the long length level probe is estimated as 20 % around the operating frequency with an accuracy of 1.5 %. This technique not only improves the accuracy but also simplifies the electronic circuitry by eliminating the temperature compensation circuit. The linearity of the probe was found to be 0.7 % at different temperatures.

Studies have also been carried out to improve the sensitivity of the probe by varying the coil diameter in the range of 28-32 mm. The sensitivity of 32mm diameter bobbin has improved to 26.5 %. The radial gap is sufficient enough for easy insertion and withdrawal of the probe into the pocket of length 10 m.

A prototype MI type discrete level probe with 5 levels have been fabricated with 32 mm diameter bobbin and tested for its performance in sodium at different temperature. The operating frequency is determined to be 2.5 kHz where the temperature effect on secondary millivolt is minimum. The discontinuous level detection accuracy is  $\pm 6$  mm around the centre of the bobbin.

After successful development of prototype MI type continuous and discrete level probes, 29 nos of Continuous and discrete level probes of each have been fabricated for use in PFBR. The active length of the continuous level probe varies from 660 mm to 9300 mm. These level probes were characterized in sodium for obtaining optimum frequency of operation and external temperature compensation resistor.

## **CHAPTER - 6**

## CONCLUSIONS

For a safe and reliable operation of sodium cooled fast reactors, on-line monitoring of core cooling and sodium levels in various systems are very essential. Further for safe fuel handling operation in opaque sodium at elevated temperature, ultrasonic under sodium viewing for protrusion detection is very essential. All these formed the focus of the research. Detailed experimental and theoretical studies have been carried out in these three domains. Major findings of the thesis work are summarized below.

### 6.1 IN-SITU TIME CONSTANT ESTIMATION OF CORE THERMOCOUPLES

Response time of thermocouple probe forms an important input for reactor safety analysis of fast reactors and hence frequent time constant estimation is essential. Towards this, a new time constant measurement method has been devised with minimal interference using ramp signal generated during operation of nuclear reactor. As part of this study, the following conclusions are derived

- The thermocouple in thermowell has been modeled and the characteristic graph between contact resistance Vs time constant has been established. The ramp rate in the reactor is estimated from fast response thermocouple which is used as reference. The response time of bare thermocouple is determined by matching the response curve.
- Process time constant for different flow zones are estimated by mathematical model and are subtracted from the predicted response time.
- This procedure has been applied to 36 thermocouple probes and the results are found within the expected limits.
- Validation and repeatability of the proposed method have been established by comparing reactor data set for two different instants.

### **6.1.1 Future Directions**

Degradation in response time due to creep, loss of spring pressure etc can be minimized (Carroll,1982) by fitting the thermowell with suitable alloy. With suitable material selection, and after studying the fabricability, galloy filled thermocouple can be tried out.

## **6.2 ULTRASONIC TECHNIQUE FOR PROTRUSION DETECTION**

Reactor core and mechanical components which make up the primary circuit coolant are totally immersed in sodium with the core being up to several meters below the sodium surface. Visual examination of the internal structure is impossible because of the opacity of sodium and lowering of liquid level is impractical once a reactor is operational. Under sodium ultrasonic method has been developed for detection and imaging of objects protruding above core top. The possible geometric shapes of the FBR objects /structures are not favorable for ultrasonic beam and imaging and detection of these structures with minimum axial gap is main challenge of the research. Full scale experiments have been performed in water properly simulating the beam spread half angle equivalent to that of sodium.

- Various absorber rod drive mechanism profiles have been simulated and different case studies have been carried out for different orientations. These experimental findings have been implemented in Indian FBR.
- It is found that the protrusion of absorber rods and their drive mechanisms can be detected and located except the extreme conical portion using direct imaging technique.
- All the reactor sectors have been simulated in both clockwise and anti-clockwise directions with and without retros for detecting protruded fuel subassembly or

conical shape of absorber rod drive mechanism which is not favorably oriented to the beam using an indirect imaging technique.

- Initially without any protrusion, the core is scanned and the C-scan image is constructed which served as the reference data. The gating is set based on reference data targeting blocking subassembly
- Using a summation algorithm with angle specific gating, it is established that a differential growth of 45 mm protrusion of fuel subassembly is detectable upto a distance of 3 m.
- The conical shapes of absorber rod drive mechanism of 20 mm projection from core cover plate are detectable using indirect imaging technique.
- The inclination effect of peripheral blocking subassembly is also studied and found that 0.44 deg. inclination is tolerable to ultrasonic beam.
- A single channel ultrasonic scanning system has been developed in house along with an offline analysis program for plotting the images with summation algorithm.

### **6.2.1 Future Directions**

Currently a rigid scanner is used in the reactor, during fuel handling operation which demands a long shut down time to scan the reactor core. Future development can be towards flexible system, capable of examining all the core from one loading position and able to remain permanently installed if ultrasonic imaging is a regular feature of FBR operation. The requirement is therefore for the development of transducers or ultrasonic waveguide capable of operating at 650°C and a flexible transducer manipulator.

The image presented is constructed from raw data which undergoes degradation due to beam spread and scanning pattern. Various algorithms can be experimented to remove beam divergence effect and filling of missing points. Current scanner has only 2 degrees of freedom. Three dimensional imaging is possible using mechanical and synthetic scanning

using 2 dimensional arrays. New methods for beam steering and focusing ultrasonic reflections arising from a specific spatial point on a target can be developed.

### **6.3 SODIUM LEVEL MEASUREMENT SYSTEM**

The under sodium scanner works only if the components are adequately immersed in sodium, which is ensured using sodium level measurement system. Long length online level measurement system has been developed and experimented in sodium for large power reactor applications. As the temperature gradient along the level probe is large an improved dynamic temperature compensation technique with simple electronics has been developed. The following results are obtained

- A Prototype longer level probe of 6000mm has been fabricated and tested in sodium to assess the sensitivity.
- Using the proposed method of temperature compensation, the temperature effect on level probe is reduced from 10.59 % to 1.5 % over a temperature range of 200°C to 550°C without change in sensitivity of the probe.
- The optimum frequency of excitation and the external resistance to be connected across the secondary coil have been arrived at simultaneously.
- The sensitivity of the level probe is determined to be 20 % at the operating frequency with an accuracy of 1.5 %. The linearity of the probe was found to be 0.7 % over the operating temperature range.
- This technique not only improves the accuracy but also simplifies the electronic circuitry by eliminating the temperature compensation circuit.
- Experimental studies have been carried out to improve the sensitivity of the probe by varying the coil diameter.
- A prototype MI type discrete level probe with 5 levels has been fabricated with 32mm diameter bobbin and tested for its performance in sodium at different temperatures.

- The discontinuous level detection accuracy is about  $\pm 6$  mm around the centre of the bobbin. The same former can carry upto 5 sensors in one discrete level probe.
- After successful development of prototype MI type continuous and discrete level probes, 29 numbers of continuous and discrete level probes of each are fabricated for deployment in PFBR. The active length of the continuous level probe varies from 660 mm to 9300 mm.

### **6.3.1 Future Directions**

All the level probes require sodium calibration to arrive at optimum frequency, secondary millivolt levels and external temperature compensation resistor. Further studies can be carried out to dispense sodium calibration by choosing materials having same conductivity and permeability equivalent to that of stainless steel and sodium at 200 and 550°C. Improving the sensitivity of the sensor by changing the electrical windings of the primary and secondary coil can be studied. Further ultrasonic waveguide technique can be experimented for sodium level measurement.

## **ANNEXURE-1**

# EFFECT OF GROSS FLOW REDUCTION ON THE MAXIMUM RATED SUBASSEMBLY DUE TO THE PRESENCE OF GROSS BLOCKAGE

## A1.1 ANALYSIS

Partial inlet flow blockage in a single fuel SA has been analyzed with rate of SA flow reduction and extent of flow reduction as independent parameters. Then an assessment is made to check whether the  $\delta\theta_1$  SCRAM parameter could limit the maximum clad hotspot below 800°C. The detailed calculations are shown in Annexure-I. SA is designed for a flow of 35.83 Kg / s during normal operation such that the clad mid-wall hotspot temperature of the fuel pin does not exceed 973 K (700° C). For limiting the hotspot clad mid-wall temperature to 1073 K (800° C) the required flow rate is 25.88 Kg/s translation in to a flow reduction of 27.8 % for respecting the clad mid- wall temperature limit of 1073 K for category II event .

$$T_{cladmid-wallhot} = T_{IN} + \Delta T_{channel} * f_{ch} + \Delta T_{film} * f_{fi} + \Delta T_{clad-mid} * f_{cl} \quad (A1.1)$$

$f_{ch}$  - channel hotspot factor

$f_{cl}$  - clad hotspot factor

$f_{fi}$  - Film hotspot factor

Let  $P$  be the power generated in a maximum rated SA . Power ( $P$ ) =  $mC_p\Delta T$

$P$  is the power generated in the central subassembly SA

The temperature rise across the SA is given by

$$\Delta T_{SA} = \frac{P}{M * C_p} \quad (A1.2)$$

$$P = 8.1 \times 10^6 \text{ W}$$

$$C_p = 1267 \text{ J/kg/K}$$

$$m = \text{mass flow rate of sodium thro' SA} \\ = 35.83 \text{ Kg/sec}$$

$$\Delta T = T_{SA \text{ O/L}} - T_{in}$$

$$T_{in} = 397^\circ\text{C}$$

$$T_{SA} = 580^\circ\text{C}$$

Calculation of maximum rated channel Temperature

$$\Delta T_{ch} = \beta \Delta T_{SA} \tag{A1.3}$$

$$\beta = 1.2$$

$$\Delta T_{ch} = 1.2 \times (580 - 397)$$

$$\Delta T_{ch} = 219.6^\circ\text{C}$$

$$\Delta T_{film} = \frac{\text{Linear power } \chi}{\pi * d * \text{heat transfer coe. of Na}}$$

$$\text{Linear power } \chi = 450 \text{ W/cm}$$

$$\text{Dia of clad} = 6.6 \text{ mm}$$

$$\Delta T_{film} = \frac{450}{\pi * 0.66 * 12}$$

$$\Delta T_{film} = 18^\circ\text{C}$$

$$\text{Actual at the Top of SA} = 18 * 0.52 = 9^\circ\text{C}$$

$$f_{ch} = 1.1504$$

$$f_{film} = 2.3088$$

$$f_{clad} = 1.4014$$

$$\Delta T_{clad-mid} = \frac{(0.5 * \chi)}{(2\pi K_c)} * \ln \frac{d_o}{d_i} \tag{A1.4}$$

$d_o$  = clad OD

$d_i$  = clad ID

$$\begin{aligned}\Delta T_{clad-mid} &= \frac{(0.5 * \chi)}{(2\pi K_c)} * \ln \frac{d_o}{d_i} \\ &= \frac{(0.5 * 450)}{(2\pi * 0.21)} * \ln \frac{6.6}{5.7} \\ &= 170.52 * 0.1466 * 0.52\end{aligned}$$

$$\Delta T_{clad-mid} = 13^\circ\text{C}$$

Clad mid wall hot spot temperature is estimated by

$$\Delta T_{clad-mid-wall-hotspot} = T_{in} + \Delta T_{channel} * f_{ch} + \Delta T_{film} + \Delta T_{clad-mid} * f_{cl} \quad (\text{A1.5})$$

$$\begin{aligned}\Delta T_{hotspot} &= 397 + 219.6 * 1.15 + 9 * 2.308 + 13 * 1.4014 \\ &= 397 + 252.54 + 20.77 + 18\end{aligned}$$

$$\Delta T_{hotspot} = 688.31^\circ\text{C}$$

$$\begin{aligned}\Delta T_{clad-mid-nominal} &= T_{in} + \Delta T_{channel} + \Delta T_{film} + \Delta T_{clad-mid} \\ &= 397 + 219.6 + 9 + 13 = \mathbf{638.6} \text{ }^\circ\text{C}\end{aligned} \quad (\text{A1.6})$$

At 25.88 kg/sec

$$\Delta T_{SA} = \frac{P}{M * C_p}$$

$$8.1 * 10^6 = 25.88 * 1267 (397 - T_2)$$

$$T_{SA} = 644 \text{ }^\circ\text{C}$$

$$\Delta T_{clad-mid-wall-hot} = T_{in} + T_{channel} * f_{ch} + \Delta T_{film} + \Delta T_{clad-mid} * f_{cl} \quad (\text{A1.7})$$

$$\Delta T_{ch} = \beta * \Delta T = 1.2 * 644 - 397 * 1.15$$

$$T_{clad hot spot} = 397 + 296.4 * 1.15 + 9 * 2.3 + 13 * 1.4$$

$$T_{clad\ hot\ spot} = 777^{\circ}\text{C}$$

$$\begin{aligned} \Delta T_{clad-mid-nominal} &= T_{in} + \Delta T_{channel} + \Delta T_{film} + \Delta T_{clad-mid} \\ &= 397 + 296.4 + 9 + 13 \\ &= 715^{\circ}\text{C} \end{aligned} \tag{A1.8}$$

$$\begin{aligned} \text{Maximum allowable blockage} &= 1 - (25.88/35.83) \\ &= 27.77\% = 27.8\% \end{aligned}$$

Assume rate of blockage is 3.6% and find out total time

$$\text{Rate of flow reduction} = \text{extent of flow reduction} / \text{Total time}(t)$$

Assume computer process time (CST) = 1 sec

Actuation time of control rod (SDM) = 1 sec

Total time required to SCRAM = Thermocouple response time + CST + SDM

$$t = \theta + 2$$

$$\theta = (27.8/3.6) - 2$$

$$\theta = 5.72 \text{ sec}$$

$$T_e = T_{in} + R * t \tag{A1.9}$$

$$650 = 580 + R * 7.72$$

$$R = 9.0673^{\circ}\text{C/sec}$$

$$T_m - T_{in} = Rt + R\tau(e^{-t/\tau} - 1) \tag{A1.10}$$

**Table A1.1 Flow rate versus clad hot spot temperature**

<b>Particulars</b>	<b>Flowrate kg/s</b>	<b>Nominal Sodium outlet temperature (°C)</b>	<b>Nominal Clad temperature (°C)</b>	<b>Clad hot spot temperature (°C)</b>
<b>Normal operation</b>	35.83	580	639	688
<b>Minimum flow to avoid Design Safety Limit</b>	25.88	644	715	777

### **A1.2 MODEL**

As the blockage sets in, the flow starts reducing and the temperature across SA rises. Thermocouple which is above the SA outlet, senses the temperature rise after a small time lag, which is due to time constant of the thermocouple. The thermocouple in thermo well is considered as first order system and response time for ramp input was derived. This type of input is a characteristic of thermal analysis systems where linear temperature rise with respect to time is quite common. The detailed formula derivation is given below. The general solution is given by

$$G(s) = \frac{R}{s^2(1+\tau s)} \quad (\text{A1.11})$$

Splitting into partial fraction

$$\frac{R}{s^2(1+\tau s)} = \frac{As+B}{s^2} + \frac{C}{\tau s+1}$$

$$\frac{1}{s^2 + (\tau s + 1)} = \frac{(As+B)(\tau s + 1) + Cs^2}{s^2(\tau s + 1)}$$

equating the coe. of  $s^2$

$$A\tau + c = 0$$

equating the coe. of  $s$

$$A + B\tau = 0$$

$$A = -\tau$$

$$B = 1$$

$$C = \tau^2$$

$$\frac{1}{s^2 + (\tau s + 1)} = \frac{-\tau s + 1}{s^2} + \frac{\tau^2}{\tau s + 1}$$

$$G(s) = R \left[ \frac{-\tau}{s} + \frac{1}{s^2} + \frac{\tau^2}{\tau s + 1} \right]$$

Taking Laplace transform

$$G(s) = R \left[ t - \tau \left( \frac{1}{s} - \frac{\tau}{\tau s + 1} \right) \right]$$

$$= R \left[ t - \tau \left( \frac{1}{s} - \frac{\frac{\tau}{\tau}}{\frac{\tau s}{\tau} + \frac{1}{\tau}} \right) \right]$$

$$= R \left[ t - \tau \left( \frac{1}{s} - \frac{1}{s + \frac{1}{\tau}} \right) \right]$$

$$= R \left[ t - \tau \left( \frac{s + \frac{1}{\tau} - s}{s \left( s + \frac{1}{\tau} \right)} \right) \right]$$

$$= R \left[ t - \tau \left( \frac{\frac{1}{\tau}}{s \left( s + \frac{1}{\tau} \right)} \right) \right]$$

$$\text{Since } L^{-1} \frac{a}{s(s+a)} = 1 - e^{-at} \quad (\text{A1.12})$$

$$G(t) = R \left[ t - \tau (1 - e^{-t/\tau}) \right]$$

$$T_m - T_i = Rt - R\tau(1 - e^{-t/\tau})$$

$$T_m = T_i + Rt - R\tau(1 - e^{-t/\tau})$$

$$T_m = T_e - R\tau(1 - e^{-t/\tau})$$

$$(\text{A1.14})$$

$$T_e = T_i + Rt$$

Where

$T_m$  - Thermocouple temperature ( $^{\circ}\text{C}$ )

$T_e$  --- SA outlet temperature ( $^{\circ}\text{C}$ )

$\tau$  --- Time constant of thermocouple (s)

$R$  ---- Rate of change of temperature ( $^{\circ}\text{C/s}$ )

$t$  ---- time (s)

$T_i$  ---- SA outlet temperature at  $t=0$

SA outlet temperature under normal operation corresponding to clad mid-wall temperature limit of  $700^{\circ}\text{C}$  increases from  $580^{\circ}\text{C}$  to  $650^{\circ}\text{C}$  under category II condition. For a particular case, when perturbation is @  $9.05\text{ K/s}$ , responses of various temperatures like coolant outlet, response of TC with different time constants ( $\tau$ ) and clad mid-wall temperature under hot

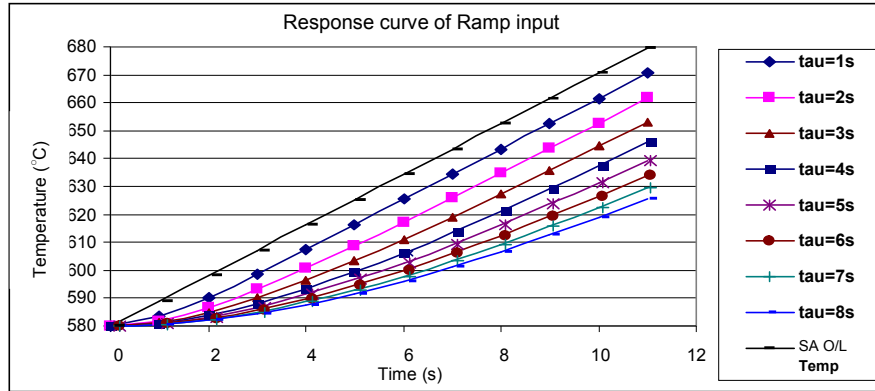


Fig. A1.1 Measured temperature as a function of response time for ramp input

Table-A1.2 Thermocouple reading for different time constant

for ramp input ( $R=9.0673$  K/s)

Time (s)	Thermocouple reading for different $\tau$ in sec								SA exit Temperature ( $^{\circ}$ C)
	$\tau = 1$	$\tau = 2$	$\tau = 3$	$\tau = 4$	$\tau = 5$	$\tau = 6$	$\tau = 7$	$\tau = 8$	
0	580	580	580	580	580	580	580	580	580
1	583.34	581.93	581.36	581.04	580.85	580.72	580.62	580.54	589.05
2	590.29	586.67	584.90	583.86	583.19	582.71	582.36	582.09	598.1
3	598.59	593.11	590.01	588.07	586.75	585.80	585.08	584.52	607.15
4	607.37	600.59	596.24	593.34	591.30	589.80	588.64	587.73	616.2
5	616.33	608.69	603.27	599.46	596.68	594.58	592.94	591.63	625.25
6	625.36	617.17	610.88	606.23	602.72	600.01	597.87	596.13	634.3
7	634.41	625.88	618.91	613.50	609.31	606.01	603.35	601.17	643.35
8	643.47	634.74	627.23	621.18	616.36	612.48	609.31	606.69	652.4
9	652.54	643.67	635.76	629.16	623.76	619.34	615.68	612.62	661.45
10	661.61	652.66	644.44	637.38	631.47	626.54	622.41	618.92	670.5

spot conditions were estimated. SCRAM threshold limit is taken as + 10 K on the SA outlet temperature. At  $t=1$ , find  $T_m$ (keeping  $R = \text{fixed}$ ,  $\tau=1$  fixed,  $T_{in} = \text{fixed}$ ) and plot the graph. The response to ramp input was plotted for various time constant varying from 1 to 8 s as shown in Fig. 1.4. The steady state error increases as time constant increases. It is observed that it takes 4.6 s for TC with  $\tau = 8$  s to reach the threshold limit of  $590^{\circ}$  C. Taking into

account Computer Scan Time (CST) maximum of 1 s and Shut Down Margin (SDM) of 1 s, total time taken for SCRAM to be achieved would be 6.6 s (Table 1.5). By then clad hotspot temperature would have reached 785°C which is less than the limit of 800 °C. This indicates that a good margin is available for clad mid-wall temperature limit. The time taken by TC with lesser  $\tau$  for reaching SCRAM threshold limit is 4 & 3.4 s respectively for  $\tau = 6$  & 4 s. With lesser  $\tau$ , a lower mid-wall temperature under hotspot condition was reached by clad also. Even for SCARM threshold limit of 15 K, with  $\tau = 8$  s, time required for TC to sense the threshold limit is 5.7s. Taking in to account the CST of 1 s and SDM of 1s, the total time taken to SCRAM the reactor is 7.7 s, which is just adequate to satisfy the clad mid-wall temperature limit under hot spot condition. Flow reduction rate is estimated from the maximum allowable blockage and the time required to SCRAM the reactor. Flow reduction rate=Maximum allowable blockage/Total time required to SCRAM

Where, Total time required to SCRAM= TC response time for a given  $\tau$ +CST+SDM

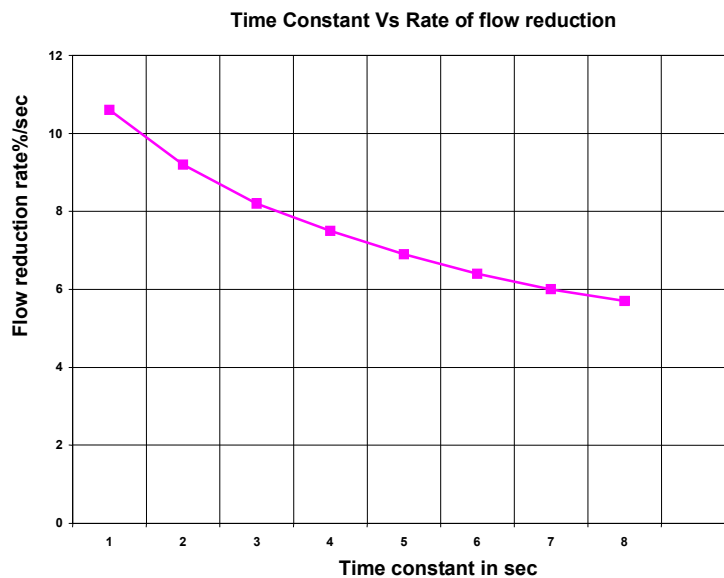


**Fig. A1.2 Time constant Vs rate of flow reduction**

Fig.A1.2 represents the flow reduction rate, Thermocouple constant,  $\tau$ , and for SCRAM threshold limits of 10K for a constant CST & SDM of 1 s each. As  $\tau$  decreases allowable blockage rate increases. From the data it appears that there is a steep gradient upto 2 s and it saturates beyond 6 s. With the fast response thermocouples ( $\tau < 2$  s), temperature fluctuation would lead to frequent SCRAM.

### **A1.3 CLOSURE**

Studies indicate that the rate of growth of blockage is slow which can easily be detected with the thermocouples having  $\tau = 6$  s and there is no much advantage in having a lower  $\tau < 6$  s. Hence, a thermocouple time constant,  $\tau = 6 \pm 2$  s is adequate from the clad mid-wall temperature requirements for a SCRAM threshold temperature limit of + 10 K.

## **ANNEXURE - 2**

## ERROR ESTIMATION IN TIME CONSTANT

### ERROR CALCULATION FOR TIME CONSTANT OF THERMOCOUPLE PROBE ALONG WITH PROCESS DELAY

Error in scan interval	= 0.001s
Rate	= 3.74 °C/s
Time	= 6 s
$\Delta t$	= 0.001 s
$\tau$	= 5.6 s
$T_{ss(004X)}$	= 432.669 °C
$T_{SA(004X)}$	= 425.348 °C
$T_{ss-inlet}$	= 339.55 °C
$T_{inlet(t2)}$	= 339.78°C
$T_{CSA-ss}$	= 426.829 °C
$T_{csA (t2)}$	= 409.233°C

#### Error in temperature

Measurement = 0.4% of temperature reading

#### Formulas used

$$R = \frac{[T_{CSA}(t_1) - (T_{in}(t_1))] - [T_{CSA}(t_2) - (T_{in}(t_2))]}{(t_1 - t_2)} \quad \dots\dots\dots(A2.1)$$

$$T_m = T_{SA(m)}(t) - T_{in}(t) \quad \dots\dots\dots(A2.2)$$

$$T_{ss} = T_{SA}(ss) - T_{in} \quad \dots\dots\dots(A2.3)$$

$$T_m = (T_{ss} - Rt) + R\tau(1 - e^{-t/\tau}) \quad \dots\dots\dots(A2.4)$$

The thermocouple reading consists of both random and systematic error. If the error is purely random in nature, then, traditional statistical error estimation method will be followed. Since

thermocouples used in the present application have significant systematic error contribution the following methodology has been adopted. The error was calculated by finding out the minimum and maximum possible values of the function by including the incremental/ decrease in the deviation. The error lies in between the maximum and the minimum value of the function taking into account the deviation.

To find out error in R

$$R = \frac{[T_{CSA}(t_1) - (T_{in}(t_1))] - [T_{CSA}(t_2) - (T_{in}(t_2))]}{(t_1 - t_2)}$$

Two thermocouples such as central SA thermocouple and reactor inlet temperature measuring thermocouple are used for ramp calculation. The error in a thermocouple, if any, will be systematic in nature as the thermocouple having positive error will show positive error at another instant of shorter time interval. A typical estimate of error at a particular instant of time is shown in Table-A2.1. The required data are taken from Fig. 3.11.

**Table A2.1 Typical calculation for error in Rate**

Parameter	Fitted value	++ error	-/-error	+/- error	-/+ error
T <sub>csa</sub> (t <sub>1</sub> )	419.201	420.9	417.5	420.9	417.5
T <sub>in</sub> (t <sub>1</sub> )	339.78	341.1	338.4	338.4	341.1
T <sub>csa</sub> (t <sub>2</sub> )	407.759	409.4	406.1	409.4	406.1
T <sub>in</sub> (t <sub>2</sub> )	339.55	340.9	338.2	338.2	340.9
ΔT	3 sec	3.001	2.999	3.001	3.001
Rate	3.74	3.75	3.72	3.75	3.72
%error	----	<b>0.36</b>	<b>0.36</b>	<b>0.38</b>	<b>0.45</b>

$$\% \text{ error} = \left| \frac{\text{Approximate value} - \text{Exact value}}{\text{Exact value}} \right| \times 100$$

Various errors are estimated as shown in the above calculation and are listed in Table-A2.2.

**Table-A2.2 Error estimation in rate, Tss and Tm**

Condition	Error in Rate	Error in Tss	Error in Tm
Nominal	---	---	----
Positive	0.36%	-----	0.4%
Tcsa/Tsa positive T <sub>in</sub> negative	0.38%	3.31%	3.6%
negative	0.36%	0.4%	0.4%
Tcsa/Tsa Negative T <sub>in</sub> positive	0.45%	---	3.6%
<b>Max error</b>	<b>0.45%</b>	<b>3.3%</b>	<b>3.6%</b>

After finding out the maximum errors in the rate, Tss and Tm the positive and negative deviations are substituted in equation (A2.4) and corresponding to the nominal value, the errors in time constants ( $\tau_{TC+Process}$  &  $\tau_{Process\ alone}$ ) are estimated and are given in Table- A2.3.

As observed from Table-A2.3, the maximum error obtained in time constant of a thermocouple with process is found to be 3.08%.

**Table-A2.3 Error estimation in time constant of thermocouple with process**

Condition	Rate	Tss (°C)	Tm (°C)	t (s)	tau (s)	error in $\tau_{TC+Process}$
Nominal	3.74	93.11	84.36	6	5.52	---
Positive	3.76	96.37	87.39	6.003	5.37	<b>2.72%</b>
Negative	3.72	89.86	81.32	5.997	5.69	<b>3.08%</b>

## ERROR CALCULATION IN PROCESS TIME CONSTANT

Error in scan interval = 0.001s

Rate = 3.74 °C/s

Time = 6 s

$\Delta t$  = 0.001 s

$\tau$  = 0.77 s

$T_{ss(80mm)}$  = 426.829 °C

$T_{SA(80mm)}$  = 407.33 °C

$T_{ss-inlet}$  = 339.55 °C

$T_{inlet(t2)}$  = 339.78 °C

$T_{CSA-ss}$  = 426.829 °C

$T_{csA(t2)}$  = 409.233 °C

Error in temperature

Measurement = 0.35 % of temperature reading

### Formulas used

$$R = \frac{[T_{CSA}(t_1) - (T_{in}(t_1))] - [T_{CSA}(t_2) - (T_{in}(t_2))]}{(t_1 - t_2)} \quad \dots\dots\dots(A2.6)$$

$$T_m = T_{SA(m)}(t) - T_{in}(t) \quad \dots\dots\dots(A2.7)$$

$$T_{ss} = T_{SA}(ss) - T_{in} \quad \dots\dots\dots(A2.8)$$

$$T_m = (T_{ss} - Rt) + R\tau(1 - e^{-t/\tau}) \quad \dots\dots\dots(A2.9)$$

**For calculation of rate, process response curve for Zone-1 as shown in Fig. 3.13 is used.**

**The same procedure as in Table-A2.1 is followed in Table-A2.4.**

**Table-A2.4 Error Estimation in Rate, Tm and Tss for process**

<b>Condition</b>	<b>Error in Rate</b>	<b>Error in Tss</b>	<b>Error in Tm</b>
Nominal	---	---	----
All Positive error	0.31%	-----	0.4 %
T <sub>csa</sub> /T <sub>sa</sub> positive T <sub>in</sub> negative	0.338 %	3.07 %	3.9 %
All negative error	0.316 %	0.35 %	0.4 %
T <sub>csa</sub> /T <sub>sa</sub> Negative T <sub>in</sub> positive	0.405 %	---	3.91 %
<b>Max error</b>	<b>0.41 %</b>	<b>3.1%</b>	<b>4 %</b>

**Table-A2.5 Error Estimate in process time constant**

<b>Condition</b>	<b>Rate</b>	<b>Tss</b>	<b>Tm</b>	<b>t in sec</b>	<b>tau</b>	<b>error in <math>\tau_{\text{Process alone}}</math></b>
Nominal	3.74	87.27	67.35	6	0.7	---
All parameters with positive deviations	3.757	89.98	69.98	6.003	0.679	<b>3.0 %</b>
All parameters with negative deviations	3.72	84.57	64.72	5.997	0.671	<b>4.14 %</b>

The error in the time constant of process due to structural materials and sodium alone is 4.14% as shown in Table-A2.5. Thus, the error in the time constant of thermocouple is obtained by subtracting the time constant of process alone from the time constant of thermocouple with process. Table-A2.6 depicts the error estimation in the thermocouple time constant.

**Table-A2.6 Error estimation in thermocouple time constant**

<b>Condition</b>	$\tau_{TC}$	<b>Error in thermocouple time constant</b>
Nominal	4.82	
Positive	4.681	<b>2.88 %</b>
negative	5.019	<b>4.12 %</b>

**Error in thermocouple time constant = 4.12 %**

## REFERENCES

- Argous, J.P.**, et al., 1980. Temperature measurement at the LMFBR core outlet, (American Nuclear Society), pp. 4.52-4.58.
- Barrett, L.M.**, Mcknight, J.A., Fothergil, J.R. 1984. Ultrasonic viewing in Fast Reactors, Phys. Technology, **15**, pp. 308-314.
- Bertini, H.W.**, et al., 1980. Description of selected accidents that have occurred at nuclear facilities, Report: ORNL/NSIC-176, Oak Ridge National Laboratory, Oak Ridge, Tennessee.
- Bishop, J.F.W.**, 1981. Power from Plutonium: fast reactor fuel, Nucl. Energy, **20**, pp. 31-48.
- Bishop, J.** British Patent Nos 1526950 and 2029306.
- Brear, D.J.**, Stansfield, R.G., 1991. An analysis of the events lead up to and during the oil ingress into primary circuit on 24-29 July, Report: AEA RS 5230.
- Brockmann, K.**, et al., 1990. Temperature drift at outlet temperature of KNK II subassemblies, Int. Fast Reactor Safety Meeting, Snowbard, Utah.
- Burch, S.**, McKnight, J.A., 1982. The application of maximum entropy to the processing of ultrasonic images of nuclear reactor components immersed in liquid sodium, Acoustical imaging, **12**, pp. 249-57.
- Carroll, R.M.**, Carr, K.R., Shephard, R.L., 1982. Studies of sheathed thermocouple construction and installation in thermowells to obtain faster response, Temperature-Its measurement and control in Science and Industry, **5**, Part-II, American Institute of Physics, Tennessee.
- Chetal, S.C.**, Balasubramanian, V., Chellapandi, P., Mohanakrishnan, P., Puthiyavinayagam, P., Pillai, C.P., Raghupathy, S., Shanmugham, T.K., Sivathanu Pillai, C., 2006. The design of the Prototype Fast Breeder Reactor, Nuclear Engineering Design, **236**, pp. 852–860.

- Coon, G.A.**, Rochester, N.Y. 1957. Responses of temperature sensing element analogs, Trans. ASME, **56 (A-51)** pp. 1857-1868.
- Creys-Malville**. 1982. SA accident analysis, Proceedings of Int. tropical meeting on LMFBR safety and reliable design, Lyon, France.
- Da Silva, J.J.**, Wanzeller, M.G., Almeida Farias, P. De., Da Rocha Neto, J.S. 2005. Development of circuits for excitation and reception in ultrasonic transducers for generation of guided waves in hollow cylinders for fouling detection, Proc. IEEE Instrumentation and Measurement Technology Conference, **1**, pp. 467-471.
- Data Book** on Heat Transfer Division Sec., 502.5 , page 9, May 1991.
- Davidson, D.F.**, Duncombe, E. 1966. Some transducer Techniques for use at elevated temperatures, Trans Soc., Instrument. Tech. **18**, pp. 51-61.
- Day, C.K.**, Smith, R.W., 1974. Under sodium viewing IEEE Trans. Ultrasonics, US-21(3).
- Duncombe, E.**, et al., 1966. Some Analytical and process instrumentation for measurements in sodium Proc., IAEA Symposium on Alkali Metal coolants paper SM 85/16, Vienna.
- Duncombe, E.** 1984. Some Instrumental techniques for hostile environments, Journal of Phys. E: Sci. Instrumentation, **17**, pp. 7-18.
- Evans, P.B.F.**, et al., 1966. Control and Instrumentation of Prototype Fast Reactor. Proc. BNES conference on fast breeder reactors, Paper No. 5A/S, London.
- Fothergill, J.R.**, et al., 1980. Ultrasonic imaging in LMFBRs using digital techniques, Report No. ND-R-581(R), pp. 1-7.
- Gillespie, A.B.**, Deighton, M.O., Pike, R.B., Watkins. 1982. A new ultrasonic technique for the measurement of liquid level, Ultrasonics, pp.13-17.
- Gourdon, J.**, et al., 1979. The detection anomalies in Fast Reactor Cores, RAPPORT TECHNIQUE DRNP/P/No. 11, Fast Reactor Safety Technology, Seattle, USA.

- Griffin, J.W., et al., 2009.** Under-Sodium Viewing: A review of Ultrasonic Imaging Technology for Liquid Metal Fast Reactors, Pacific Northwest National Laboratory PNNL-18292, USA.
- Hans, R., Kranz, E., Weiss, H., 1984.** Under-sodium viewing - A method to identify objects in an opaque medium, Proc. Liquid Metal Engg. Technology, BNES, London, pp. 419-421.
- Hashemian, H.M., 2005.** Sensors Performance and reliability, ISA Publication. North Carolina, USA.
- Hirokazu Karasawa et al., 2000.** Development of under-sodium three dimensional Visual Inspection Technique using Matrix- arrayed Ultrasonic Transducer, Journal of Nuclear Science and Technology, **37**, No.9, pp. 769-779.
- Hoitnik, N.C., Day, C.K., 1975.** Under-sodium viewing system development for FFTF, HEDL-TME, Jan., pp. 21-25.
- Huang, J., Que, P.W., Jin, J.H., 2004.** A Parametric Study of Beam Steering for Ultrasonic Linear Phased Array Transducer, Russian Journal of Nondestructive Testing, **40**(4), pp. 254-259.
- Iraci M.P.G., et al., 2007.** Time response measurement of Angra I Nuclear Power Plant using direct and Indirect Methodologies, Proc. Int. Nuclear Atlantic Conf. - INAC, Santos, SP., Brazil.
- Jha, D.K., 2005,** Text book of Electrostatics, Discovery Publishing House.
- Junzo, T., et al., 1980.** An ultrasonic viewing system in liquid sodium, IEEE Trans. Nucl. Sci. **NS-27**, No 1, pp. 821-825.
- Karasawa, K., Izumi, M., Suzuki, T., Nagai, S., Tamura, M., Fujimori, S. 2000.** Development of Under-sodium Three-dimensional Visual Inspection Technique Using Matrix-arrayed Ultrasonic Transducer, J. Nucl. Sci. Tech. **37**(9), pp. 769-779.

- Kerwin, C.**, Playfoot William, H. Todt., 1976. Liquid metal level sensor with increased sensitivity 1976, Patent No.: US3996801A.
- Kuniji Asano.** 1975. A mathematical model of an inductive type sodium level meter and some applications, IEEE Transactions on Nuclear Science, **NS-22**, No.6, pp. 2689-2695.
- Lions, N.**, Buis, H., Baron, J., Fournier, C., Gourdon, J. 1974. Special Instrumentation for PHENIX, Proc. Int. Conf. on Liquid Metal Technology In Energy Production, CEN Cadarache, France.
- Lyons N.**, et al., 1978. Utilisation and performance of sodium instrumentation during start up and initial operation of Phenix, Proc. Int. Conf. on Liquid Metal Technology in Energy Production, Pennsylvania.
- McGonigal, F.**, Dean, S.A., Ferguson, B.G., Harrison, E. 1971. Measurement of sodium level in PFR, Nucl. Engg. International, **16**, No. 175/6, pp. 62-65.
- McCabe, W.L.**, Smith, J.C., 1976. Unit operations of Chemical Engineering, 3<sup>rd</sup> Edition, McGraw-Hill Chemical Engineering Series, pp. 275-277.
- Mcknight, J.A.**, Burton, E.J. 1983. Under sodium viewer, Atom, **323**, pp. 266-270.
- Nestor, C.W.**, Dodd, C.V., Deeds, W.E., 1979. Analysis and computer programs for eddy current coils Concentric with multiple cylindrical conductors, Report: ORNL 5220, Tennessee.
- Paris et al.**, 1976. Probe for measuring the level of a liquid, United States Patent No.: 3.948.100.
- Prahlad, B.**, Swaminathan, K.,. Determination of response time of core thermocouples of the Fast Breeder Test Reactor, Proc. 6<sup>th</sup> Natl Heat and Mass Transfer Conf., IIT-Madras, India..

- Pro-Wave.** 2005. Selection and Use of Ultrasonic Ceramic Transducers. Application Note AP050830. Pro-Wave Electronics Corp., Taiwan.
- Playfoot et al.,** 1976. Liquid metal level sensor with increased sensitivity, U.K patent (19) 3,996,801.
- Rajendran, A.,** Asokane, C., Elumalai, G., Swaminathan, K. 1996. Development of an Ultrasonic Under-sodium scanner for the fast Breeder Test Reactor.” Proc. 14<sup>th</sup> World Conf. on Non-Destructive Testing, New Delhi, India, pp. 349- 352.
- Ravi, L.,** Velusamy, K., Chellapandi P., 2013. A robust thermal model to investigate radial propagation of core damage due to total instantaneous blockage in SFR fuel subassembly, Annals of Nuclear Energy, **62**, pp. 342-356.
- Rohrbacher, H.A.,** Bartholomay, B. 1974. Ultrasonic and acoustic detection methods for LMFBR's, Proc. BNES Conf. Fast Reactor Power Stations (London Thomas Telford), pp. 505-514.
- Selvaraj, R.** 1978. Fast Response Stainless steel thermocouple, RRC Report No.: 27, IGCAR, Kalpakkam.
- Srinivasan, G.,** Suresh Kumar, K.V., Rajendran, B., Ramalingam, P.V., 2006. The Fast Breeder Test Reactor - Design and operating experiences, Nuclear Engineering and Design, **236 (7-8)**, pp. 796–811.
- Swaminathan, K.,** Asokane, C., Sylvia, J.I., Kalyanasundaram, P., Swaminathan, P., 2012, An Ultrasonic Scanning Technique for In-Situ ‘Bowling’ Measurement of Prototype Fast Breeder Reactor Fuel Sub-Assembly, IEEE transactions on Nuclear Science, **59 (1)**, pp. 174- 181.
- Swaminathan, P.,** 2004. Computer based on-line monitoring system for Fast Breeder Test Reactor, India, IAEA Technical meeting in increasing instrument calibration through on-line monitoring Technologies, Halden, Norway.

- Swaminathan, P., Srinivasan, P.** 1996. Computer Based core Monitoring System, OECD Specialists Meeting on In-core instrumentation and reactor core assessment, Japan.
- Swaminathan, K., Rajendran, A., Elumalai, G.,** 1990. Development and Deployment of an Ultrasonic Under-Sodium Viewing System in the Fast Breeder Test Reactor, IEEE Trans. Nuclear Science, **NS- 37(5)**, pp.1571-1577.
- Trapp, J.P., Girard, J.Ph.,** 1990. Instrumentation for LMFBR Control and Safety Phenix and Super-Phenix feedback with a view to the EFR Volume III, Proc. Int. Fast Reactor Safety Meeting.
- Turnbull, D.H., Foster, F.S.,** 1991. Beam Steering with Pulsed Two-Dimensional Transducer Arrays, IEEE Trans. Ultrason. Ferroelectrics Freq. Contr. **38(4)**, pp.320-333.
- Uesugi, N., et al.,** 1979. An Ultrasonic viewing system in liquid sodium, IEEE Nuclear Science Symposium, USA.
- Uma Seshadri, et al.,** 1989. Instrumentation for supervision of core cooling in FBTR and PFBR, Proc. IAEA specialists meeting on instrumentation for FBR, Report no. IWGFR/72, IGCAR, India.
- Velusamy, K., Juby Abraham, Rajendrakumar, M., Padmakumar, G., Kasinathan, N., Selvaraj, P., Chellapandi, P., Vaidyanathan, G., Chetal, S.C.** 2010. Thermal Hydraulic Studies For Fast Breeder Test Reactor, Proc. Int. Workshop on New Horizons in Thermal Hydraulics and Safety, AERB, Mumbai, India.
- Vinolia, K., Srinivasan, G., Swaminathan, P., Ramalingam, P.V.,** 2008. Proposal to inhibit Plugging detection Supervision program after LOR order, Report: RMD/FBTR/S-ST-3/66100/TN-707.
- Wang, Z., Zhou, Y., Tian, J.,** 2008. TOFD-Scan Imaging Based on Synthetic Aperture Focusing Technique, Proc. 17<sup>th</sup> World Conf. on Nondestructive Testing, Shanghai, China.

**Watkins, R.D., Barret, L.M., Mcknight, J.A., 1988. Ultrasonic wave guide for use in sodium coolant of fast reactors, Nuclear Energy 27(2), pp. 885-891.**

## Nomenclature

$A$	Contact area between the thermocouple and the inside of the well
$C_p$	Specific heat capacitance of sodium
$C_w = C_2$	Thermal capacitance of Well
$C_b = C_1$	Thermal capacitance of the thermocouple bulb
$(C_p)_{Na}$	Specific heat capacity of sodium
$(C_p)_{ss}$	Specific heat capacity of stainless steel
$D_o$	Outer diameter of thermowell
$D_i$	Inner diameter of thermowell
$d$	Diameter of clad
$d_o$	Clad Outer Diameter
$d_i$	Clad Inner Diameter
$E$	Electromotive force
$\Delta E$	Difference in secondary voltage at extreme temperature
$\Delta E_T$	Change in secondary O/P in mV w.r.t temperature
$f_{ch}$	Channel hotspot factor
$f_{cl}$	Clad hotspot factor
$f_{fi}$	Film hotspot factor
$h$	Heat transfer film coefficient of sodium
$I_1$	Primary exciting current

$K$	Amplitude of the step input
$K_c$	Clad Thermal conductivity
$k$	Coupling factor
$L$	Length of the wire
$L_1$	Self inductance of primary
$L_2$	Self inductance of secondary coil
$l_1$	Distance from bottom of coils
$l_2$	Distance from top of coils
$M$	Mutual inductance between coils
$M_{ss}$	Mass of stainless steel structure
$M_{Na}$	Mass of sodium
$m$	Mass flow rate of sodium through the subassembly
$\dot{m}$	Mass flow rate
$n_1$	Number of primary coil turns
$n_2$	Number of secondary coil turns
$P$	Power generated in the central subassembly
$R$	Ramp rate
$R_f$	Film resistance of source
$R_{w1}$	Thermal resistance offered by half of the wall thickness of the thermo-well
$R_{w2}$	Thermal resistance offered by other half of the wall thickness of the thermo-well

$R_c$	Thermal resistance of contact between the Stainless Steel sheathed thermocouple and the inside surface of thermo-well
$R_i$	Internal resistance calculated by dividing primary voltage by primary current
$\Delta R_i$	Difference in internal resistance at extreme temperature
$R_{ext}$	External resistance to be connected across secondary coil
$r_1$	Inner radius of coil
$r_2$	Outer radius of coil
S	Sensitivity
$T_{ss}$	Steady state temperature
$T_1$	Core outlet temperature (ramp rate is experienced here)
$T_2$	SA top temperature
$T_1^0$	SA top temperature at a previous instant
$T_1^n$	SA top new temperature
$T_2$	Temperature at 15 mm above SA top
$T_2^0$	15mm/80mm above SA top temperature (previous value)
$T_2^n$	15mm/80mm above SA top temperature (new value)
$T_m$	Measured SA outlet temperature at $t_2$
$T_{cladmid-wallhot}$	Clad middle wall hot temperature
$T_{ss(004X)}$	Steady state temperature of thermocouple 004X
$T_{SA(004X)}$	Temperature measured by thermocouple 004X

$T_{ss-inlet}$	Inlet temperature at Steady state
$T_{inlet(t2)}$	Inlet temperature at time t2
$T_{CSA-SS}$	Central SA temperature at Steady state
$T_{csA(t2)}$	Central SA temperature at time t2
$T_{ss(80mm)}$	Temperature at 80mm above SA top at Steady state
$T_{SA(80mm)}$	Temperature at 80mm above SA top at that instant
$\Delta T_{channel}$	Channel temperature
$\Delta T_{film}$	Film temperature
$\Delta T_{clad-mid}$	Clad mid-wall temperature
$\Delta T_{hot\ spot}$	Hot spot temperature
$T_{clad\ hot\ spot}$	Clad hot spot temperature
$\Delta T_{clad-mid-nominal}$	Clad nominal mid wall temperature
$\Delta T_{SA}$	Temperature rise across the SA
$T_{SA\ O/L}$	Subassembly outlet temperature
$T_{in}$	Subassembly inlet temperature
$\Delta T_{ch}$	Maximum rated channel Temperature
$T_e$	SA outlet temperature
$T_m$	Thermocouple temperature
$T_i$	SA outlet temperature at t=0
$T_{Ref}$	Reference temperature

$T_{jn}$	Junction temperature
$t$	Total time required to SCRAM
$V_i$	Input voltage
$V_o$	Output voltage
$z$	Transfer impedance

## Greek letters

$\alpha$	Separation constant
$\beta$	Channel fraction
$\tau$	Time constant of thermocouple
$\varepsilon_A$	Seebeck coefficient of wire A
$\varepsilon_B$	Seebeck coefficient of wire B
$\tau_{process}$	Time constant of process
$\Delta\tau_{tc+process}$	Combined Time constant of process and thermocouple
$\chi$	Linear power
$\theta$	Thermocouple response time
$\omega$	Angular frequency of $I_1$
$\mu_0$	Free space permeability

## Subscripts

$ch$	Channel
$cl$	Clad

<i>fi</i>	Film
<i>SA</i>	Subassembly
<i>o/l</i>	Outlet
<i>in</i>	Inlet
<i>o</i>	Outer
<i>I</i>	Inner
<i>Ref</i>	Reference
<i>Jn</i>	Junction
<i>w</i>	wall thickness
<i>c</i>	Contact Resistance
<i>ss</i>	Stainless steel
<i>Na</i>	Sodium
<i>ext</i>	External

### **Superscripts**

0	Previous instant
<i>n</i>	New instant

### **ABBREVIATION**

AC	Alternating Current
ARDM	Absorber Rod Drive Mechanism
CCW	Counter Clockwise
CSR	Control Safety Rod
CSRDM	Control Safety Rod Drive Mechanism
CST	Computer Scan Time

CW	Clockwise
DC	Direct Current
DIR	Direction
DSRDM	Diverse Safety Rod Drive Mechanism
DSR	Diverse Safety Rod
DND	Delayed Neutron signal
EBR	European Breeder Reactor
e.m.f	Electro motive force
FBR	Fast Breeder Reactor
FBTR	Fast Breeder Test Reactor
FSA	Fuel subassembly
IVTP	In-vessel Transfer Pot access port
IHX	Intermediate Heat Exchanger
LED	Light Emitting Diode
LOR	Lowering of control rod
MI	Mineral Insulated
MgO	Magnesium Oxide
Na-24	Sodium isotope 24
PC	Personnel Computer
PFR	Prototype Fast Reactor
PHWR	Pressurised Heavy Water Reactor
PLC	Programmable Logic Controller
Pu	Plutonium

PZT	Lead Zirconate Titanate
RF	Radio frequency
RTD	Resistance Temperature Detector
SA	Subassembly
SCRAM	Safety Control Rod Accelerated Mechanism
SDM	Shut Down Margin
SPX	Super Phenix
SSA	Shielding subassembly
TC	Thermocouple
TIB	Total Instantaneous Blockage
T/W	Thermowell
U	Uranium
USUSS	Under Sodium Ultrasonic Scanner
UU	Uranium Utilisation
USV	Ultra Sonic viewer

## **PUBLICATIONS BASED ON THESIS**

### **INTERNATIONAL JOURNAL PAPERS**

1. Ultrasonic Imaging of Projected Components of PFBR. **Sylvia JI**, Jeyan MR, Anbucheliyan M, Asokane C, Rajan Babu V, Babu B, Rajan KK, Velusamy K and Jayakumar T, Nuclear Engineering and Design, 2013, Vol. 258, pp., 266-274.
2. Development of Mutual Inductance Type Sodium Level Detectors for PFBR. **Sylvia JI**, Vijayamohana Rao P, Babu B, Madhusoodanan K, Nuclear Engineering and Design, 2013, Vol. 262, pp. 219-227
3. A Novel Method for In-Situ Estimation of Time Constant for Core Temperature Monitoring Thermocouples of Operating Reactors. **Sylvia JI**, Clement Ravi Chandar S and Velusamy K, Nuclear Engineering and Design, 2014, Vol.275, pp. 154-162.

### **CONFERENCE PROCEEDINGS**

4. Ultrasonic Imaging of simulated absorber rod drive mechanism of PFBR, **Sylvia J.I.**, Jeyan M.R., Anbucheliyan M., Rajan Babu V., and T.Jayakumar, Proceedings of the National Seminar and Exhibition on Non-Destructive Evaluation NDE,2011, Dec. 8-10.